POLITECNICO DI MILANO
Master Degree in Space Engineering
Dipartimento di Scienze e Tecnologie Aerospaziali

Fragmentations in low Earth orbit: event detection and parent body identification

Supervisor: Prof.ssa Camilla Colombo
Co-supervisor: Dr. Matteo Romano

Thesis of:
Andrea Muciaccia, ID 928415

Accademic Year 2019-2020

To my family

Abstract

More and more new missions and new launches are planned every year. Parallel to this, during the recent years the number of debris has considerably grown, increasing the space traffic around the Earth. Inevitably, due to the high number of uncontrolled objects, the generation of high-risk collision orbital regions tends to grow.
The presence of guidelines aimed to space debris mitigation and collision avoidance ruling the entire lifetime of the spacecraft does not always allow to avoid possible unpredictable events (e.g., explosions of spacecraft or rocket bodies) or hardly predictable events (e.g., collisions between objects in space). Consequently, by increasing the knowledge about the debris population (also studying their origin), the capability to prevent possible hazards for all the on-orbit active objects would increase.
The work proposed in this thesis has two main objectives: on the one hand the localisation in space and time of the breakup event, while on the other hand the identification of the parent object (or objects) related to the fragments. Both the objectives are achieved by considering Two-Line-Elements (TLEs) as data set for all the test cases and by analysing them through several steps. First of all, an outlier filter is applied to the initial data set to eliminate non-coherent TLEs that may be included in the initial sequence and, simultaneously, the ballistic coefficient of each object is fitted exploiting the B^* parameter available in the TLEs. Then, the method makes use of pruning/clustering techniques useful to eliminate from the data set elements uncorrelated with the desired ones needed for the localisation of the fragmentation. Mean Keplerian orbital elements are used for the propagation [1], considering a time span of the order of months to years for the long-term evolution of orbits. Numerical results, also using graphical representations, will show the capability of the proposed method for studying breakup events on the long term.
This thesis is part of the COMPASS project: "Control for orbit manoeuvring by surfing through orbit perturbations"(Grant agreement No 679086).

This project is European Research Council (ERC) funded project under the European Union's Horizon 2020 research.

Sommario

Al giorno d'oggi, ogni anno sono pianificati nuovi lanci e nuove missioni. Parallelamente, negli ultimi anni il numero di detriti è cresciuto considerevolmente, andando ad aumentare il traffico spaziale introno alla Terra. Inevitabilmente, a causa della presenza di un gran numero di oggetti non controllabili sono generate molte regioni orbitali con un alto rischio di collisione.
La presenza di linee guida riguardanti la mitigazione dei detriti spaziali e la prevenzione delle collisioni nello spazio che regolano l'intera vita dei satelliti non sempre permette di evitare eventi non predicibili (e.g. esplosione di satelliti o di lanciatori) o che sono dificilmente predicibili (e.g. collisione tra oggetti nello spazio).
Il lavoro che viene proposto all'interno di questa tesi ha due obiettivi principali: da una parte la localizzazione nello spazio e nel tempo di possibili frammentazioni, mentre dall'altra parte la possibilità di identificare l'oggeetto (o gli oggetti) dal quale hanno avuto origine i frammenti. Gli obiettivi sono raggiunti andando ad utilizzare set di dati formati da Two-Line-Elements (TLEs) per i test, analizzandoli attraverso differenti fasi. Come prima cosa, i set di TLEs sono controllati con l'utilizzo di filtri per outliers poichè possibili valori errati possono essere inclusi nelle sequenze di dati considerate. Sfruttando il parametro B^*, direttamente incluso all'interno delle TLEs, come elemento di fitting viene stimato il valore di coefficiente balistico di ciascun ogetto (necessario per la propagazione). Successivamente, il metodo proposto utilizza tecniche di filtraggio e raggruppamento (sfruttando i parametri orbitali) utili per eliminare dall'analisi elementi non correlati con quelli utili per identificare la frammentazione. La propagazione degli elementi orbitali Kepleriani è effettuata sfruttando elementi mediati e andando a considerare degli intervalli di tempo a partire dai mesi e fino agli anni per l'evoluzione a lungo termine delle orbite. Dei risultati numerici, con anche l'ausilio di immagini, mostreranno la capacità del metodo proposto di studiare gli eventi di frammentazione nel lungo periodo.

Questa tesi fa parte del progetto COMPASS: “Control for orbit manoeuvring by surfing through orbit perturbations”(Grant agreement No 679086). Questo progetto è finanziato dall’European Research Council (ERC) nell’ambito della ricerca dell’European Union’s Horizon 2020.

Acknowledgments

Before starting with the discussion of my thesis work, I would like to spend some words for the people who played a meaningful role in my academic accomplishments.
I am extremely grateful to prof.ssa Camilla Colombo for giving me the opportunity to work on such an interesting and current topic, that is the space debris world, and for her careful supervision. Then, I would like to extend my deepest gratitude to my co-supervisor Dr. Matteo Romano, for his relevant advice, his constant guidance and for all the (online) meetings we did during these months that have been a precious time for discussions and crucial for completing the work. Thanks also to Dr. Mirko Trisolini and to Dr. Stephan J. Frey for the suggestions they gave me at the beginning of the work.
Special thanks to my family, to my parents for their willingness, their help and their sacrifice that allowed me to get where I am today. Without them, this achievement would not have been possible. Thanks to my sisters Adriana, Federica and Giulia and my brother-in-law Mauro who supported me from afar throughout this challenging time.
Many thanks to my grandparents who have been a powerful source of inspiration for me. Thanks also to all my big warm family for their constant presence and interest in my course of study.
Thanks should also go to all my friends with whom I shared the last six years away from home. Firstly, thanks to my roommate and my ex house mates for all experiences both good and bad that made us grow and mature together.
Then, I would say thank you to all the friends/guys I have met in Milano, especially in Politecnico, who made lessons and study more pleasant and stimulating, in particular my colleagues who carried out university projects with me.
A last thank you goes to all my friends and all the people with whom I shared exciting and significant experiences of my life.

Contents

Abstract **III**

Sommario **V**

Acknowledgment **IX**

Acronyms **XXI**

Symbols **XXIII**

1 Introduction **1**
1.1 Overview 1
1.2 Low Earth Orbit Environment 4
1.3 State of the art 6
1.3.1 Pruning and clustering 6
1.3.2 Past works on fragmentation reconstruction 9
1.3.3 Ballistic coefficient estimation 12
1.4 Scope of the thesis 13
1.5 Structure of the thesis 14

2 Theoretical models for fragmentations **15**
2.1 Low Earth orbit main perturbations 15
2.1.1 Perturbation due to Earth's non spherical gravitational field 16
2.1.2 Aerodynamic drag 17
2.1.3 Third-body perturbation 18
2.1.4 Solar radiation pressure 19
2.2 Planetary Orbital Dynamics 19
2.3 Two-Line-Elements 20
2.4 TLEs filtering outlier 21
2.4.1 TLE update time 21

2.4.2 Large time gaps . . . 22
2.4.3 Mean motion . . . 24
2.4.4 Eccentricity and inclination . . . 25
2.4.5 Negative B^* . . . 25
2.4.6 Otulier filter flowchart . . . 26
2.4.7 Filter example . . . 27
2.5 Ballistic coefficient . . . 29
2.5.1 BC estimation examples . . . 32
2.5.2 BC final considerations . . . 36
2.6 Triple loop filter . . . 37
2.6.1 Apogee-perigee . . . 37
2.6.2 MOID . . . 37
2.6.3 Time-Angular window . . . 41
2.6.4 Filter example . . . 42
2.6.5 Triple-loop flowchart . . . 45
2.7 Gabbard Diagram . . . 46

3 Event detection 47
3.1 Data preparation . . . 49
3.2 Pruning/Clustering phase . . . 49
3.2.1 Example of the pruning phase . . . 52
3.2.2 Focus on the triple-loop . . . 54
3.3 Fragmentation event . . . 54
3.3.1 Single family . . . 55
3.3.2 More than one family . . . 58
3.4 Outcomes . . . 60

4 Parent body identification 61
4.1 Inclination . . . 63
4.2 Triple-loop and right ascension of ascending node . . . 66
4.3 Discussion . . . 70

5 Fragmentation scenarios 71
5.1 Test considering a single family . . . 72
5.1.1 Event detection . . . 72
5.1.2 Refinement . . . 75
5.1.3 Parent identification . . . 78
5.2 Test considering more than one family . . . 81
5.2.1 Iridium 33 Breakup . . . 82
5.2.2 Fengyun 1C Breakup . . . 85

5.2.3 SL-14 R/B Breakup 88
5.2.4 USA 109 Breakup 91

6 Conclusions **93**
6.1 Summary 93
6.2 Future works 95

Bibliography **103**

A Hierarchical clustering method examples **105**

B Two-Line-Elements **107**

C MOID parameters **111**
C.1 Position vector 111
C.2 Coefficients of the polynomial system 112
C.3 Sylvester matrix and resultant 113

D Objects ID **115**
D.1 Triple-loop filter example Elements ID 115
D.2 Single Family 115
D.2.1 Cosmos 2251, single family case 1 115
D.2.2 Cosmos 2251, single family case 2 115
D.2.3 NOAA 16, single family case 1 116
D.2.4 NOAA 16, single family case 2 116

List of Figures

1.1 Relative proportions of the cataloged fragments (whole history) - Image taken from ESA's Annual Space Environment Report [2] last retrieved date. 2
1.2 The near Earth (up to 2000 km) altitude population - Image taken from History of on-orbit satellite fragmentations 15^{th} Edition [5]. 5
1.3 Number of objects per orbit inclination - The objects considered are the one included in the daily catalogue (`https://www.space-track.org/`) on 23 February 2021. 5

2.1 High update time example 23
2.2 Outlier filter flowchart. 26
2.3 TLEs filter example 28
2.4 Event detection flowchart. 31
2.5 BC estimation as function of time and of the solar flux model. 32
2.6 Semi-major axis evolution over time - daily solar flux. 33
2.7 Apogee and perigee altitudes evolution over time - daily solar flux. 34
2.8 Semi-major axis evolution over time - sinusoidal solar flux. . . 34
2.9 Apogee and perigee altitudes evolution over time - sinusoidal solar flux. 34
2.10 Semi-major axis evolution over time - daily solar flux. 35
2.11 Apogee and perigee altitudes evolution over time - daily solar flux. 35
2.12 Semi-major axis evolution over time - sinusoidal solar flux. . . 36
2.13 Apogee and perigee altitudes evolution over time - sinusoidal solar flux. 36
2.14 Angular windows around MOID points - Image taken from Hoots et al. [21].. 41
2.15 Filtering process initial conditions. 42

2.16 Apogee/Perigee filter 43
2.17 MOID filter 44
2.18 Conditions after the third filter. 44
2.19 Triple-loop filter flowchart. 45
2.20 Gabbard Plot of Iridium 33 breakup, nine months after the event. 46

3.1 Event detection flowchart. 48
3.2 Distribution of the objects with respect to the normalised (on the maximum value) inclination, eccentricity, and semi-major axis of each orbit, before the inclination clustering. 50
3.3 Distribution of the objects with respect to the normalised (on the maximum value) inclination, eccentricity, and semi-major axis of each orbit, after the inclination clustering. 51
3.4 Location of the unknown Iridium 33 fragment with respect to the limits in inclination of the Iridium 33 debris. 53
3.5 Distribution of the objects with respect to the normalised (on the maximum value) inclination, eccentricity and semi-major axis of each orbit, after the inclination clustering (the orange dot is the unknown fragment). 53
3.6 First rough estimation of the event epoch. 55
3.7 Evolution in time of $\Delta\Omega$ - Cosmos 2251 example. 57
3.8 Ω distribution - Before the propagation. 59
3.9 Ω distribution - At the event date 59

4.1 Event characterisation flowchart. 62
4.2 Objects distribution in inclination and in right ascension of ascending node of each orbit - NOAA 16 satellite. 64
4.3 Objects distribution in inclination and in right ascension of ascending node of each orbit - Cosmos 2251 satellite. 64
4.4 Objects distribution in inclination and in right ascension of ascending node of each orbit - Iridium 33 satellite. 65
4.5 Objects distribution in inclination and in right ascension of ascending node of each orbit - Fengyun 1C satellite. 65
4.6 Number of fragments per orbit inclination - Fengyun 1C satellite. 65
4.7 Gabbard plot of fragments and parent candidates. 67
4.8 MOID between fragments and Cosmos 2251. 68
4.9 Fragments and parent candidates distribution in inclination and in right ascension of ascending node of each orbit. 69

5.1 $\Delta\Omega$ as function of initial date of the analysis - Test case set 1. 73
5.2 $\epsilon_r\%$ as function of initial date of the analysis - Test case set 1. 73
5.3 $\Delta\Omega$ as function of initial date of the analysis - Test case set 2. 74
5.4 $\epsilon_r\%$ as function of initial date of the analysis - Test case set 2.. 74
5.5 Refined $\epsilon_r(\%)$ as function of initial date of the analysis - Cosmos 2251 test case. 75
5.6 Refined $\epsilon_r(\%)$ as function of initial date of the analysis - NOAA 16 test case. 76
5.7 Number of identified close approaches per correction time - Test case 1 month. 77
5.8 Number of identified close approaches per correction time - Test case 12 months. 77
5.9 Number of survived candidates as a function of inclination threshold Δi - NOAA 16 test case. 79
5.10 Number of survived candidates as a function of inclination threshold Δi - Cosmos 2251 test case. 80
5.11 $\epsilon_r(\%)$ as function of the unknown object - Iridium 33 test case. 83
5.12 $\Delta\Omega$ evaluated at the event date - Iridium 33 test case. 83
5.13 Number of survived candidates as a function of inclination threshold Δi - Iridium 33 test case. 84
5.14 $\epsilon_r(\%)$ as function of the unknown object - Fengyun 1C test case. 86
5.15 $\Delta\Omega$ evaluated at the event date - Fengyun 1C test case. . . . 86
5.16 Number of survived candidates as a function of inclination threshold Δi - Fengyun 1C test case. 88
5.17 Ω distribution - SL-14 R/B test case. 89
5.18 Number of survived candidates as a function of inclination threshold Δi - SL-14 R/B test case. 90
5.19 Ω distribution - USA 109 test case. 91

List of Tables

3.1 Number of objects survived after the inclination filter depending on the selected Δi. 52

5.1 Parent identification, second step results - NOAA 16 test case. 79
5.2 Parent identification, second step results - Cosmos 2251 test case. 81
5.3 Filter thresholds - Iridium 33 test case. 82
5.4 Objects included in the set after the pruning phase - Iridium 33 test case. 82
5.5 Parent identification, second step results - Iridium 33 test case. 85
5.6 Filter thresholds - Fengyun 1C test case. 85
5.7 Objects included in the set after the pruning phase - Fengyun 1C test case. 87
5.8 Parent identification, second step results - Fengyun 1C test case. 88
5.9 Filter thresholds - SL-14 R/B test case. 89
5.10 Parent identification, second step results - SL-14 R/B test case. 90
5.11 Filter thresholds - USA 109 test case. 91

B.1 TLE-Line 1 108
B.2 TLE-Line 2 109

Acronyms

AoP	Argument of Perigee
A/P	Apogee/Perigee
BC	Ballistic Coefficient
CDF	Cumulative Distribution Function
DFT	Discrete Fourier Transformation
ESA	European Space Agency
FFT	Fast Fourier Transformation
GEO	Geostationary Orbit
GTO	Geostationary Transfer Orbit
HEO	Highly Elliptical Orbit
HCM	Hierarchical Clustering Method
ID	Identification Number
IDFT	Inverse Discrete Fourier Transformation
LEO	Low Earth Orbit
MAD	Mean Absolute Deviation
MEO	Medium Earth Orbit
MOID	Minimum Orbit Intersection Distance
NASA	National Aeronautics and Space Administration
NORAD	North American Aerospace Defense Command
PlanODyn	Planetary Orbital Dynamics
PDF	Probability Density Function
RAAN	Right Ascension of Ascending Node
SBM	Standard Breakup Model

SGP4	Standard General Perturbations 4
SDP	Simplified Deep Space Perturbations
SOFT	Simulation of On-Orbit Fragmentation Tool
SRP	Solar Radiation Pressure
SSN	Space Surveillance Network
TEME	True Equator Mean Equinox
TLE	Two-Line-Element
US	United States
WAM	Wavelet Analysis Method

Symbols

a	Semi-major axis of the orbit $[km]$
$\underline{a}_{drag}$	Perturbing acceleration due to atmospheric drag effect $[m/s^2]$
$\underline{a}_{3B}$	Perturbing acceleration due to the third body effect $[m/s^2]$
$\underline{a}_{SRP}$	Perturbing acceleration due to SRP effect $[m/s^2]$
A_{corss}	Cross-sectional area $[m^2]$
A_{cr-Sun}	Cross-sectional area normal to the sun direction $[m^2]$
AU	Astronomic unit $(1.495978707 \cdot 10^{11} m)$
A/m	Area to mass ratio $[m^2/kg]$
B^*	Drag-like parameter used with simplified perturbations models
$\underline{c}$	Angular momentum vector $[kg \cdot m^2/s]$
c_d	Drag coefficient [-]
c_r	Reflectivity coefficient [-]
C_{nm}	Empirically determined coefficient (tsseral harmonic potential computation)
D_{SH}	Similarity distance (Southworth-Hawkins) [-]
D_D	Similarity distance (Drummond) [-]
D_J	Similarity distance (Drummond) [-]
e, E	Eccentricity of the orbit [-]
E_{rel}	Relative kinetic energy $[J]$
$f_{r_{drag}}$	Acceleration due to drag in radial direction $[m/s^2]$
$f_{t_{drag}}$	Acceleration due to drag in transverse direction $[m/s^2]$
$f_i(t)$	Polynomial coefficient, calculated in operationby t

	with i = 0,...,4
$\underline{F}$	Perturbing force $[N]$
$g_i(t)$	Polynomial coefficient, calculated in operationby t
	with i = 0,1,2
i	Inclination of the orbit $[deg]$
I_{21}	Angle between the orbital planes
J_2	Second-order zonal harmonic [-]
J_4	Fourth-order zonal harmonic [-]
$J_{2,2}$	Second-order tesseral harmonic [-]
k, K	Weightings parameters [-]
m_b	mass of a body $[kg]$
n	Mean motion [rev/day]
n_{reg}	Mean motion evaluated through the regression technique
	[rev/day]
p, P	Semi-latus rectum of the orbit $[km]$
P_n/P_{nm}	Legendre polynomials
$P_{SR@1AU}$	Solar radiation pressure at one astronomic unit
q	Perigee distance $[km]$
Q	Apogee distance $[km]$
r, R	Geocentric distance $[km]$
$\underline{r}$	Position vector $[km]$
$\underline{r}_{b-3B}$	Distance vector from the spacecraft to the third-body $[km]$
$\underline{r}_{b-Sun}$	Distance vector from the spacecraft to the Sun $[km]$
$\underline{r}_{E-3B}$	Geocentric distance vector of the third body $[km]$
R_E	Earth radius $[km]$
R_{rel}	Rate of change of the relative distance
$\dot{R}_{rel}$	Derivative in time of R_{rel}
$Res(t)$	Resultant of a matrix, calculated in operationby t
s	True anomaly (exploited during MOID formulation)
	after a change of variables $[deg]$

$S(t)$	Sylvester matrix
$\hat{S}(t)$	Modified Sylvester matrix
S_{nm}	Empirically determined coefficient
	(tsseral harmonic potential computation)
t	True anomaly (exploited during MOID formulation)
	$[deg]$
$\mathbf{t}$	Time $[s]$
T_A	Absolute tolerance
T_R	Relative tolerance
U	Potential function
U_{ZH}	Zonal harmonics potential function
U_{TH}	Tesseral harmonics potential function
v, V	True anomaly (exploited during MOID formulation)
	$[deg]$
v_{rel}	Relative module between two orbiting bodies $[km/s]$
$\underline{v}_{rel}$	Relative velocity vector $[km/s]$
	after a change of variables $[deg]$
δv	Velocity increment $[m/s]$
ϵ_{rel}	Relative error
θ	True anomaly [deg]
λ	Longitude position of a space object $[deg]$
μ_E	Earth gravitational parameter $[m^3/s^2]$
μ_{3B}	Third body gravitational parameter $[m^3/s^2]$
Π_{21}	Difference of the longitudes of perigees measured from
	the intersection of the orbits
ρ	Atmospheric density $[kg/m^3]$
ϕ	Latitude position of a space object $[deg]$
$\underline{\chi}$	Position vector (exploited during MOID formulation) $[km]$
ω	Argument of perigee $[deg]$
Ω	Right ascension of ascending node $[deg]$

#	Cardinality of a set

Chapter 1

Introduction

Nowadays, the study of space debris, of their evolution in time, and of their influence on the space around the Earth is assuming a relevant position in the research world. The number of objects currently in orbit in LEO region is assessed to be 13932, 9714 of which are catalogued as space debris [2]. The high number of uncontrolled objects generates many space region with the possibilities of collisions or other breakup events. This inevitably affects satellite traffic around the Earth, giving back importance to the knowledge about the defunct human-made objects.

1.1 Overview

Before analysing the space debris distribution, it is essential to note that the following description is only related to artificial debris, therefore it does not include natural space debris; moreover, it is important to properly classify the different types of space debris. The first category of these objects is the so called mission-related debris [3]; inside this set are considered objects coming from possible releases during spacecraft's operation, activation, deorbit, and deployment both for payloads and rocket bodies [2]. Usually, the number of such objects is quite low per mission; indeed, spring release mechanisms or spin-up devices, protective covers for optical instruments (e.g. sensors, cameras), astronaut tools are limited in number in the various missions. However, sometimes the number of objects could be high: this is the case of the Mir space station, orbiting with a perigee altitude of 340 km and an apogee altitude of 400 km [4], that in its entire life (around fifteen years) has produced 323 of such debris. The second source are the satellite breakup [5] debris, defined as objects generated by destructive disassoci-

ation of an orbital payload, rocket body, or structure, often with a wide range of ejecta velocities [5]. This category contains the major amount of objects. Inside this set are classified debris related to collisions (intentional or not) and explosions. Well-known examples are the accidental Cosmos 2251- Iridium 33 collision, occurred on 10^{th} February 2009 [5], and the deliberate destruction of the Fengyun 1C, occurred on 11^{th} January 2007 [5]. The last category contains the anomalous events [5]. Here are included all the objects which detach from the main body, usually with a low velocity; as an example, debris shedding due to material deterioration and detachment of appendages are part of this class. This type of debris represents typically a minor source with respect to the satellite breakup set.
Figure 1.1 shows the relative proportions for the different type of breakup or anomalous sources of debris. As it can be observed, the anomalous type covers a lower percentage inside the total amount of classified objects. This occurs because many more objects are generated during fragmentations.

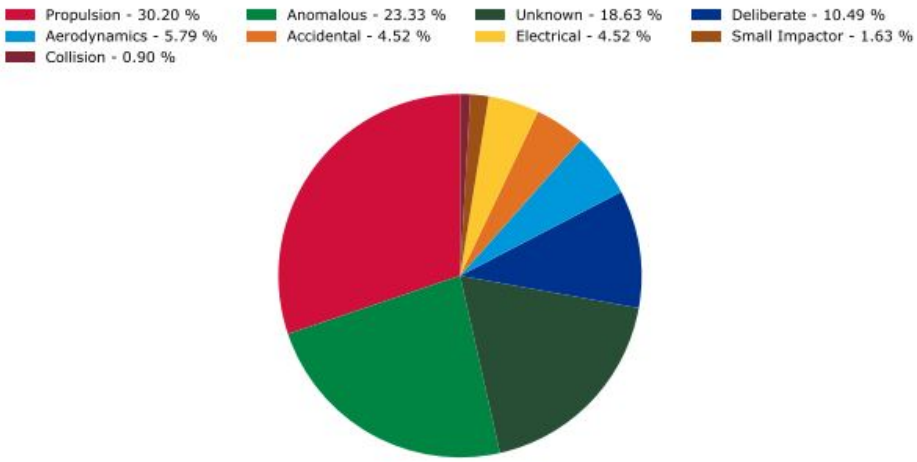

Figure 1.1: Relative proportions of the cataloged fragments (whole history) - Image taken from ESA's Annual Space Environment Report [2] last retrieved date.

A further distinction is made between traceable and untraceable objects. The US Space Surveillance Network (SSN), with the use of ground-based radars and optical measurements, is able to track objects larger[1] than 5 cm in LEO and larger than 1 m in GEO [6]. This implies that objects with a lower diameters have to be estimated or modelled separately. A proper

[1]The debris size are intended as equivalent diameter

model of these micro debris is important because for satellite manufacturers the most dangerous objects are the ones with size between 5 and 15 mm [7]. Moreover, collisions with objects larger than 1 cm could damage or disable operative spacecraft, while collisions with objects larger than 10 cm could lead to catastrophic events. This because the relative orbital velocity can reach very high values (e.g. up to 14 km/s). The main issue of catastrophic and non-catastrophic collisions is related to the so-called Kessler syndrome [8], that is the continuous growth of the debris population due to concatenated collisions/explosions.

As observed, the generation of new debris is strictly correlated with the increase in the number of missions. This requires the formulation and the use of standards related to space debris mitigation and collision avoidance. The general aim of space debris mitigation is to reduce the growth of space debris by ensuring that spacecraft and launch vehicle orbital stages are designed, operated, disposed of in a manner that prevents them from generating debris throughout their lifetime [9]. Moreover, it is important to avoid any harm during the re-entry phase. This objectives are achieved by adopting some preventive actions during the entire life of the mission. Indeed, there is the need to not release intentionally debris during orbital operations or to avoid possible breakups (although this is not always predictable). During the design of the mission it is important to analyse the risk of possible collisions with other space objects; these considerations are also needed during the entire lifetime of the missions with the use of proper collision avoidance maneuvers. It is also important to remove spacecraft and launch vehicles from protected regions both at the beginning and at the end of the mission. The latter can be performed by a re-entry (for LEO and some MEO satellites), during which it is important to avoid any risk for people or Earth environment, or with the use of so-called spacecraft graveyard orbits (of which one is above the GEO region). The graveyard orbit regions are sectors where no-more operative spacecraft are collected to protect the ones that are still operative. In addition, for LEO missions, the current procedure provides that the a re-entry phase of the mission has to be successfully completed in a maximum of 25 years [2].

Considering all the previous notions, it is evident that precise models which describe the debris evolution and their generation are of great importance. Indeed, with the use of this kind of models it is possible to perform more in-depth analysis suited to improve the safety of the future missions and in general of the entire space around the Earth. The work here presented focuses on two main characteristics: the detection of possible occurred fragmentations and the identification of the parent(s) that originated the frag-

ments. The use of filters based on Keplerian orbital elements, along with useful algorithms to estimate the ballistic coefficient of each fragment, are necessary to achieve these results. All the features exploited for the development of the final model will be discussed in the following Sections and Chapters.

1.2 Low Earth Orbit Environment

The work presented here focuses its attention in the study of fragmentations occurred in LEO. Hence, it is important to have clear in mind its major characteristics before starting with the analysis of the fragmentations. Indeed, each region in space has its main features which make its study peculiar.
Before illustrating the various types of perturbations that typically affect objects orbiting in this region, it is interesting to analyse the distribution of space debris inside it. As stated in Section 1.1, breakup events are the major source of debris. This is more true when the LEO region is considered. Figure 1.2 shows the distribution of space debris with altitude (data reported date back to 28^{th} October 2018). To display the distribution, the spatial density (i.e. number of objects per unit volume) is an interesting parameter since many objects traverse the altitude regions of interest yet contribute little to the local collision hazard (e.g. Geosynchronous Transfer Orbits)[5]. As it can be observed, the region around the 800 km presents two peaks: a small peak at an altitude of around 790 km related to the Iridium 33/Cosmos 2251 collision, and an higher peak at an altitude of around 890 km mainly related to the Fengyun 1C breakup. Obviously, these two events are not the only ones that affect that region of space; indeed, the NOAA-16 US weather satellite (which broke up on 25 November 2015) gives a great contribution with its 458 debris still in orbit at the epoch considered.

Additional considerations can be done by observing the distribution of the objects with respect their orbit inclination. Figure 1.3 shows a dominance of objects orbiting with an inclination around 100 deg. This surely is related to the presence of many objects placed in sun-synchronous orbits, widely used for near Earth missions (e.g. weather satellites), that inevitably increase the probability of events (like the Fengyun 1C) occurring in this region. As can be deduced from the study of the models ([10]), the inclination is little affected by perturbations in LEO, remaining constrained throughout the entire life of the object. Missions planned to cross or live in those areas have to pay attention to all the possible risks.

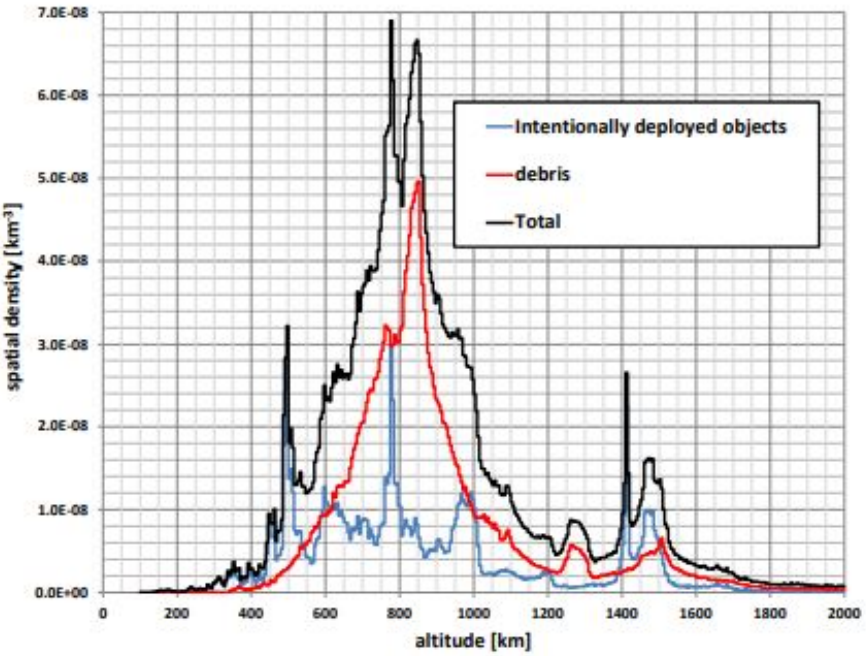

Figure 1.2: The near Earth (up to 2000 km) altitude population - Image taken from History of on-orbit satellite fragmentations 15^{th} Edition [5].

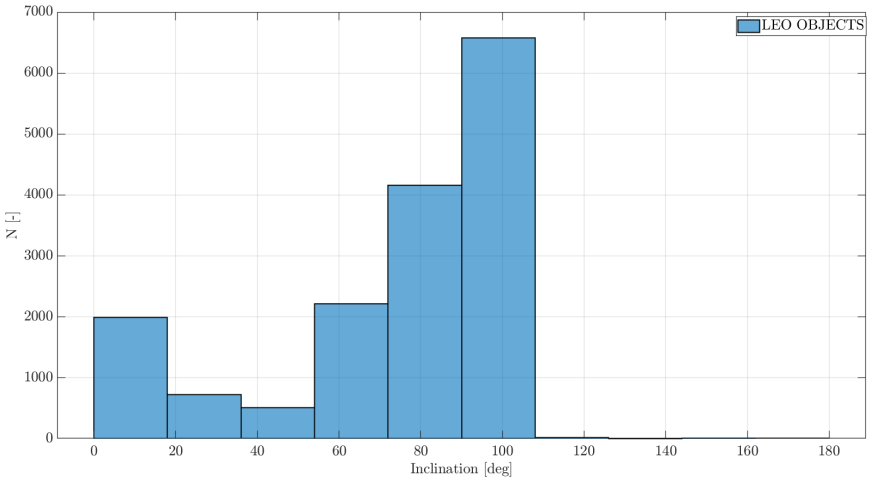

Figure 1.3: Number of objects per orbit inclination - The objects considered are the one included in the daily catalogue (`https://www.space-track.org/`) on 23 February 2021.

1.3 State of the art

For the development of the final model, several problems need to be analysed, including the identification of the correct fragments among all those included in a generic initial set and the estimation of their ballistic coefficient, which is extremely useful during the propagation phase. Firstly, pruning and clustering techniques are extremely important when objects coming from different parent bodies have to be studied, since objects that share a common origin may have some common features (Section 1.3.1). This is the case of the space debris generated from the same parent body; the use of these algorithms makes it possible to eliminate from the study all the objects that are not related to the ones examined. In addition, Section 1.3.2 introduces past work that shares the same goal as this thesis. Then, a proper estimation of the ballistic coefficient is required to have an higher accuracy in the propagation (as discussed in Section 1.3.3); the latter is more important in this thesis work since long-term propagations are analysed.

1.3.1 Pruning and clustering

Part of the methods presented here come from the study of asteroid families. Indeed, many techniques have been designed over the years in the asteroids field. It is worth to mention that all these techniques are thought to be used exploiting proper orbital elements, that are orbital elements which include only secular periodic perturbations (i.e. short/long periodic perturbations are neglected) [11]. In this way, the orbital parameters remain almost constant for a long time span and common features can be identified between different objects; contrary, if osculating elements (which consider also short/long periodic perturbations) are considered, local variations may affect the family analysis. For the thesis work, mean elements are considered, hence only short periodic perturbations are discarded.
The three main methods reported in literature for the asteroids families identification are the Hierarchical Clustering Method (HCM), the D-Criterion, and the Wavelet Analysis Method (WAM). The first two methods share some common features and are directly connected with the analysis of the orbital parameters; the last method is a density-evaluation method based on the use of a particular function called “wavelet”, having a characteristic size defined according to the adopted metric [12]. The basic idea is the same for the three methods: first the two more similar objects are identified and clustered together; then, by exploiting the similarity metric function, other objects are added to the cluster until the family is completed.

Different metrics are available to perform clustering by exploiting the D-criterion. The first developed method was introduced by Southworth and Hawkins at al. [13]. The metric proposed is

$$D_{sh}^2 = (e_2 - e_1)^2 + \frac{(q_2 - q_1)^2}{R_{Earth}^2} + \Big(2sin\Big(\frac{I_{21}}{2}\Big)\Big)^2 + \Big(\frac{e_2 + e_1}{2}\Big)^2\Big(2sin\Big(\frac{\Pi_{21}}{2}\Big)\Big)^2 \tag{1.1}$$

where e is the eccentricity, q is the perigee distance, R_{Earth} is the Earth mean radius, I_{21} (that could vary between 0 degrees and 180 degrees) is the angle between the orbital planes and is computed as

$$\Big(2sin\Big(\frac{I_{21}}{2}\Big)\Big)^2 = \Big(2sin\Big(\frac{i_2 - i_1}{2}\Big)\Big)^2 + sin(i_a)sin(i_b)\Big(2sin\Big(\frac{\Omega_b - \Omega_a}{2}\Big)\Big)^2 \tag{1.2}$$

where i is the inclination and Ω is the right ascension of the ascending node of the orbits. The last parameter to be evaluated is Π_{21}, that is the difference of the longitudes of perigees measured from the intersection of the orbits (starting from anyone of the mutual nodes [14]) and it is computed as

$$\Pi_{21} = \omega_2 - \omega_1 + 2sin^{-1}(S_{21}) \tag{1.3}$$

where S_{21}

$$S_{21} = cos(\frac{i_2 + i_1}{2})sin(\frac{\Omega_2 - \Omega_1}{2})sec(\frac{I_{21}}{2}) \tag{1.4}$$

As observable in equation 1.1, the D-criterion presents inside its metric all the orbital parameters usually exploited to describe space objects motion. D_{sh}^2 typically is called similarity function; the meaning of this name is related to the facts that in order to have low values, the two objects must present similar Keplerian elements.
A second metric was proposed by Drummond at al. [15] and it is a modification of the Southworth-Hawkins equation

$$D_D^2 = \Big(\frac{e_2 - e_1}{e_2 + e_1}\Big)^2 + \Big(\frac{q_2 - q_1}{q_2 + q_1}\Big)^2 + \Big(2sin\Big(\frac{I_{21}}{2}\Big)\Big)^2 + \Big(\frac{e_2 + e_1}{2}\Big)^2\Big(2sin\Big(\frac{\theta_{21}}{2}\Big)\Big)^2 \tag{1.5}$$

with

$$I_{12} = cos^{-1}\Big(\frac{\underline{c}_1 \cdot \underline{c}_2}{c_1 c_2}\Big) \tag{1.6}$$

and

$$\theta_{12} = \left(\frac{\underline{e}_1 \cdot \underline{e}_2}{e_1 c_e}\right) \tag{1.7}$$

where $\underline{c}_1$ and $\underline{c}_2$ are the angular momentum vectors and $\underline{e}_1$ and $\underline{e}_2$ are the Laplace-Lenz vectors. An evident diversification from the previously presented metric is the way in which the eccentricity and perigee distance are normalised.
Another metric was proposed by Jopek at al. [16]. Also this formulation is a modification of the first presented metric

$$D_J^2 = (e_2 - e_1)^2 + \left(\frac{q_2 - q_1}{q_2 + q_1}\right)^2 + \left(\frac{I_{12}}{180^\circ}\right)^2 + \left(\frac{e_2 + e_1}{2}\right)^2 \left(\frac{\Pi_{12}}{180^\circ}\right)^2 \tag{1.8}$$

where all the parameters are computed as in the Southworth-Hawkins formulation.
The second family of clustering techniques previously cited is the Hierarchical Clustering Method; as previously stated, the basic idea is the same, but the type of metric involved is different. The HCM includes in its metric only three Keplerian orbital elements: the semi-major axis, the inclination and the eccentricity. The generic metric proposed by Zappala at al. [17] is

$$\delta v = na\sqrt{k_1(\frac{\delta a'}{a'})^2 + k_2(\delta e')^2 + k_3(\delta i')^2} \tag{1.9}$$

where $\delta a', \delta e', \delta i'$ are the difference in the proper elements between the two considered bodies, n and a are the mean motion and the semi-major axis of the main body and k_1, k_2 and k_3 are weighting parameters (whose computation is reported in Appendix A). The metric is written in the form of a velocity increment since the idea proposed is that the similarity of two orbits is related to a deviation in velocity generated by the disturbances.
The last method related to the meteors/asteroid literature is the Wavelet method proposed by Bendoja at al. [18]. The basic idea is to use a wavelet transformation function that allows to detect local over-densities of points belonging to a given N-dimensional space (in this case the $\{a', e', i'\}$ space, where a' is the semi-major axis, e' is the eccentricity, and i' is the inclination of the orbits) at different scales [12]. By superimposing a grid in the phase space and computing wavelet coefficient at each node, it is possible to find more dense or more sparse regions of objects. The metric equation involved in the process is exactly the same proposed by Zappala et al. [19]; also in this case, it is required to choose the three weighting coefficients.

Other techniques that can be used as pruning methods are: the MOID evaluation, the triple-loop filter, and the nodal distance. These methods are usually exploited when collision avoidance analysis have to be performed.
The nodal distance, that is the simplest technique (and could be seen as a particular case of the MOID evaluation), makes the assumption that the minimum distance between two orbits lays along the nodal line. This can be considered as true for orbits that posses similar inclination and different eccentricity. Surely, since it is a simple geometric approach, it is computational efficient but, on the other hand, it lacks of reliability since the debris distribution being considered presents also objects with very different inclination. Consequently, it is better to focus the attention on the MOID computation. The algorithm presented here is the algebraic evaluation of the MOID proposed by Gronchi at al. [20]. The algorithm is based on the algebraic elimination theory: through the computation of the resultant of two bivariate polynomials, it identifies a 16^{th} degree univariate polynomial whose real roots give us one component of the critical points (i.e. maximum, minimum and saddle points)[20]. Among all the points, the global minimum is also identified and considered as the MOID. The method will be described more thoroughly in the following chapter.
The last method analysed is the triple-loop filter, generally exploited to evaluate the real close approach between two space objects and hence the possibility of collisions. As the name suggest, the filter is composed by three filters: two geometrical filters and a time one. The first two filters are based on geometrical properties and analyse possible conjunction looking at the apogee and the perigee of each orbit (explained more in detail in Section 2.6.1) and through the evaluation of the minimum distance between two orbits. In the method proposed by Hoots at al. [21], the MOID is evaluated by considering the minimum distance near the nodal line; as will be explained in Chapter 2, the method exploited in this works will join together this filter with the MOID evaluation according to Gronchi et al.. The last is a time filter, that is used to check the possibility of a close approach, without the computation of the minimum distance, by generating windows around the MOID points and checking for possible intersection in time. Also this filter will be largely described in Chapter 2.

1.3.2 Past works on fragmentation reconstruction

A brief overview on previously developed methods is important to know how this topic was faced in the past. The first described work is the one proposed by Frey et al. [22]. This work represents the starting point from which the

model developed in this thesis took inspiration. Indeed, the same propagator and the same time span for the propagation are considered. The method devised by Frey exploits mean Keplerian elements for the fragmentation event detection; in particular, he observed that the propagator returned acceptable approximations for the inclination and the right ascension of ascending node of the orbits, and hence these two features can be used for LEO studies. The event detection is carried out propagating back all the considered fragments and looking at possible clustering of objects in the orbits' right ascension of ascension node. Moreover, Frey suggests the use of supervised learning algorithms to be trained, starting from a set of known fragments. The trained algorithm is then exploited to study also unknown fragmentations.
Another work that uses Keplerian orbital elements for the propagation is the one of Dimare et al. [14]. The general idea of the method is the use of some similarity functions (e.g. the D-criterion explained in Section 1.3.1), based on the Keplerian orbital elements, to find the event date and the parent body. The event epoch is searched looking at the minimum in time of the similarity function, since it is assumed that the orbital parameters of the fragments would be similar near the fragmentation epoch. The similarity functions used in the works are based on:

- The D-criterion, exploiting the metrics proposed by Southworth and Hawkins at al.[13], by Drummond et al. [15], and by Jopek et al. [16] (all of them have been introduced in Section 1.3.1);
- The MOID computation (more in detail in Section 2.6);
- The nodal distance.

For the identification of the minimum, they generated a large enough time window around the analysed event, and they used the backward propagation to recover the time evolution of each orbital elements and the computation, at each time step, of the similarity function. They tested the method both with the use of simulated data (obtained through the use of the NASA standard breakup model) and with a real fragmentation. The metric of Southworth and Hawkins and of Jopek proved to be the most suitable for both the goals [14]. However, the method was validated for a time span of about one months, and hence the validity on a longer time is not assessed.
Romano et al. [23] proposed a new method, this time based on osculating orbital elements. Romano exploits SGP4 propagator since the time frame analysed is up to one month from the event epoch. The objectives of his

work are double: the first goal is the detection in space and time of the event, while the second is the modelling (in space) the distribution of the generated fragments. The first goal is achieved looking for convergence in the space orbital region of the fragments considered for the analysis. The latter is performed exploiting the triple-loop filter proposed by Hoots et al. [21] (and described in detail in Section 2.6) to reject from the process possible objects that are not related to the event analysed (e.g. fragments of satellite that belongs to other fragmentation events) and to search possible close approaches between the fragments included in the studied set. The objects that survives after the triple-loop filter are subdivided into different families exploiting the HCM (described in Section 1.3.1), since objects originated from the same parent are likely to have similar orbital parameters. The final set of objects is matched with a set of possible parent candidates to identify possible parent and their orbital informations. The latter are then used to characterise the fragmentation exploiting the NASA standard breakup model [24] to statistically recover the physical properties associated to each fragment. At the end, all the previously obtained informations are used to model the distribution of the orbital parameter of all the possible generated fragments.
A last analysed method is the one proposed by Andrisan et al. [25], developed as a project for the ESA. One of the tools of the project, the Simulation of On-Orbit Fragmentation Tool (SOFT), is dedicated to the determination of the type of fragmentation (in case new debris are detected by a space surveillance network), to the location in space and time of the event, and to find the objects involved. Firstly, the type of fragmentation is identified looking at the classical orbital elements; in case large differences between the elements of the new fragments are observed, they assume the event to be a collision, otherwise the event is treated as an explosion. The event detection and the parent identification is carried out by computing, at each time step, the position of the center of mass of the analysed fragments, along with the distance of each fragment and the position of the center of mass and the correspondent averaged value. The time step for the backward propagation is not fixed, and it varies in case the averaged distance is smaller than threshold (selected as 50 km [25]); the process goes on until the minimum value is reached. The velocity and the position of the parent orbit are computed as an average between those of the fragments. These two values are then matched with a catalogue to find the possible parent candidates:

- for events occurred on equatorial orbit, the perigee and apogee altitudes are used for the parent comparison;

- for events not occurred on equatorial orbit, the inclination and the right ascension of ascending node are used for the parent comparison.

1.3.3 Ballistic coefficient estimation

The ballistic coefficient is an extremely important physical parameter, that is also needed to evaluate the time evolution of the orbital elements. This coefficient has to be recovered by the B^*, that is a parameter included in the TLE sets (that are the data format used to recover the initial orbital elements, as explained in Section 2.3). The basic idea shared by all the techniques is to consider that the variation in the semi-major axis (included in the TLEs as mean motion) is only related to the drag influence. In this way, by comparing the variation of the elements presented in the history of the considered TLEs and the one obtained through a different propagation it is possible to recover a suited estimation of the BC.
Dolado Perez at al. [26] proposed a method to estimate the area-to-mass ratio for both the drag and SRP effects separately. They needed the estimation of this values to properly initialise the orbit determination process. As a first approximation, the area-to-mass ratio for the drag and SRP effects are considered as equal (since the objects are considered as randomly tumbling) and are preliminarily estimated using the variation of the semi-major axis due to drag. A more refined estimation is computed by analysing the variation in the TLEs. Indeed, the idea is to recover two coefficients, K_1 and K_2. that solve the following system of equations

$$\left.\frac{da}{dt}\right|^{TLE} = K_1 \left.\frac{da}{dt}\right|^{drag} + K_2 \left.\frac{da}{dt}\right|^{srp} \tag{1.10}$$

$$\left.\frac{de}{dt}\right|^{TLE} - \left.\frac{de}{dt}\right|^{cons} = K_1 \left.\frac{de}{dt}\right|^{drag} + K_2 \left.\frac{de}{dt}\right|^{srp} \tag{1.11}$$

where $\frac{d}{dt}$ is the variation in time of the parameter begin considered.

For each considered TLEs set, a couple of K_1 and K_2 can be computed following the procedure described below [26]:

1 The mean of the time derivative of the semi-major axis cumulated from the epoch of the first TLE in the catalogue up to the current TLE is computed (based on the TLE fitting);

2 The mean of the contributions to the semi-major axis (drag and SRP) cumulated from the initial epoch up to the current epoch is computed (based on the fitting of propagated values);

3 The same goes for the eccentricity;

4 The system of Eq. 1.10 and 1.11 can therefore be solved.

The main problem of this procedure arises from the fact that, at low altitudes, the SRP contribution is of many order of magnitudes lower than the drag one, giving rise to wrong results. Consequently, . Gondelach et al. [27] present another technique, based only on the variation due to the drag effects. The idea is the same as the one previously described, that the variation in the semi-major axis in the TLEs is related to drag only; hence, by propagating the orbit exploiting all the considered perturbations and recovering the time variation of the semi-major axis due to drag only, it is possible to estimate the needed ballistic coefficient. It is worth to mention that a loop is performed till the convergence of the method, that is when the variation in the semi-major axis of the TLEs and the one performed by the propagator are similar enough, that is when the relative difference is below a given tolerance. This method is further analysed in Chapter 2. Moreover, the method proposed by Gondelach was also applied to re-entry prediction by Frey et al. [28].
It is worth to mention that the estimation of the ballistic coefficient of all the space objects is an open question in the space research field. Indeed, many uncertainties, mainly related to the estimation of real word physical properties, such as the atmospheric density or the solar cycle influence, are difficult to be covered perfectly.

1.4 Scope of the thesis

The proposed work aims at characterising possible occurred fragmentations (i.e., explosions and collisions) from different points of view. On one side, the objective is to find the objects involved in the event, starting from an initial set of undefined objects in the form of Two-Line-Elements (TLEs), and to localise it in space and in time. On the other side, it is important to identify, within a set of possible candidates, the parent body (or bodies) which originated the fragments. The whole study is carried out focusing only on the LEO region. Indeed, each region has its own peculiarities, making the problem slightly different for different space regions. The time frame taken into account for the localisation of events is in the order of months up to years, hence considering the long-term evolution of the fragments' orbits. Moreover, mean Keplerian orbital elements are considered for the propagation. The choice of a long time span for the propagation, along with the

use of mean elements, requires to have high accuracy in estimating some parameters (e.g. the ballistic coefficient). Indeed, the more the initial time of the propagation goes far from the event date, the more the accuracy in the propagation (and in the parameters useful for it) plays an important role, making the study more complex than considering short time spans for the event detection. This thesis is part of the COMPASS project: "Control for orbit manoeuvring by surfing through orbit perturbations"(Grant agreement No 679086). This project is European Research Council (ERC) funded project under the European Union's Horizon 2020 research. This work within the COMPASS project complements the work performed by Romano et al. [23]. which reconstructs fragmentation on the short range exploiting the SGP4 propagation is part of performed within the European Commission Framework Programme H2020 "SST Space Surveillance and Tracking" contracts N. 785257 (2-3SST2016). The main difference is, as well stated before, the time span of the study, here months, there days.

1.5 Structure of the thesis

After this brief overview of the problem, the following chapters are organised as follows. Chapter 2 is dedicated to the detailed description of all the tools that are exploited in the model; some of them have been already presented in Section 1.3 and will be further characterised, while others will be introduced for the first time. Chapter 3 is dedicated to the description of the model proposed to identify possible fragmentation starting from a set of objects. All the phases and passages will be presented in a detailed way. Chapter 4 describes the part of the model dedicated to the parent body identification. Chapter 5 is dedicated to the validation of the models described in the previous two chapters; the validation is performed by applying such models to test cases and discussing the results. Chapter 6 the final considerations and the presentation of possible improvement and future works related to the presented work.

Chapter 2

Theoretical models for fragmentations

Within this chapter are illustrated features that characterise the tools exploited in the models for the fragmentation events detection and the parent body(s) identification, including their strengths and their limitations. Some of them have already been introduced in the previous chapter, while others are being introduced for the first time. First of all, Section 1.2 describes the main characteristic of the LEO region. Section 2.3 briefly introduces the TLEs, the data format with which information about the objects is taken. Then, since these data might contain errors, in Section 2.4 it is presented an outlier filter. Section 2.5 shows how the ballistic coefficient of each object is estimated from TLEs data. Pruning and clustering algorithms, exploited to find possible families, are reported in Section 2.6. Section 2.7 presents the Gabbard diagram [29], a powerful tool useful to analyse fragmentation events.

2.1 Low Earth orbit main perturbations

As per definition, the LEO is the region of the space around the Earth characterised by an apogee altitude between 0 and 2000 km, and by a perigee altitude between 0 and 2000 km [2]. Due to this characteristics, the region is highly influenced by the perturbation due to Earth's non spherical gravitational field and the aerodynamic drag. This two may be considered as the main perturbations in this sector of the space. Other perturbations that have to be considered, also through possible resonance between different type of perturbations, are the Solar Radiation Pressure (SRP) and the

third-body perturbation (e.g. luni/solar perturbations). A detailed analysis of the perturbation is reported in

2.1.1 Perturbation due to Earth's non spherical gravitational field

The perturbation due to Earth's non spherical gravitational field is of great importance for objects orbiting near the Earth (and generically for objects orbiting around a celestial body). The contributions related to the non-spherical conformation of the Earth have to be added to the principal gravitational potential (obtained when considering the gravitational field as spherical). The gravitational potential energy is modelled through the use of the potential function

$$U(r) = -\frac{\mu_E}{r} \tag{2.1}$$

where μ_E is the Earth gravitational parameter and r is the geocentric distance (with the reference system centered in the Earth center). This leads to a force applied to the orbiting body equal to

$$\underline{F} = -\frac{\mu_E \cdot m_b}{r^3}\underline{r} \tag{2.2}$$

where m_b is the mass of the orbiting body.
Additional potentials are added to account for the non-sphericity of the Earth. The non-spherical contribution can be subdivided in two contributions: the zonal harmonics and the tesseral harmonics (that includes the sectorial harmonics). Consequently, the potential function becomes [30]

$$U(r, \phi, \lambda) = \frac{\mu_E}{r}(-1 + U_{ZH} + U_{TH}) \tag{2.3}$$

where ϕ is latitude and λ is the longitude of the objects position, while U_{ZH} and U_{TH} are the zonal harmonics and tesseral harmonics potential, respectively. Both the potential are expressed through the use of Legendre polynomials. The zonal harmonics potential is evaluated as

$$U_{ZH}(r, \phi) = \sum_{n=1}^{\infty} J_n \big(\frac{R_E}{r}\big)^n P_n(\cos\phi) \tag{2.4}$$

where R_E is the Earth radius, P_n are the Legendre polynomials of degree n and J_n are empirically determined coefficients to the Legendre polynomial of degree n. An important contribution is related to the so called J_2 effects that is related to the Earth oblateness or the equatorial bulge. Indeed,

among all the zonal harmonics contribution, this one plays the most important role since it is some orders of magnitude higher than the others. To the J_2 effects are associated the secular effects on the right ascension of the ascending node, on the argument of perigee and on the true (or mean) anomaly, while the other Keplerian parameters are not affected. The tesseral harmonics potential is expressed as [30]

$$U_{TH}(r,\phi,\lambda) = \sum_{n=1}^{\infty}\sum_{m=1}^{m}\left(\frac{R_E}{r}\right)^n (C_{nm}\cos m\lambda + S_{nm}\sin m\lambda)P_{nm}(\cos\phi) \quad (2.5)$$

where C_{nm} and S_{nm} are empirically determined coefficients from observations [10]. The tesseral harmonics play a less predominant role for objects in LEO region than the zonal harmonics one; however, for more refined method, their effect has to be considered.

2.1.2 Aerodynamic drag

The aerodynamic drag is a perturbation strictly related to the Earth's atmosphere. Typically, space is set to 'begin' at 100 km altitude and even though almost the totality of the atmosphere lies below this altitude, the air density at altitude higher than 100 km is high enough to exert a force on space objects [31]. The main effects of the atmospheric particles are the aerodynamic drag and aerodynamic heating, which affect the evolution of all space objects. Due to the decay with altitude of the air density, the atmospheric drag most strongly influences the motion of a satellite below 800 km [10], while other perturbations are more relevant at higher altitude [10]. The aerodynamic drag is a non-conservative perturbation, and its perturbing acceleration is expressed as

$$\underline{a}_{Drag} = -\frac{1}{2}\rho(t,h)\frac{c_d \cdot A_{cross}}{m_b} v_{rel}^2 \frac{\underline{v}_{rel}}{\|\underline{v}_{rel}\|} \quad (2.6)$$

where ρ is the atmospheric density (at altitude h and time t), c_d is the drag coefficient, A_{cross} is the cross-sectional area that is perpendicular to the relative velocity $\underline{v}_{rel}$ (i.e. relative to the atmosphere rotation). As observable in Eq. 2.6, the aerodynamic drag is both related to physical properties of the space objects and to the atmosphere characteristic. All the physical properties can be summarised in an unique parameter, named the ballistic coefficient

$$BC = \frac{c_d \cdot A_{cross}}{m_b} \quad (2.7)$$

The atmospheric characteristics are instead more complex to be recovered and to be modelled. Indeed, the majority of the uncertainty in modelling the effect of the drag is associated to the estimated value of the density. Indeed, the density vary both with altitude and with time, and its estimation is related to many effects which alter it.
Density can be modelled either as static or time-varying; but even in the static case, it is necessary to account for spatial variation (i.e. latitudinal and longitudinal variations [10]). Time-varying models, which are more complex since consider more real effects, include more influencing factors:

- Diurnal, Seasonal, and Semi-annual variations;
- Rotating atmosphere, winds, and tides;
- Magnetic-storm and irregular short-periodic variations;
- Cyclical variations;
- 27-day solar-rotation cycle and 11-year cycle of Sun spots.

Different atmospheric density models have been presented over the years; among the others, it is possible to cite the Jacchia-Roberts, the US Standard Atmosphere 1976 and the NRLMSISE-00 models [10]. The Keplerian parameters more influenced by the drag are the semi-major axis and the eccentricity, leading to a circularisation and size reduction of the orbit.

2.1.3 Third-body perturbation

The effects of the gravitational attractions of other celestial body different from the Earth are considered as third-body perturbations. Indeed, since a two-body problem is considered for the propagation, all external bodies will affect the motion of space objects. However, only the Sun and the Moon produce effects that are measurable [10]. The effect of this perturbation becomes relevant at high altitude, when the contribution related to the aerodynamic drag tend to diminish of importance. The acceleration generated by the effect of a generic third-body is expressed as

$$\underline{a}_{3B} = \mu_{3B}\left(\frac{\underline{r}_{b-3B}}{r_{b-3B}^3} - \frac{\underline{r}_{E-3B}}{r_{E-3B}^3}\right) \tag{2.8}$$

where μ_{3B} is the standard gravitational constant of the considered third-body, the $\underline{r}_{b-3B}$ is the distance from the spacecraft to the third-body and the $\underline{r}_{E-3B}$ is the geocentric distance of the third body.
The principal effects of this perturbation are secular changes in inclination, eccentricity and argument of perigee.

2.1.4 Solar radiation pressure

The last analysed perturbation is the one caused by solar radiation pressure, that is a non-conservative perturbation. The effect is related to photons photons carried by solar radiation, which transfer their momentum to the objects they hit, giving them a boost in velocity. The momentum these photons carry is extremely small. Thus, the perturbing force isn't really observed in LEO spacecraft. The perturbing acceleration is expressed as [30]

$$\underline{a}_{SRP} = P_{SR@1AU} \frac{AU^2}{\left\|\underline{r}_{b-Sun}\right\|} c_r \frac{A_{cr-Sun}}{m_b} \frac{\underline{r}_{b-Sun}}{\left\|\underline{r}_{b-Sun}\right\|} \tag{2.9}$$

where $P_{SR@1AU}$ is the solar radiation pressure at one astronomic unit, c_r is the reflectivity coefficient, A_{cr-Sun} is the cross-sectional area normal to the sun direction, m_b is the body mass and $\underline{r}_{b-Sun}$ is the distance from the spacecraft to the Sun. This perturbation, mainly because directly connected to the Sun, is highly influenced by the solar activity. During high solar activity periods, the effect of the SRP can overcome the effects of other perturbations (clearly depending on the altitude) [10]. The main uncertainty in the SRP models come from the difficulty in modelling the solar cycles and the time spent in the shadow of the orbiting body. The SRP highly influences objects with high surface area and low mass like solar-sails.

2.2 Planetary Orbital Dynamics

The main characteristics of this thesis work are the mid- up to long-term propagation and the use of Keplerian orbital elements. Consequently, a proper propagator has to be selected. Planetary Orbital Dynamics (PlanODyn) suite [1] is a semi-analytic propagator based on single and double averaged dynamics, and it is written in Keplerian orbital elements (or non-singular equinoctial elements). In case the single average approach is considered, the averaging is performed over the orbit revolution of the considered objects around the central body (i.e. the Earth for the thesis work). Depending on the type of the perturbing forces, the planetary equation considered are:

- the Lagrange planetary equation (Battin et al. [32]), used to describe the conservative forces (i.e. gravitational forces associated to the non-spherical central body and the third-body perturbations);

- the Gauss planetary equation (Battin et al. [32]), used to describe the non-conservative forces (i.e. the drag perturbation).

The perturbations available for the propagation are: the atmospheric drag, the zonal and tesseral harmonics of the Earth's gravity potential, the SRP, and the third-body perturbations (i.e. the Sun and the Moon effects). The secular disturbing effect associated to the aerodynamic drag is modelled according to King-Hele et al. [33], that gives a set of semi-analytical expression depending on the drag regimes. The SRP is modelled through a cannonball (i.e. assuming the objects of interest to be a sphere) and ignoring the eclipses (Kirov et al. [34]). The third-body effects are implemented using the model proposed by Kaufman et al. [35], and computing the ephemerides of the perturbing bodies according to Meeus et al. [36]. The geopotential effects are modeled according to Kaula et al [37], for the first-degree expansion of the zonal and of the tesseral harmonics, and according to Brouwer et al. [38] for the second-order zonal harmonic. The flexibility of the force model implemented in PlanODyn allows to select the desired perturbation effects depending on the analysed case. Indeed, depending on the space region and on the time-frame of interest, it is possible that some perturbations are some order of magnitude lower than the others, and hence can be neglected.

2.3 Two-Line-Elements

Two-Line-Elements (TLE) are publicly available data, generally used to perform orbital mechanics analysis whenever more accurate orbital data are not available. This type of data is used through simplified perturbation models like the SGP4 [39]; however, the latter are not exploited in this work since their validity is generally considered of the order of few days [40], hence not suitable for longer propagations.
The orbital elements included in the TLEs are mean Keplerian elements (computed through SGP4/SDP4 orbital model), since short-periodic variations are removed. Moreover, they are represented in the True Equator Mean Equinox (TEME) reference frame [39], that is the same adopted by the propagator used for this work.
An important parameter included inside the TLEs is the B^*, that is a way of modeling the influence of the aerodynamic drag on the satellite. In this form, it is directly used to recover the aerodynamic disturbance with SGP/SDP propagators. Since the propagator adopted here require the ballistic coefficient rater than the B^*, the latter is exploited as a fitting parameter to recover the ballistic coefficient, as explained in Section 2.5. For complete-

ness, Appendix B reports the format of the TLEs and a brief description of each included parameter. The data needed for the analysis is taken from `www.space-track.org`.

2.4 TLEs filtering outlier

Since TLEs may include some mistakes inside their parameters, there is the need of filters that succeed in their identification and elimination. This improves the accuracy of the study since it increases the accuracy of the input data. The filter described in the following subsections has been proposed by Lidtke et al. [41]. The parameters analysed by the filter are the mean motion, the inclination, the eccentricity, the time of update of the TLEs, the sign of the B*. Once the filtering is complete, the majority of the outliers have been eliminated. Indeed, it is not possible to eliminate all the outliers with an automatised tool, because some outliers are difficult to find also by an human operator. Moreover, some outliers remain below the tolerance considered for the type of study of this work and consequently are not considered as completely wrong. It is also important to mention that the data exploited for the tests does not cover the entire life of the objects, but rather contain only a small portion; this partially reduces the efficacy of the filter since the global behavior of the evolution of each considered parameter is lost. The following subsections introduce each filter.

2.4.1 TLE update time

The first check is performed over the update time of new TLEs, that is how often a new TLE is updated. The update time is not constant, but some recurrent features may be identified. Among the others, short update times (i.e. two updates of the same object that occur with a too small time difference) are extremely important; indeed, this is a signal of possible errors, since the latest update could be a correction of the previous TLE.
To counter this possibility, it is essential to define a time threshold to identify possible correction. For the filter used here, the threshold value selected to consider a new update as a correction is of half an orbit (i.e., the semi-period of the orbit). Sometimes it is possible that even the new update is affected by errors. However, the check is performed for each TLE included in the set and, moreover, this is only a preliminary filter.

2.4.2 Large time gaps

A second check is performed on the update time, this time focusing on the presence of large time distance between two consecutive TLEs. In case the update of a new TLE took place after a long time, it may be possible that the the new TLE and the previous one are no more correlated between each other in terms of variation of the orbital elements. Indeed, it possible that, in the interval where data points are missing, some events may have occurred. To overcome this problem, the analysed TLEs set is subdivided into windows, each of which does not contain large time gaps. Once the windows are generated, the other filters are applied separately to each window.
Figure 2.1 shows an example of a TLEs set (NORAD ID 13025) in which are detected some time gap. From the cumulative number distribution (displayed in the image on the top) it is possible to observe that the majority of the updates occurred within 10 days, while in some cases the update times have been longer. The figure on the bottom shows instead the windows generated by the algorithm. The red dots are the edges of each window, while the blue dots are the TLEs included in the set. As observable, the method is capable of properly identify large time gaps and to generates appropriate windows.

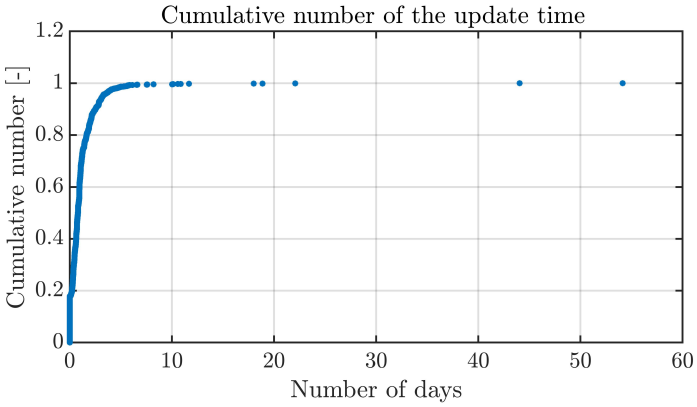

(a) *Cumulative number vs number of days*

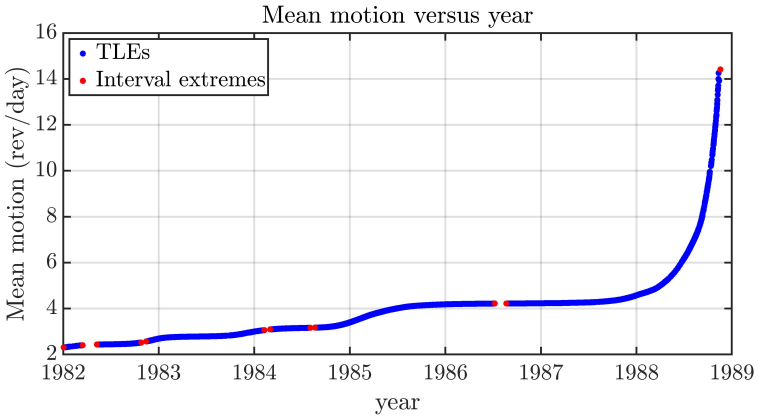

(b) *Mean motion evolution vs time*

Figure 2.1: High update time example

2.4.3 Mean motion

Inside the TLEs, the semi-major axis is not directly included, but can be recovered from the mean motion. This parameter is directly connected with the orbital energy. Due to the change in the energy, mainly by the drag for the type of objects considered, there will be a change in the mean motion. Some times it is possible to observe some erroneous values inside the evolution in time of this parameter. The filter adopted to localise possible outliers in the mean motion history is based on a regression technique. The method is based on a sliding window (of a fixed length), within which TLEs are scanned, and a regression computation with the use of a polynomial of a chosen order. With the regressed polynomial obtained, the following two TLEs in the series are analysed. The regression of the data is useful to predict the theoretical evolution of the mean motion and to compare it with the one contained inside the TLEs. Indeed, the predicted values is exploited to compute two different tolerances, an absolute tolerance T_A and a relative tolerance T_R. The absolute tolerance is evaluated as [41]

$$T_A = \frac{n_i - n_{reg}(t_{i+1})}{n_{reg}(t_i)} \tag{2.10}$$

where n_i is the elements i-th in the sliding window, $n_{reg}(t_i)$ and $n_{reg}(t_{i+1})$ are the mean motion evaluated through the regression technique of the i-th and (i+1)-th elements.
On the other hand, the relative tolerance is evaluated as [41]

$$T_R = \frac{n_i - n_{reg}(t_{i+1})}{n_{reg}(t_i) - n_{reg}(t_{i+1})} \tag{2.11}$$

Two different threshold values are set for the two tolerances and, if both are exceeded at the same time, it is necessary to evaluate a further tolerance. Indeed, the analysed elements might not be an outlier but rather there could be a change in the evolution of the mean motion (e.g. a maneuver).
The new tolerance is [41]

$$T_{Ai+1} = \frac{n_{i+2} - n_{i+1}}{n_{reg}(t_{i+1})} \tag{2.12}$$

If also the threshold of this last tolerance is exceeded, the TLE is considered as an outlier; on the contrary, if the the value stays below the threshold, the element is considered as correct. In the latter case, since there is a change in the properties, the original window defined through the previous filters is further subdivided creating sub-windows, within which the following other

filters are exploited.

2.4.4 Eccentricity and inclination

A more statistical approach is applied to the filter that involves the inclination and the eccentricity. The latter is not analysed directly; rather the perigee distance is evaluated. The mathematical tools used here are the median, the mean, and the median/Mean Absolute Deviation (MAD). This statistical tool is usually exploited to find out possible outliers and to eliminate them. As in the preceding filter, here a sliding window is scanned through the sequence of inclination ad eccentricity; obviously, two separated windows are considered for each Keplerian element. As the window slides along the inclination/perigee radius sequence, the mean value is evaluated, and the latter is subtracted from the central element of the window. In this way, the sequence becomes a time series of differences. Then, another sliding window scans the time series of differences and the MAD (here intended as mean absolute deviation) is evaluated. In the end, all the elements that present a difference from the mean value equal to a fixed number of MAD are considered as outliers and eliminated. It is important to note that more than one passage for each sequence can be performed to eliminate the outliers at different level of precision, each time considering different values for the windows length.

2.4.5 Negative B^*

Negative values of B* are generally associated to maneuvers, hence non-natural change of the body trajectory, or are caused when the effects of drag are overcome by other perturbations [10]. Since the objects used for this work are not active objects, negative values of B^* are eliminated. The filtering is performed by the use of a simple sign check.

2.4.6 Otulier filter flowchart

Figure 2.2 summarise the steps of the previously introduced outlier filter.

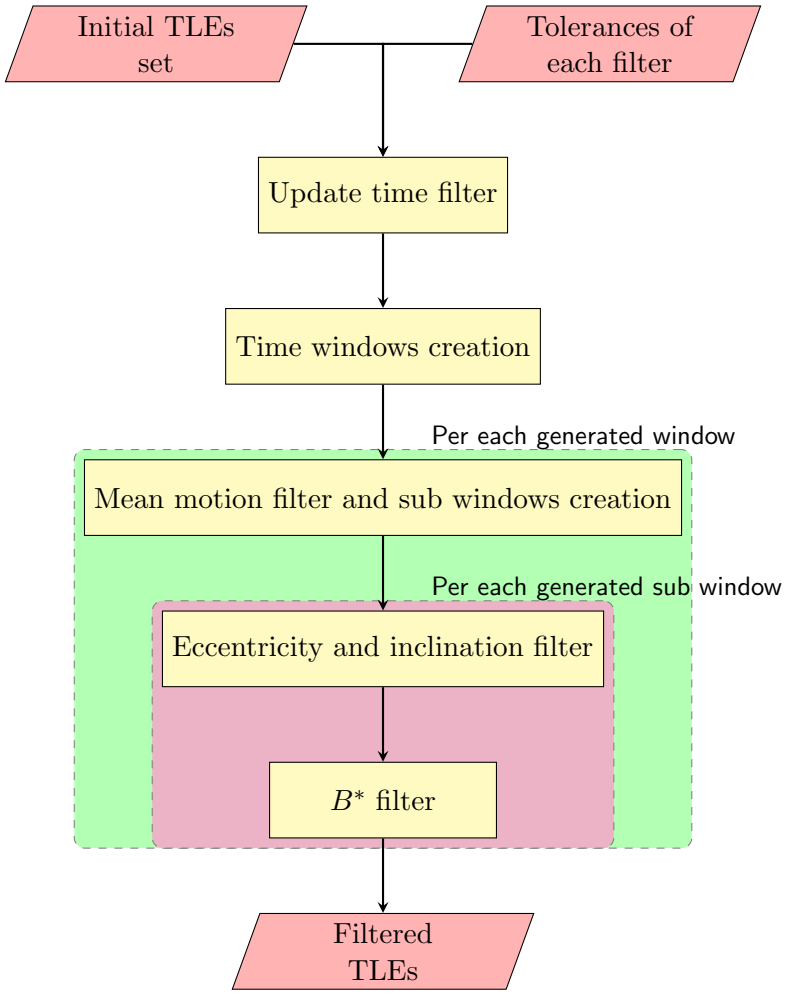

Figure 2.2: Outlier filter flowchart.

2.4.7 Filter example

The example proposed here considers the TLEs set of an Iridium 33 debris, that is the 97051 L (NORAD ID 33761). To check the validity of the filter, some large outlier values are inserted randomly inside the original set: 3 outliers for the mean motion, four for the eccentricity, and four for the B^*. On the contrary, no outliers are inserted to check the correction filter, but rather the already present errors are considered. As observable in Figure 2.3, the filter is able of detecting the presence of wrong values (red dots) and of eliminating them.
It is worth to make a last consideration concerning the weight of the outlier error with respect to the correct trend of the analysed parameter. Even though looking at the pictures (that show the evolution in time of a parameter along with the included outlier) the error between the outlier value and the correct trend appear high, it is possible that the severity of the error may not be equally high. As an example, considering the first outlier in the mean motion and computing its correspondent semi-major axis, it is possible to observe that the error with respect to the correct evolution is about 80 m. Considering typical values of the order of kilometers when studying collision avoidance or close approach cases, the error obtained here stays below these typical thresholds. Consequently, in the case the outlier has not been localized by the filter, the accuracy may not suffer from the error.

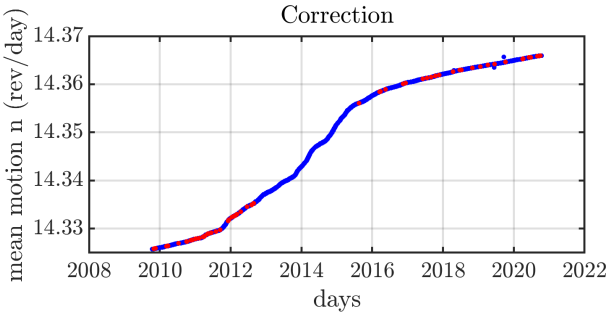

(a) *Correction filter*

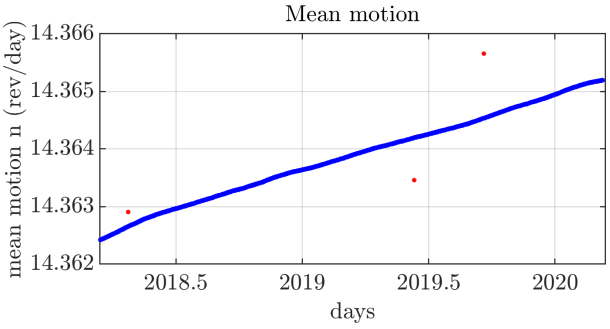

(b) *Mean motion filter*

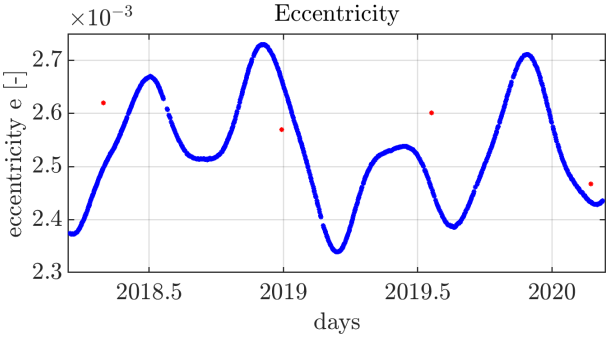

(c) *Eccentricity filter*

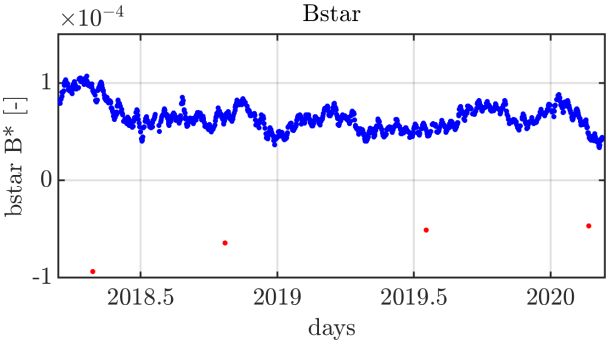

(d) *B* filter*

Figure 2.3: TLEs filter example

2.5 Ballistic coefficient

As previously stated in Section 1.3.3, the ballistic coefficient (BC) is an important physical property of each body. Moreover, the propagator used within this thesis work requires its estimation to recover a precise time evolution of the objects.
The BC is generally defined as

$$BC = \frac{m_b}{c_d \cdot A_{cross}} \tag{2.13}$$

where m_b is the mass of the body, c_d is the drag coefficient, and A_{cross} is the cross-sectional area of the body.
The work of Gondelach et al. [27] presents a strategy to estimate the ballistic coefficient, starting from the analysis of the B^*. As reported in Eq. 2.14, a first approximation of the ballistic coefficient can be performed through the Vallado formulation [42]:

$$BC = 12.741621 \cdot B^* \tag{2.14}$$

This approximation is not very accurate, but it is good enough to be used as a first guess in the estimation process. The first step is to recover the change in the semi-major axis Δa between two TLEs. Since the semi-major axis is not directly included inside the TLE, the latter is computed through the 'mean' mean motion n_o, that is instead available in each TLE:

$$a_{TLE} = \left(\frac{\mu_E \cdot 86400^2}{\pi^2 n_o^2}\right)^{1/3} \tag{2.15}$$

where μ_E is the standard gravitational parameter of the Earth (considered as $\mu = 398600\ km^3/s^2$). Consequently, the variation in the semi-major axis is computed as

$$\Delta a_{TLE} = a_{TLE_2} - a_{TLE_1} \tag{2.16}$$

Then, the variation in the semi-major axis is estimated with the propagator, in order to compare the two changes. As per definition, it is possible to assume that the change in the semi-major axis between two TLEs is caused by the aerodynamic perturbation only. Even if long-periodic variations of the semi-major axis (related to gravitational and SRP effects) may be included in the TLEs, their contribution is generally negligible [43].
The orbital parameters are propagated considering all the perturbations that affect the objects during their motion; parallel to that, the variation of the

semi-major axis with time due to drag is evaluated at each time step as

$$\frac{da}{dt}\Big|_{drag} = 2\frac{a^2}{\sqrt{\mu p}}\Big[f_{r_{drag}} e \sin\theta + f_{t_{drag}}\frac{p}{r}\Big] \tag{2.17}$$

where p is the semi-latus rectum, θ the true anomaly, $f_{r_{drag}}$ and $f_{t_{drag}}$ the acceleration due to drag in radial and transverse direction, respectively. The variation in the semi-major axis is recovered integrating the previous expression in time

$$\Delta a_{prop} = \int_{t_1}^{t_2} \frac{da}{dt}\Big|_{drag} dt \tag{2.18}$$

Once both the variations are available, a check it is performed to see if it is possible to stop the process. A simple secant method is exploited to update the BC estimation, as observable in eq. 2.19.

$$BC_n = BC_{n-1} - \Delta a_{DIFF}(BC_n - 1)\frac{BC_{n-1} - BC_{n-2}}{\Delta a_{DIFF}(BC_{n-1}) - \Delta a_{DIFF}(BC_{n-2})} \tag{2.19}$$

where BC_n is the n^{th} BC estimate and $\Delta a_{DIFF} = \Delta aTLE - \Delta a_{PROP}$. As a first try, since only a single estimation is available and the Secant method requires two guesses values, a second estimation is recovered from the first guess as follows

$$BC_2 = \frac{\Delta a_{TLE}}{\Delta a_{prop}(BC_1)} BC_1 \tag{2.20}$$

where BC_1 is the estimation computed through the Vallado expression. The procedure is repeated until Δa_{DIFF} goes below the threshold value of $10^{-4} km$ [27]. As evident from the preceding description, many parameters affect the estimation of the BC; among them, it is necessary to cite the atmospheric model and the date range within which the estimation is conducted; the latter could be high in case many TLEs are available for the study or low in case few elements are considered for the analysis. The date considered for the estimation is another source of error in the estimation process producing over/under estimated values, that inevitably decrease the accuracy of the propagation and of the all study. Indeed, depending on the date it is possible that the accuracy in the reconstruction of the parameters suitable for the BC estimation is lower than in other cases. Moreover, it is possible to have a worse correspondence between the B^* and the model adopted for the fitting.

Before proceeding with a series of examples, it is important to highlight that

a bad evaluation of the BC not only affects the evolution in time of the semi-major axis (and consequently of the altitude of the orbit), but rather affects also the variation of other parameters like the Keplerian orbital angles (e.g., the right ascension of ascending node and the argument of perigee).
Figure 2.4 shows the steps of the BC estimation process.

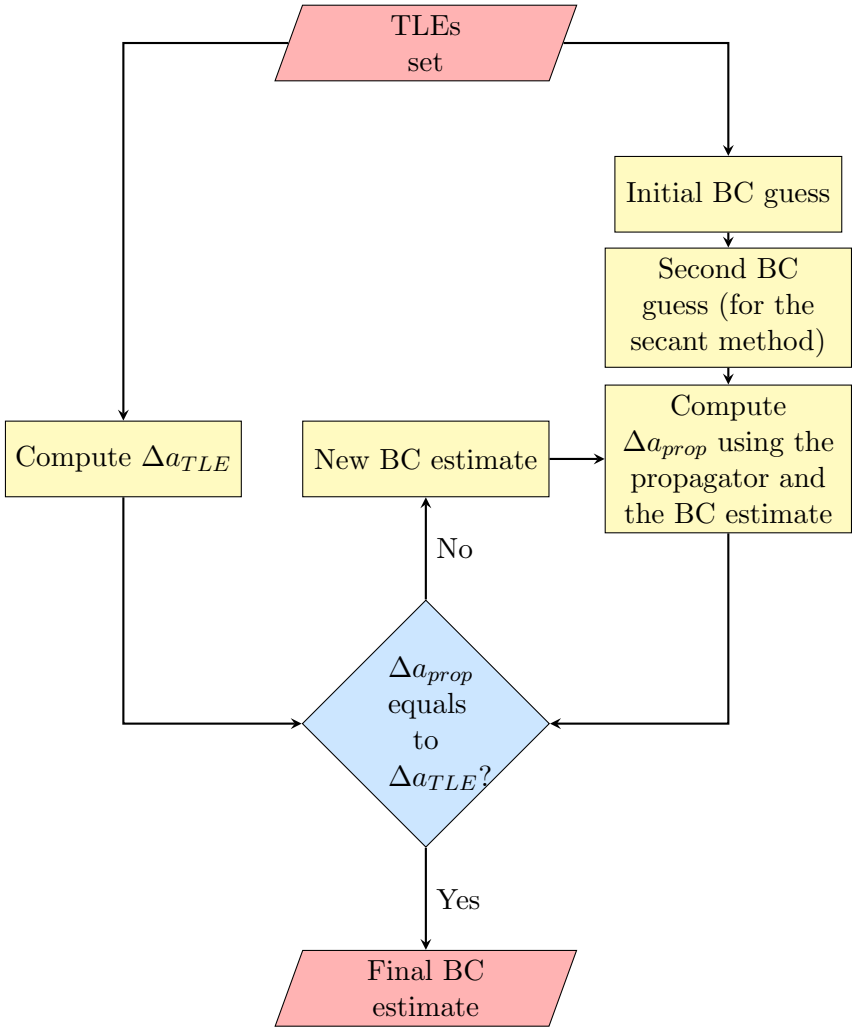

Figure 2.4: Event detection flowchart.

2.5.1 BC estimation examples

The examples presented here are useful to point out how the ballistic coefficient estimation is conduced in the model introduced in the next chapters. A compromise is necessary between the accuracy of the propagation and the computational time of the process; a larger number of elements might seem a better choice for the estimation process. However, the computational time required increases as well, especially if a high number of objects is considered for the analysis.
The first analysis performed here considers an Iridium 33 fragment (NORAD ID 33772) and its TLEs of the year 2013. The estimations showed in Figure 2.5 is performed considering a daily time interval for the single BC estimation and the procedure is repeated for an entire year.

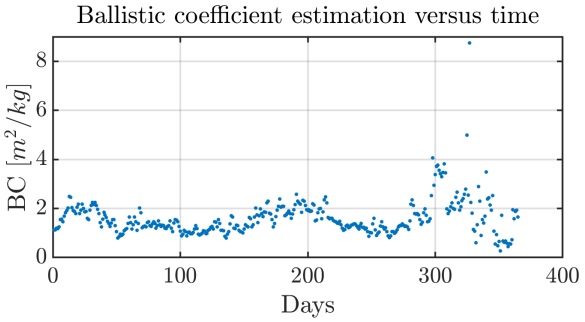

(a) *Daily solar flux.*

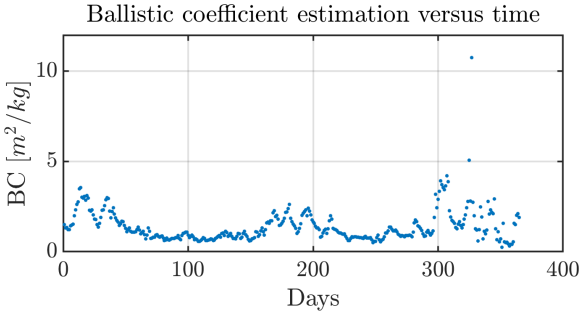

(b) *Sinusoidal solar flux.*

Figure 2.5: BC estimation as function of time and of the solar flux model.

The picture on the top considers a daily[1] solar flux model to recover the time evolution of the atmosphere density (needed in the drag model), while on the bottom it is exploited a much simpler sinusoidal model for the solar flux. As observable, the estimation reported on the top seems to be more bounded around the mean value while on the bottom it is observed a higher oscillation; the latter is probably related to the lack of accuracy in the sinusoidal model. However, in both the cases it is interesting to note that, even considered a high number of estimations, it is not always possible to recover a good final guess. As an example, the estimates located between 150-th and 200-th days include many values far from the mean one, and hence could result in a worse final guess. Moreover, it is noticeable that performing the estimation process on different dates leads to a different BC as well.
Figures 2.6 and 2.7 show the evolution in the semi-major axis and in the perigee and apogee altitudes in time of the previously introduced fragment, respectively. The estimation is performed daily for the single BC in a time window of seven days. The reconstruction seems accurate for the long time span considered for the propagation. The error in the final semi-major axis is about 1 km, that is of the same order of magnitude of typical thresholds adopted for collision avoidance or close encounters studies.
The same test is performed considering the sinusoidal model for the solar activity. From figures 2.8 and 2.9 it is evident that the approximation is degraded by the use of the sinusoidal model.

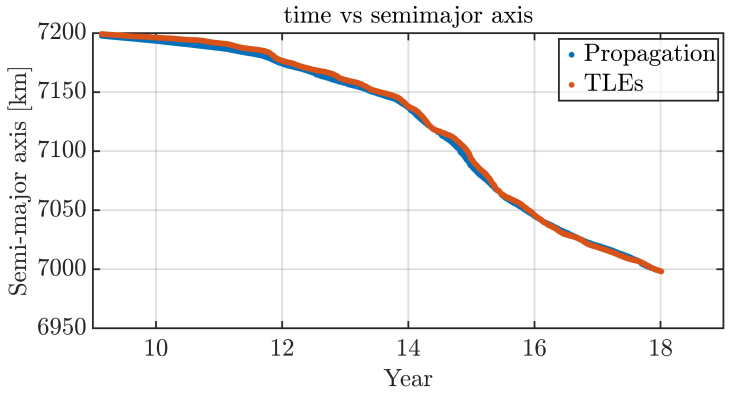

Figure 2.6: Semi-major axis evolution over time - daily solar flux.

[1]The atmospheric model used here is presented in the paper of Frey et al. [44]

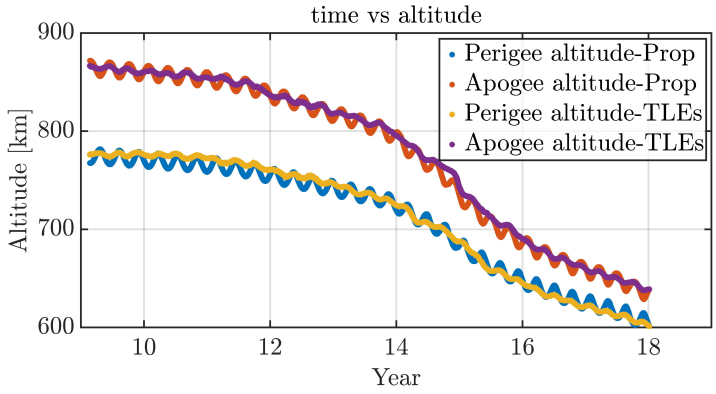

Figure 2.7: Apogee and perigee altitudes evolution over time - daily solar flux.

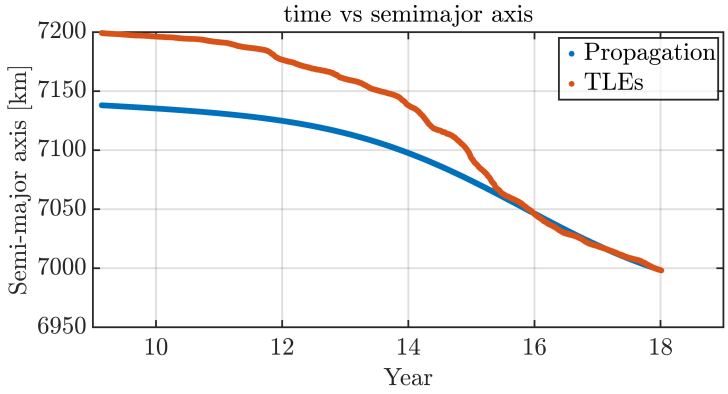

Figure 2.8: Semi-major axis evolution over time - sinusoidal solar flux.

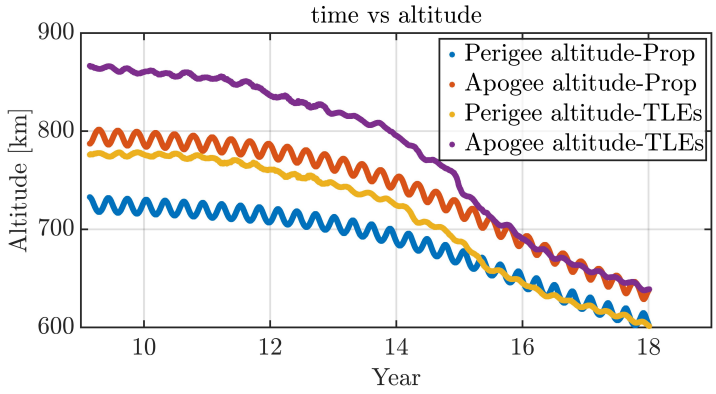

Figure 2.9: Apogee and perigee altitudes evolution over time - sinusoidal solar flux.

However, this behaviour is not a general rule for any estimation. An example is proposed in figures 2.10 and 2.11 for the new daily case, and in figures 2.12 and 2.13 for the new sinusoidal case. The initial propagation date is changed and hence a different estimation derives from the process. As clearly evident, in this second case the sinusoidal model works better than the daily one. This is probably related to the choice of the the date in which it is performed the estimation process.

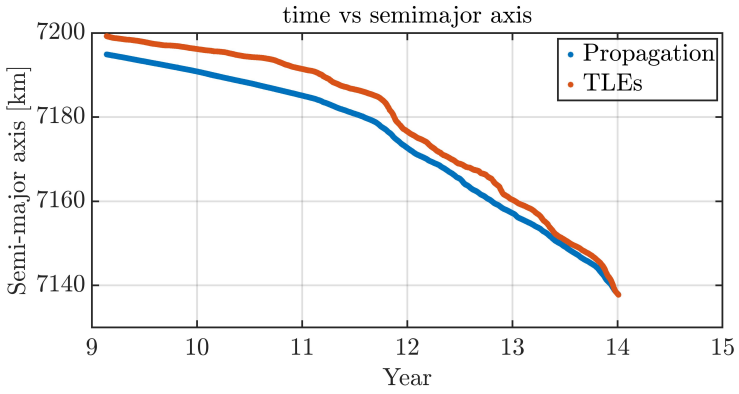

Figure 2.10: Semi-major axis evolution over time - daily solar flux.

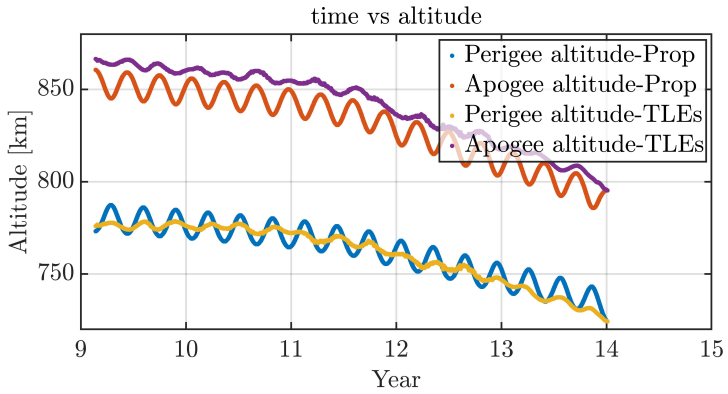

Figure 2.11: Apogee and perigee altitudes evolution over time - daily solar flux.

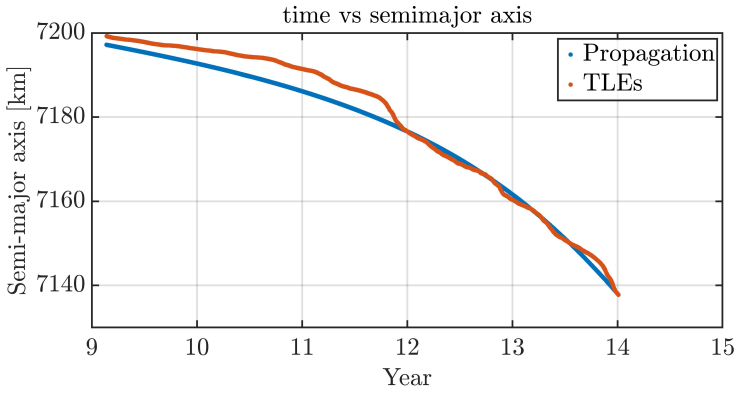

Figure 2.12: Semi-major axis evolution over time - sinusoidal solar flux.

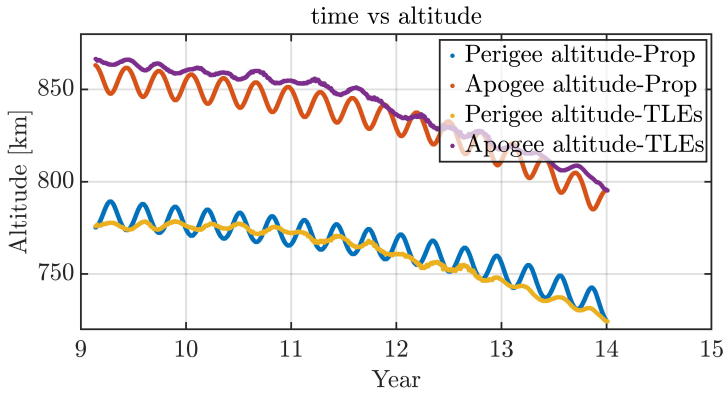

Figure 2.13: Apogee and perigee altitudes evolution over time - sinusoidal solar flux.

2.5.2 BC final considerations

Three main problems affect the BC estimation: the B^* itself since, as previously stated, it is not directly linked to the drag perturbation, possible shortcomings in the drag model, and the fact that fragments typically exhibit an higher value of area-to-mass ratio than satellites or upper stages. The latter entails an higher influence of all the disturbances in which this physical property is involved.
Following all the previous considerations, it is possible to state that the bad estimation of the BC, which affects the entire propagation process, introduces strong limitations to the entire model. Near solar minimum or for not extremely long propagations the accuracy seems to be acceptable. For much longer propagations the accuracy tends to decrease, especially for the

semi-major axis, also by considering a daily solar flux for the drag computation. This happens because of the lack in BC estimation precision. Due to high computational time, the sinusoidal representation of the solar flux is adopted to perform tests in Chapter 5. Consequently, when analyzing the results it is important to have in mind all these limitations.

2.6 Triple loop filter

The triple-loop filter is usually exploited to check if possible close encounters between objects may occur. The filter consists of three steps, two geometric comparisons and one time scanning. The model presented here is inspired by the one proposed by Hoots at al.[21]. Some modification have been introduced, mainly related to the estimation of the MOID.
The check in each filter is performed using two bodies, a target body and a comparison body.

2.6.1 Apogee-perigee

In order to avoid considering objects which are completely uncorrelated with the target one, this first geometric filter is used to eliminate all the objects for which the orbit geometry does not allow to have close encounters. The geometric check is related to the conformation of the two orbits with the aim of finding possible geometrical conjunctions between the two orbits. The control is performed by comparing the apogee and the perigee values of the two orbits. More in detail, being q_{max} the largest of the two perigees and Q_{min} the smallest of the two apogees, if

$$q_{max} - Q_{min} < D_{threshold} \tag{2.21}$$

the geometry of the two ellipses allows the presence of intersections and hence of close encounters.
This first geometrical filter is very useful for eliminating the majority of the objects not useful for the analysis.

2.6.2 MOID

The second geometrical filter aims at finding the minimum orbital distance between the two orbits. It is worth noting that this is not the close encounter distance between the two bodies, rather it is a geometrical parameter useful to remove those orbits whose distance is greater than a threshold. Differently from the method proposed by Hoots, here the minimum distance is find

out through the algebraic solution proposed by Gronchi et al. [20]. The method developed by Gronchi allows to find the 16 closest geometrical points between the orbits considered. The one which is interesting here is the global minimum. Indeed, if this distance is too large, then no close approach can occur; otherwise, if this value is low, it is necessary to check the two orbits further.

Mathematical description

First of all, it is important to point out that the method is developed considering orbits with common focus. Moreover, it is based on the localisation of the critical points of the squared distance between two points belonging to two different orbits, defined in [20] as

$$d^2(V, v) = (\underline{\chi_1} - \underline{\chi_2}) \cdot (\underline{\chi_1} - \underline{\chi_2}) \tag{2.22}$$

where V, v are the true anomaly of the first and of the second object respectively, while $\underline{\chi_1}$ and $\underline{\chi_2}$ are the position vectors of the two objects on the orbits. The formulation adopted for the definition of the position vector is the one proposed by Sitarski et al. [45], that is

$$\underline{\chi_1} = R[\underline{\mathfrak{P}} cos(V) + \underline{\mathfrak{Q}} sin(V)] \tag{2.23}$$

$$\underline{\chi_1} = r[\underline{\mathfrak{p}} cos(v) + \underline{\mathfrak{q}} sin(v)] \tag{2.24}$$

where $\underline{\mathfrak{P}}, \underline{\mathfrak{Q}}, \underline{\mathfrak{p}}, \underline{\mathfrak{q}}$ are vectors whose elements are function of the classical Keplerian orbital elements (defined in C.1), while R and r are the distance of the points from the focus of the orbit evaluated with the typical conic equation

$$R = \frac{P}{1 + E\ cos(V)} \tag{2.25}$$

$$r = \frac{p}{1 + e\ cos(v)} \tag{2.26}$$

where P and p are the semilatum rectum of the orbits.
The system of equations to be solved to find the stationary points of the

squared distance is

$$\begin{cases} p(1+E\ cos(V))[sin(V)(K\ cos(v)+M\ sin(v))+ \\ -(E+cos(V))(L\ cos(v)+N\ sin(v))]+ \\ +EP\ sin(V)(1+e\ cos(v))=0 \\ \\ P(1+e\ cos(v))[sin(v)(K\ cos(V)+L\ sin(V))+ \\ -(e+cos(v))(M\ cos(V)+N\ sin(V))]+ \\ +ep\ sin(v)(1+E\ cos(V))=0 \end{cases} \tag{2.27}$$

where K = $\underline{\mathfrak{P}} \cdot \underline{\mathfrak{p}}$, L = $\underline{\mathfrak{Q}} \cdot \underline{\mathfrak{p}}$, M = $\underline{\mathfrak{P}} \cdot \underline{\mathfrak{q}}$ and N = $\underline{\mathfrak{Q}} \cdot \underline{\mathfrak{q}}$.
Then, the problem is transformed into an algebraic one performing a variable change (as suggested in Gronchi et al. [46])

$$\begin{cases} s = tan(V/2) \\ t = tan(v/2) \end{cases} \tag{2.28}$$

After a mathematical rearrangement of the terms, the previously system of equations becomes a polynomial system of the form

$$\begin{cases} f(s,t) = f_4(t)s^4 + f_3(t)s^3 + f_2(t)s^2 + f_1(t)s + f_0(t) = 0 \\ g(s,t) = g_2(t)s^2 + g_1(t)s + g_0(t) = 0 \end{cases} \tag{2.29}$$

where the polynomial coefficients are function of the previously defined Keplerian elements and are showed in more detail in Appendix C.2.
A further modification of the system of equations is carried out with the use the algebraic theory of elimination (proposed by Cox et al. [47]). The theory states that: f(s,t) and g(s,t) have a common factor (as polynomials in variable s) if and only if the resultant Res(t) = Res(f(s,t),g(s,t),s) of f and g with respect to s is zero (from Gronchi et al. [20]).
The resultant is computed through the determinant of the Sylvester matrix associated to the two polynomials (described in C.3), giving rise to a 20^{th} degree polynomial in the variable t (hence reducing the number of variables). After mathematical manipulation of the polynomial coefficients, it is possible to obtain a 16^{th} degree polynomial defined as

$$r(t) = det(\hat{S}(t) = \frac{Res(t)}{[t^2(e-1)-(e+1)]}) \tag{2.30}$$

where Res(t) is the resultant (reported in C.3) of the previously mentioned Sylvester matrix, and $det(\hat{S}(s))$ is the determinant of a modified Sylvester matrix (again defined in C.3). It is important to note that the roots of the denominator, that are $t = \pm\sqrt{\frac{e+1}{e-1}}$, have to be discarded.
To compute the coefficients of the polynomial, the FFT (Fast Fourier Transformation) is exploited, that is particularly efficient when working with a number of evaluations that is a power of 2, while $r(t)$ has 17 coefficient. Consequently, it is is necessary to reduce the degree of the polynomial; this is performed writing

$$r(t) = r_0 + t\ \tilde{r}(t) \tag{2.31}$$

where

$$\tilde{r}(t) = \sum_{j=1}^{15} r_{j+1} t^j \tag{2.32}$$

and where $r_0 = det(\hat{S}(0))$. Then, the evaluation-interpolation method is applied (using the DFT and IDFT) to $\tilde{r}(t)$ whose evaluations in the 16^{th} roots of unity $\omega_k = \exp -2\pi i \frac{k}{16}$ with k = 0, ..., 15 are given by

$$\tilde{r}(\omega_k) = \frac{r(\omega_k) - r_0}{\omega_k} \tag{2.33}$$

By interpolating the values of $\tilde{r}$ it is possible to compute the coefficient of r.

Steps of the algorithm

The steps of the algorithm presented in Gronchi et al. [20] are:

1 Compute the polynomial coefficient appearing in $\hat{S}(t)$ at $t = 0$ and at all the 16^{th} roots of unity ω_k by the DFT algorithm;

2 Compute the determinants of the 17 matrices $\hat{S}(0)$, $\hat{S}(\omega_k)$ (with k = 0, ..., 15), thus obtaining the evaluation of $r(t)$ at $t = 0$ and ω_k;

3 Use eq. 2.33 to compute $\tilde{r}(\omega_k)$;

4 Apply the IDFT algorithm to obtain the coefficients of $\tilde{r}(t)$ from its 16 evaluations;

5 Get the coefficients of $r(t)$ using the relation in eq. 2.31;

6 Computes the real roots of $r(t)$;

7 Starting from the solution $\hat{t} \in (R)$, search for possible $\hat{s} \in (R)$ for which ($\hat{t} \in (R)$, $\hat{s} \in (R)$) is a solution of the system 2.29;

8 Detect the type of singularity.

For the purpose of this thesis work, the last step is focused on finding the minimum that corresponds to the MOID.

2.6.3 Time-Angular window

The last step presented in the method by Hoots et al. [21] is the time filter. The idea is to find all the windows around the MOID points for each orbit and to check possible overlaps between the windows of the first object and the windows of the second object; in case of overlaps, the presence of close encounters is checked in those windows.
Figure 2.14 shows an example of the window generation, where u_r is defined as the sum of three angles: the argument of perigee of the orbit, the true anomaly, and a third angle defined as the angle between the vector aligned to the nodal line and the vector aligned to the direction perpendicular to the orbital plane.

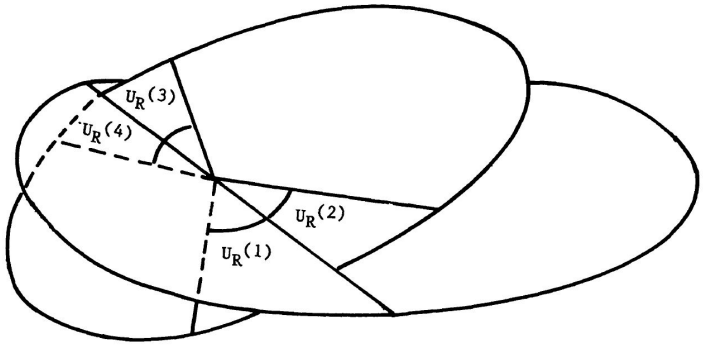

Figure 2.14: Angular windows around MOID points - Image taken from Hoots et al. [21]..

In this picture, taken from the Hoots paper, the MOID is considered along the nodal line; hence, the angular windows are generated around this region. Similarly, the windows are generated on the second orbit and possible time intersection are searched.
The angles corresponding to the window edges are converted in a time measure, that is the moment the bodies pass through those points, and more windows are generated according to the time span selected for the search of the close approach.

2.6.4 Filter example

The following example illustrates how the filter works. A target orbit is selected along with 41 comparison orbits (the NORAD ID number of the objects considered is reported in Appendix D.1). Each comparison orbit passes through the filter and, if it does not fulfill all of the previously mentioned steps, it is eliminated, otherwise it is left for further analysis. The thresholds selected for each filter are:

- 300 km for the apogee/perigee comparison;
- 100 km for the MOID evaluation;
- one day for the time filter (both forward and backward).

Figure 2.15 shows the initial condition with all the comparison orbits in green while the target orbit is in red. Then, one after the other, the three filters introduced previously are applied.

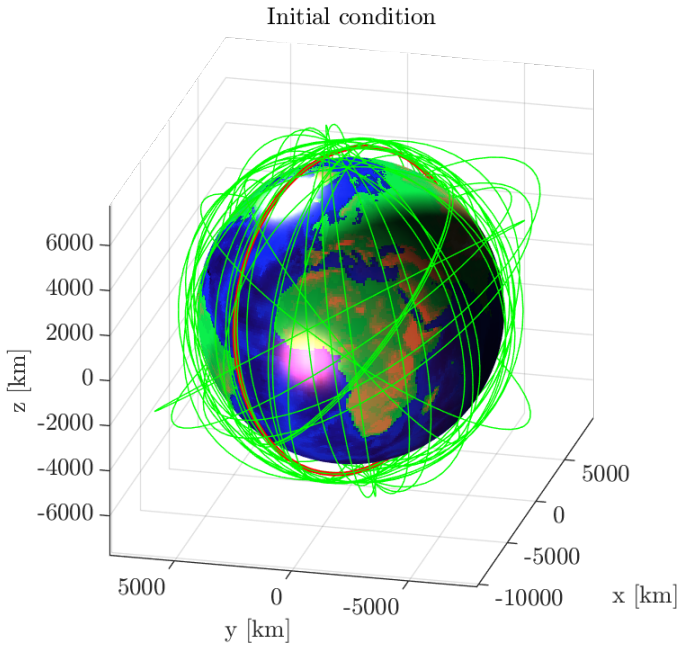

Figure 2.15: Filtering process initial conditions.

After the first filter, the apogee/perigee one, 9 of the initial 41 objects are discarded from the process. Figure 2.16 shows on the top the evaluation of the check distance between each comparison orbit and the target one. As said, 9 values are above the threshold and hence the correspondent objects are eliminated. On the bottom, the figure shows the remaining orbit.

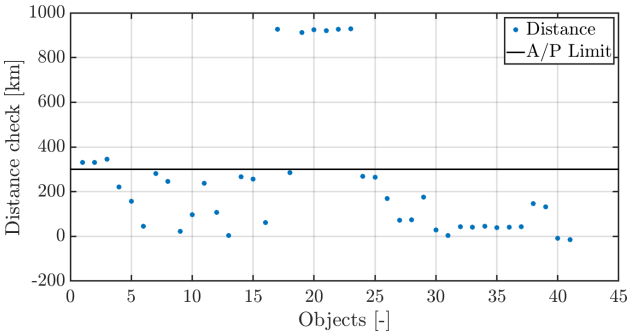

(a) *Apogee/Perigee check distance between each object and the target one*

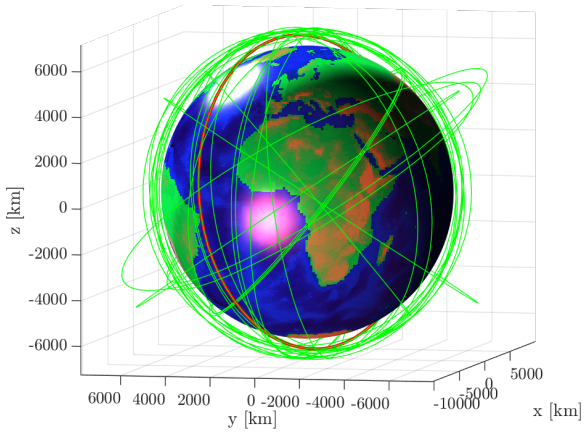

(b) *Objects orbit after first filter*

Figure 2.16: Apogee/Perigee filter

Then, after the application of the second filter, that is the MOID check, other 18 objects are eliminated from the process. Figure 2.17 shows on the top the MOID evaluated for each object, while on the bottom the remaining orbits.
The last filter, the time one, filters out 10 orbits; hence, four orbits remain at the end of the process and are the ones that could be further analysed to check for possible close encounters. Figure 2.18 reports the final conditions.

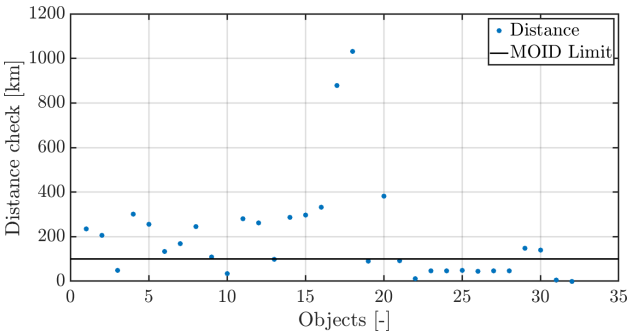

(a) *MOID between each object and the target one*

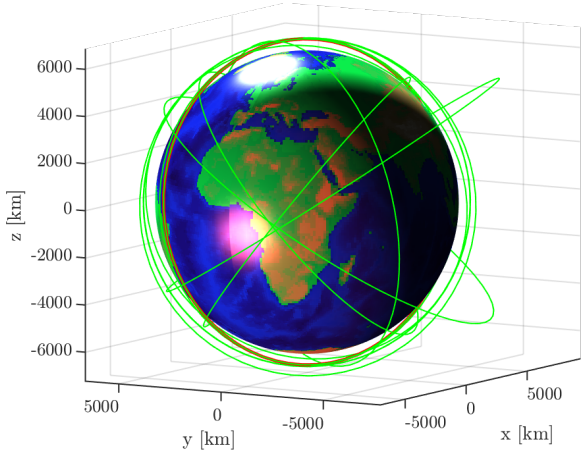

(b) *Objects orbit after second filter*

Figure 2.17: MOID filter

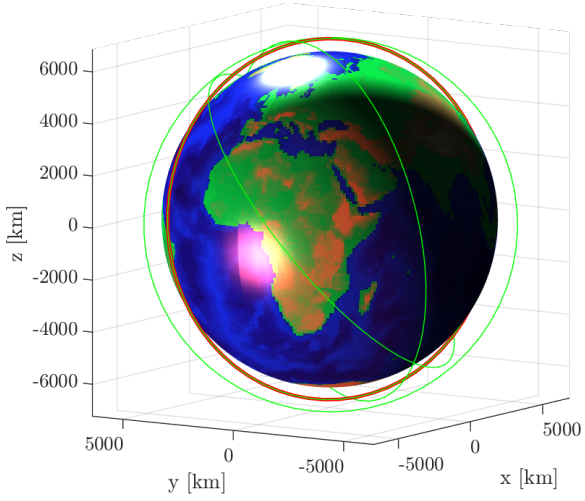

Figure 2.18: Conditions after the third filter.

2.6.5 Triple-loop flowchart

Figure 2.19 shows the steps of the triple-loop filter. As input, the method needs the orbital parameters of the two objects that are compared and the tolerances selected for each step. At the end of the process, the filter fails in case no matching is found between the two bodies, other wise the filter response is positive.

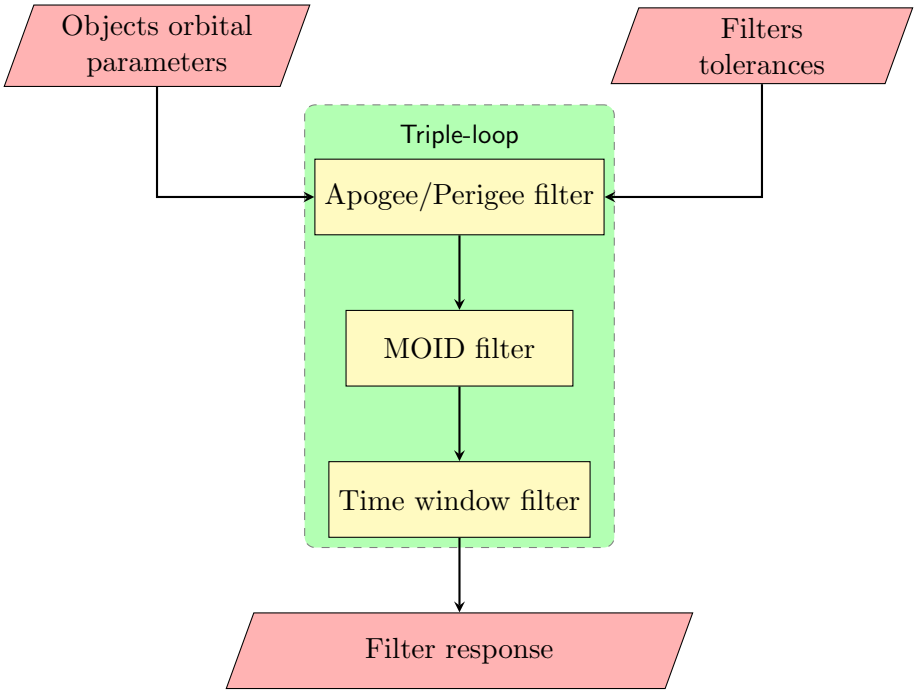

Figure 2.19: Triple-loop filter flowchart.

2.7 Gabbard Diagram

The Gabbard diagram is a type of plot developed by John Gabbard, a NORAD employee, in the 1960-70's to analyse and diagnose satellite breakups [29]. This tool allows to visualise the distribution of the debris with respect to the main body position; indeed, the plot shows the orbital period of the objects (typically expressed in minutes) on the X-axis and the perigee/apogee altitude (typically expressed in km) on the Y-axis. An example is displayed in Figure 2.20, where the distribution of the Iridium 33 breakup is reported; it is interesting to observe the bow tie pattern, which is typical for breakup events.
Different patterns are generated, depending on the orbit of the objects involved and on the location of the breakup along the orbit itself. Indeed, these two parameters influence the energy involved and the type of perturbations that affect the debris soon after the fragmentation.
Through this tool, it is hence possible to further characterise the breakup events and to become aware of the location of the debris in space.

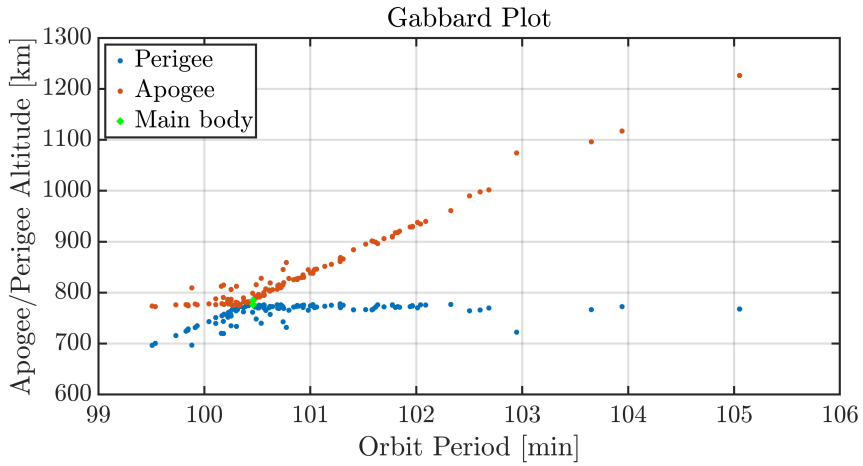

Figure 2.20: Gabbard Plot of Iridium 33 breakup, nine months after the event.

Chapter 3

Event detection

This chapter is dedicated to the description of the model developed to fulfil the first of the two goals explained in the introduction (Section 1.4), that is the identification of possible occurred fragmentations. Indeed, the entire model can be subdivided into two parts, each of which is characterised by different phases:

1 the detection of possible fragmentation events;

2 the identification of the parent object involved in it.

The model for the fulfillment of the second objective is described in the next chapter. The event detection model can be subdivided into three main phases. The first phase is dedicated to the preparation of all the input data selected for the analysis; the latter have to be manipulated and some features have to be evaluated before the starting of the analysis. The second phase is related to the elimination of objects unnecessary for the analysis with the use of different types of filters; this is advantageous also to reduce the computational time required by the process. In the end, through the use of the propagator and post-process analysis, the outputs are acquired. Figure 3.1 summarises the main processes needed for the localisation of the event. The output data are then analysed to identify the parent body as well explained in the next chapter. As visible, two different strategies are adopted depending on the type of input data; indeed, if it is well-known a priori that the TLEs in input refer to a single family, the clustering/pruning phase loses of importance and hence is skipped by the process.

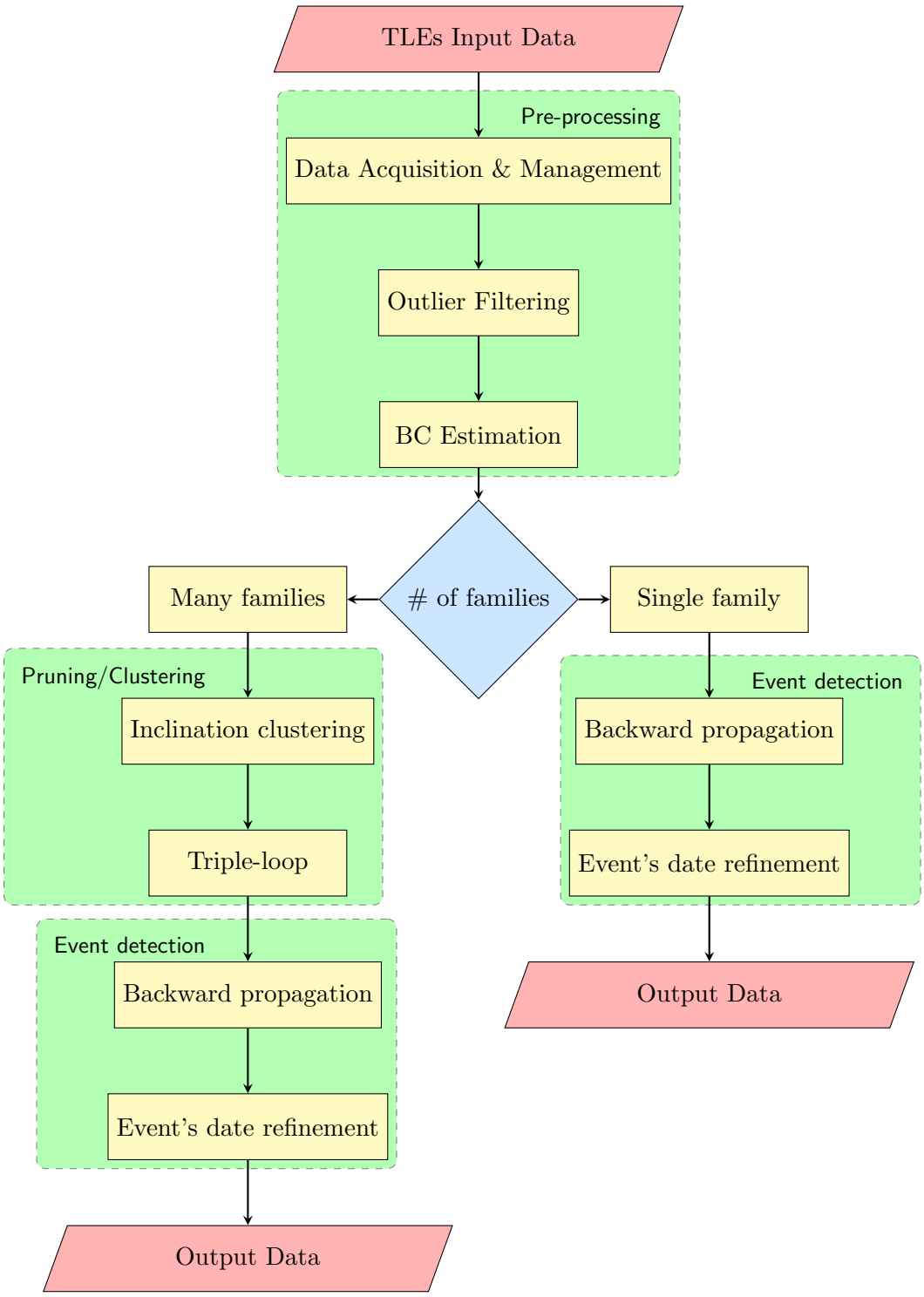

Figure 3.1: Event detection flowchart.

3.1 Data preparation

First of all, TLEs are acquired and prepared in the form useful for the analysis. Since the propagator exploited here 2.2 works with mean elements, the orbital parameters are directly recovered from the TLEs. Moreover, the TLE orbital elements are represented in TEME reference frame that is the same adopted by the propagator; consequently no transformation is needed. As previously stated, the data is acquired in the form of TLEs that may be affected by errors. To avoid the presence of outlier values, before starting with any type of analysis, the data is checked with the use of the filter introduced in Section 2.4. After the filtering phase, the data is ready for the study. Then, it is necessary to set up the data for the following phases. First of all, the BC is estimated for each object from the corresponding B^* value. The time span that the TLEs cover for the BC estimation is of 15 days for each object; this value is selected since, on the one hand it is suitable to recover a proper values for the ballistic coefficient (as showed in Section 2.5) and, on the other hand, does not waste computational time in case many objects have to be considered for the study. The BC is estimated daily among the TLEs considered and a mean value is considered for every following analysis. It is worth to state that the BC is considered as constant for the entire propagation process. Once all the objects have been assigned their BC estimate, the last TLE (i.e. the oldest one) is selected as initial state of each object. From this first initial state, a first propagation is performed to move all the objects at the same initial date, that is chosen taking as reference the oldest among all the TLEs. After this first phase, the analysed elements are ready to be exploited for the study process.

3.2 Pruning/Clustering phase

The second phase is dedicated to the selection of the objects that will be propagated in the third phase to search possible breakup events. Depending on the type of analysis that is performed, this phase may be performed or not. Indeed, if the considered objects belong to the same family, the pruning process may be skipped and the propagation is directly performed. In case the data set is constituted by unknown objects, this phase is essential to eliminate all the objects that are uncorrelated with the ones that are involved in a fragmentation. As an example, if it is necessary to find the origin of an unknown fragment, the propagation of all the known objects would entail a waste of time, along with the possibility of worst results. Consequently, a filtering phase before the propagation is extremely useful. Orbital properties

are considered within this process; indeed, in the LEO region it is possible to take advantage of some peculiar features. One of them is the little influence of perturbations on the orbit inclination change of each objects. Since the evolution of the inclination can be considered as bounded in time and since, following the events, the generated debris will stay close in inclination with respect to the main body, it is possible to cluster around the unknown objects all the known ones that are close to it according to the inclination. In this way, a large part of the objects considered initially are cancelled out from the study. Figure 3.2 shows the distribution of the objects included in a generic TLEs set on the date 23^{th} February 2021 (taken from `www.space-track.org`). The distribution is represented through the use of three Keplerian elements which characterise each object's orbit, that are the inclination, the eccentricity, and the semi-major axis. It is worth to mention that each orbital element is normalised with respect to the correspondent maximum value among all the considered objects. As visible, different regions can be distinguished at different inclination; due to this peculiarity, as previously stated, it is possible to subdivide the space region into subsets related to different values of inclination.

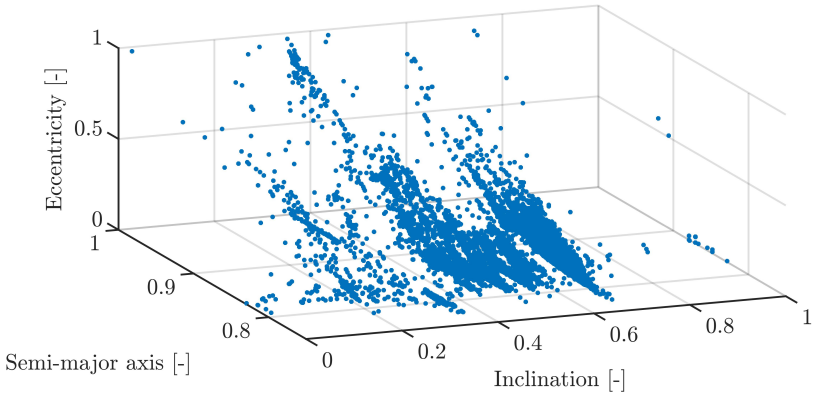

Figure 3.2: Distribution of the objects with respect to the normalised (on the maximum value) inclination, eccentricity, and semi-major axis of each orbit, before the inclination clustering.

Taking into consideration only the objects displayed near the 0.7 value of the inclination, in Figure 3.3 it is observed, as expected, that the bodies are clustered in inclination. More stringent values for the region selection can be considered to cluster objects around the ones selected as unknown. On the contrary, the distributions in semi-major axis and eccentricity seem to be more continuous, and hence are treated in a different way.

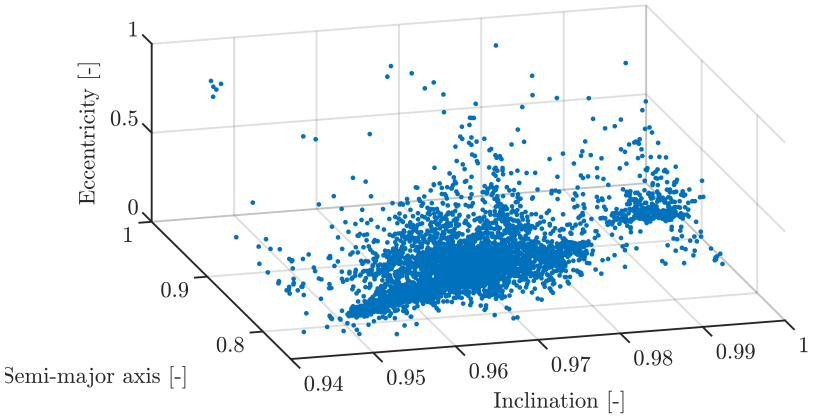

Figure 3.3: Distribution of the objects with respect to the normalised (on the maximum value) inclination, eccentricity, and semi-major axis of each orbit, after the inclination clustering.

It is however important to note that some inclination regions are widely used for different types of missions, hence creating denser regions of objects along with the higher possibility of breakup events. This in part represents a limit for this first pruning method; indeed, in regions denser of objects, many objects which are not desired will be not filtered out. Consequently, a second consideration is related to the orbital geometry of the objects. Indeed, it is possible to observe that some orbits are geometrically incompatible with respect to the analysed one. To further eliminate objects the triple-loop is used, considering only the first two filters. The time pre-filter is not suitable here since, far from the event, it could be fallacious. Through this filter it is possible to select the objects that can have a close encounter or that may have had close encounters in the past. Since the filter works considering two bodies at the same time, here the first body is represented by the target (i.e. the unknown) while the second body is represented by all the objects included in the known set. All the objects that remain after the pruning process are considered compatible with the analysed one. It is worth to mention a first limitation affecting this second method, that is the presence, in some space regions, of satellite constellations or satellite families that could share orbital elements values. This inevitably degrades the analysis since debris created by the fragmentation of a satellite belonging to a constellation may be associated with a wrong satellite or the satellite belonging to the constellation may be clustered around the unknown objects. After this second phase, the objects are ready for the most important stage that is the event detection phase, where possible events are searched.

3.2.1 Example of the pruning phase

A first example is presented here to show the behaviour of the pruning phase. The example is performed considering as unknown object a fragment of the Iridium 33 (Norad ID number 33772), and the same set of objects used in the previous section. The Table 3.1 shows that, as the distance in inclination form the target object decreases, more objects are filtered out from the initial set; on the other hand, if the Δi[1] is too small, many fragments belonging to the Iridium 33 are discarded, too.

Δi deg	Initial	Final	Eliminated	Iridium 33 In	Iridium 33 Out
5	16232	2616	13616	330	330
4	16232	2489	13743	330	330
3	16232	629	15603	330	330
2	16232	602	15630	330	330
1	16232	454	15778	330	330
0.5	16232	448	15784	330	330
0.2	16232	427	15805	330	315
0.05	16232	297	15935	330	197
0.02	16232	191	16041	330	95
0.005	16232	66	16166	330	22

Table 3.1: Number of objects survived after the inclination filter depending on the selected Δi.

Another feature that has to be analysed is the location of the considered unknown objects with respect the other Iridium 33 fragments. As observable in Figure 3.4, that refers to the previous example, the unknown object is located in a region of the inclination distribution that is denser of objects (mainly Iridium 33 debris). In case the unknown fragment was positioned closer to the ends of the Iridium 33 set of debris, a higher number of wrong objects would have been included in the set after the inclination clustering.

A Δi of 0.5 deg is considered to pass to the second filtering stage; hence

[1]It is worth to highlight that the Δi is used to build an interval around the analysed inclination.

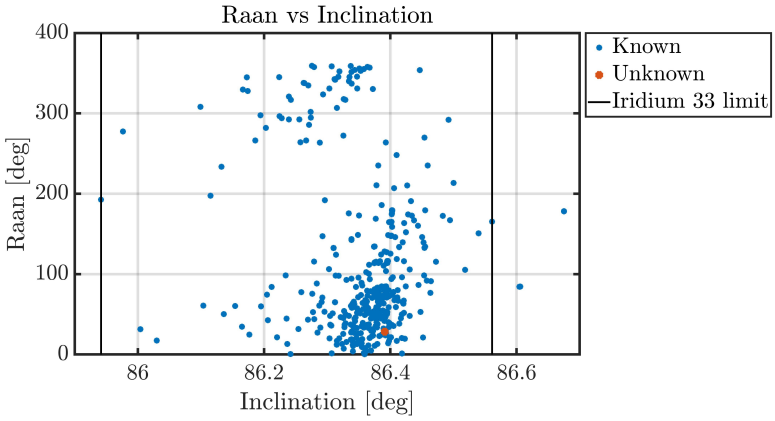

Figure 3.4: Location of the unknown Iridium 33 fragment with respect to the limits in inclination of the Iridium 33 debris.

448 objects (330 of which belonging to the 97051 family) of the initial set have passed the first filtering phase. If this last set of survived objects is passed through the second filter, it is possible to reject other non-desired objects. Considering a threshold of 100 km for the apogee/perigee filter and of 50 km for the MOID, only 40 elements remains at the end of the process, 35 of which belong to the Iridium 33 breakup event. By analysing the 5 foreign objects it is possible to verify that are all related to other Iridium missions (whether they are fragments or satellites). Figure 3.5 displays the location of the unknown objects with respect to the objects included in the set before the second filtering stage.

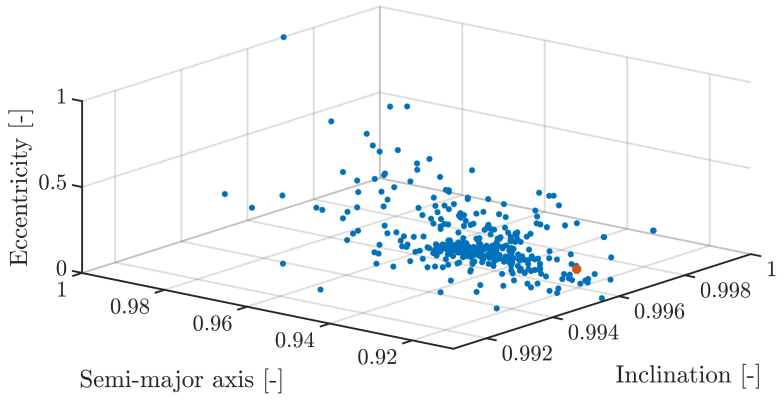

Figure 3.5: Distribution of the objects with respect to the normalised (on the maximum value) inclination, eccentricity and semi-major axis of each orbit, after the inclination clustering (the orange dot is the unknown fragment).

3.2.2 Focus on the triple-loop

Regarding the triple-loop it is worth to make further considerations. As observable from the example, it is evident that it is not always possible to have as output all the objects belonging to the analysed family. This is because the orbital evolution of each fragment is highly dependent on the condition after the breakup and on the perturbations that affect its motion along its entire life. However, this problem is shared by all the pruning methods introduced in section 1.3.1. Indeed, all the methods lack of accuracy for different reasons. The D-criterion (Section 1.3.1) loses of accuracy as the fragments are studied far from the events since the Right Ascension of Ascending Node (RAAN) and the argument of perigee (along with the other Keplerian elements) spread in the interval [0 degrees,360 degrees], making their evaluation in the similarity check erroneous. The hierarchical clustering method (Section 1.3.1) instead tries to compare the semi-major axis and the eccentricity that could be different for the analysed fragments due to the evolution in time of both the Keplerian elements. The power of the triple-loop is in the combination between the semi-major axis and eccentricity to check geometry compatibility between the analysed objects. Indeed, orbits characterised by different values of semi-major axis and eccentricity could have low values of MOID, hence preventing them from being eliminated. It is however evident that also the triple-loop has its weaknesses as the initial time of the study goes far from the event date. The final idea is to try to cluster around the unknown object the majority of the fragments belonging to the same family so that, during the propagation, it is possible to check some common features which will become much similar as the fragments are propagated near the event date.

3.3 Fragmentation event

This phase is dedicated to the research of the event. Since the date of the event is unknown, it is necessary to have a first rough estimation of it. A first guess is computed making the assumption of a linear evolution of the right ascension of the ascending node (Ω) in time; the idea is to exploit a first short propagation (e.g., one day) from which the values of Ω and $\dot{\Omega}$ (that is the derivative in time of the right ascension of the ascending node) can be acquired for each body. Then, assuming a linear variation for the RAAN it is possible to estimate the new values of Ω in time. The equation for each body is

$$\Omega_{new} = \dot{\Omega}\mathbf{t} + \Omega_0 \tag{3.1}$$

where Ω_0 is computed by the propagator and $\mathbf{t}$ is the time.
Then, it is checked where the intersection (in time) between each couple of bodies occur; this is considered as the first rough estimate useful to place the mid point for the analysis. The propagation is then performed daily for a time span that is established by the previously computed rough estimation. The initial time for the study is set at the date considered for the analysis, while the final time is set by adding to the initial time twice as many days as those found with the rough estimation (since the latter is considered as the mid point of the analysis). Figure 3.6 shows an example of the procedure. The example is related to the Iridium 33 breakup and the fragment's TLEs are taken one year after the event. The evaluation of the intersection between each couple of lines returns the first rough estimation useful for the beginning of the search process.

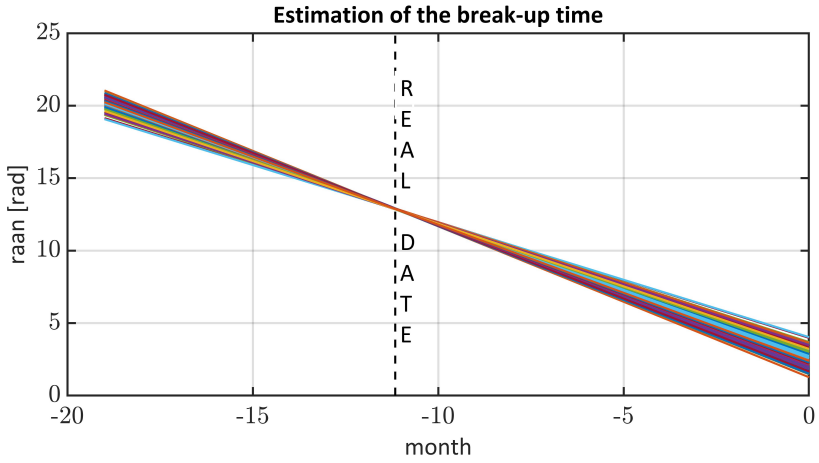

Figure 3.6: First rough estimation of the event epoch.

3.3.1 Single family

In case only a single family (i.e. fragments belonging to the same parent object(s)) is considered for the analysis, the check for a first time estimation is carried out looking for the minimum in the $\Delta\Omega$ (computed as the difference between the maximum and the minimum values of the RAAN of the objects considered). Indeed, the more the elements are propagated closer to the fragmentation event, the more it is expected that the orbits of the objects are characterised by similar values of right ascension of ascending

node. The propagation is performed daily from the initial to the final time selected for the study. Due to the presence of possible inaccuracies in the propagation, as the initial time goes farther away from the event one, this first estimation might be affected by mistakes. Consequently, a further analysis to increase the time accuracy is considered. The refinement method is performed through the use of the triple-loop filter, this time exploiting also the time filter, since the study is performed near the fragmentation epoch. The time filter is used to find out the time window around the MOID points inside of which the two objects compared by the filter are located simultaneously and hence a close approach between them can occur. A simple Newton method is performed inside the selected window to find the close approach distance and its correspondent time. From Hoots at al. [21], the iteration is defined as

$$\mathbf{t}_{n+1} = \mathbf{t}_n - \frac{R_{rel}}{\dot{R}_{rel}} \tag{3.2}$$

where $\mathbf{t}_n$ and $\mathbf{t}_{n+1}$ are the $(n+1)-th$ an $n-th$ iteration of the process while R_{rel} and $\dot{R}_{rel}$ correspond to the rate of change of the relative distance and its derivative in time. This last two terms are evaluated as function of the anomaly along the orbit and can be computed as

$$R = r_f \dot{r}_f + r_s \dot{r}_s - \underline{\dot{r}}_f \cdot \underline{r} - \underline{r}_f \cdot \underline{\dot{r}}_s \tag{3.3}$$

$$\dot{R} = \dot{r}_f^2 + r_f \ddot{r}_f + \dot{r}_s^2 + r_s \ddot{r}_s - \underline{\ddot{r}}_f \cdot \underline{r}_s - 2\underline{\dot{r}}_f \cdot \underline{\dot{r}}_s - \underline{\dot{r}}_f \cdot \underline{\ddot{r}}_s \tag{3.4}$$

A strong assumption is considered here, that is approximating the osculating orbital elements (more suited for this kind of analysis) with mean orbital elements; the assumption is mainly related to the approximation of the osculating mean anomaly with a averaged mean anomaly. Indeed, this thesis work is based on the use of mean elements for the event detection. The possible loss of accuracy in the propagation, along with the strong assumption introduced, entails that the method can be less effective as the propagation time span is longer; this happens because the difference between the correct osculating elements and the orbital elements obtained from the propagator can be extremely different, and hence wrong results can be obtained form the close encounters analysis. However, some tests are performed to see the behaviour of this technique. The parameter which have to be set for the analysis is the time interval for the windows creation within which close encounters are checked. For the test performed in Chapter 5, the limit is set at ± 30 days from the first estimated date. A simple

statistical approach is used to compute the time in which the majority of the objects may have had a close encounter. The time epoch that is evaluated by this last analysis is considered as the final guess for the event date, and the survived elements as the fragments generated by the breakup event.

Single family event detection example

A simple example is proposed here to show how the method works. The initial set of data is composed by Cosmos 2251 debris only, and is taken from a set of objects in a catalog on 24^{th} March 2009. The Cosmos 2251 collision is dated 10^{th} February 2009 at 16:56 UTC. The first guess is evaluated considering a linear variation of the RAAN and from the computations is estimated a value of 2.2573 months; through this value the mid point of the analysis is set. The check in the RAAN leads to a preliminary date events estimation that is 9^{th} February 2009 at 20:07 UTC. To have an idea of the precision of the estimation, a relative error is computed as showed in the following equation

$$\epsilon_{rel}(\%) = \frac{t_{estim} - t_{real}}{t_{last} - t_{real}} \cdot 100 \tag{3.5}$$

where t_{estim} is the time estimated through the process, t_{real} is the real event date while t_{last} is the date corresponding to the beginning of the analysis. The relative error of the first estimate is 1.27 %. Figure 3.7 shows the evolution in the $\Delta\Omega$ variation as the propagation goes on.

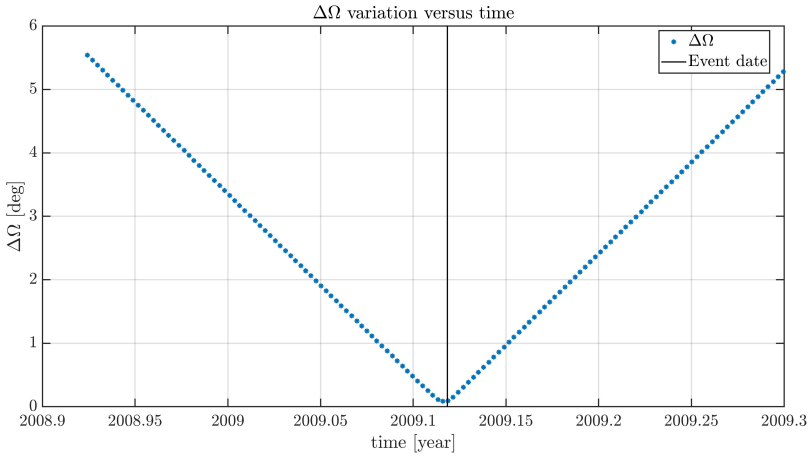

Figure 3.7: Evolution in time of $\Delta\Omega$ - Cosmos 2251 example.

The refinement analysis is performed and a second guess is found. The latter is 10^{th} February 2009 at 14:22 UTC, giving a relative error of 0.16 %.

The results show an improvement in the final solution after the application of the refinement method.

3.3.2 More than one family

The method for this second case is slightly different. After the pruning phase, the same initial estimation considered for the single family is performed since it is assumed that the majority of the survived objects belongs to the correct family. The difference is that a statistical evaluation is included in the propagation process. The idea is the same of the single family case, that is, near the fragmentation, the objects belonging to the same family will be clustered considering the RAAN as study parameter. During the propagation, a 2-dimensional histogram, whose bins are generated by the sine and the cosine of the RAAN of each object, is used to count the number of objects included in each bin. At the end of the propagation process, the time instant at which is located the bin with the maximum number of objects is checked; among all the possible solutions, it is selected the one in which the elements in the bin present the minimum value in the $\Delta\Omega$. Due to the possible presence of foreign objects not filtered out during the pruning phase, all the elements that are not included in the maximum bin are eliminated from the process. Hence, only the elements included in the maximum bin are considered for the refinement phase and for the parent identification phase. The refinement is performed as for the single family case, trying to improve the first estimation.

More families event detection example

The example proposed here is related again to the breakup of Cosmos 2251. The data is taken from the daily catalog on 10^{th} May 2009 (three months after the event), and counts 350 objects (101 of which are Cosmos 2251 debris). One of the Cosmos fragments is selected randomly to be considered as unknown; the selection fell on the fragments 33779 (NORAD ID). Before the propagation, the objects included in the initial set are filtered by the pruning routine. The thresholds selected for the example are: for the inclination a Δi of 0.5 deg, while A/P and MOID filters are selected the values of 25 km and 20 km, respectively. After the filtering phase, a set of 77 objects remains for the study, 74 of which belong to Cosmos. As before, a first rough estimation is computed, giving a value of 3.32 months; consequently the analysis is performed for about 6 months. Figure 3.8 shows the distribution of the objects in RAAN just before the propagation process. Many objects are clustered in a particular region, while three are more iso-

lated. Probably, the latter are the three foreign objects that are not rejected during the filtering phase.

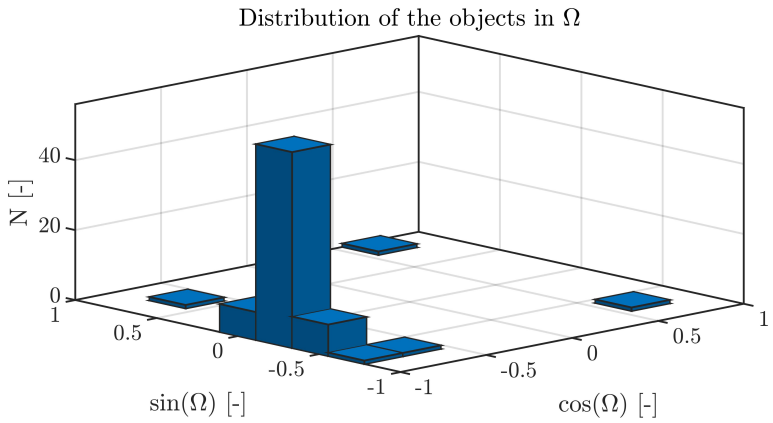

Figure 3.8: Ω distribution - Before the propagation.

The first estimation of the date is computed by propagating back the objects and checking the number of elements inside the bins of the 2-dimensional histogram. Figure 3.9 shows the 2-D histogram at the guess date. The yellow column (75 objects) includes only the Cosmos fragments; hence, the process successfully rejects the remaining three wrong objects.

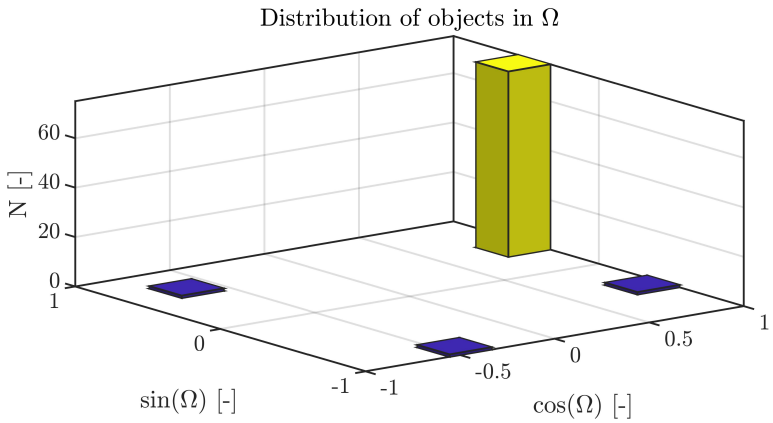

Figure 3.9: Ω distribution - At the event date

Once the propagation is finished, the estimation process returns as guess date 8^{th} February 2009, which corresponds to a relative error of 2.72 %. The refinement technique is preformed exploiting the remaining objects within a time interval of $\pm$ 30 days, giving back a second estimate dated 10^{th} February 2009 at 15:37. The relative error corresponding to this guess is 0.057 %.

3.4 Outcomes

The main outcomes of this process are the estimate of the date and the objects related to the event (in case an unknown fragmentation is considered). The latter is directly correlated to the region of the space where the breakup event may have taken place. The data collected here are then exploited in the second part of the model to recover important features of the event.

Chapter 4

Parent body identification

The second part of the model focuses on the parent body identification. Find the body (or bodies) from which fragments originated is extremely important to further characterise the breakup event. Indeed, many aspects are directly linked to the original objects, among the others the possibility to reconstruct the distribution of all the debris that may be generated from the event. The method proposed here is very similar to the one adopted for the pruning phase explained in the context of the event detection, because the general characteristics useful for this second analysis are the same. The flowchart displayed in Figure 4.1 summarises the steps adopted for the achievement of the final objective. First of all, the distribution of the objects by the inclination point of view is checked, as discussed in Section 4.1. Then, the remaining elements are propagated back to the event date estimated through the first part of the model and two additional filters are exploited to narrow the field of possible candidates (Section 4.2). As for the the model proposed in Chapter 3, tests to determine the validity of the model are presented in Chapter 5.

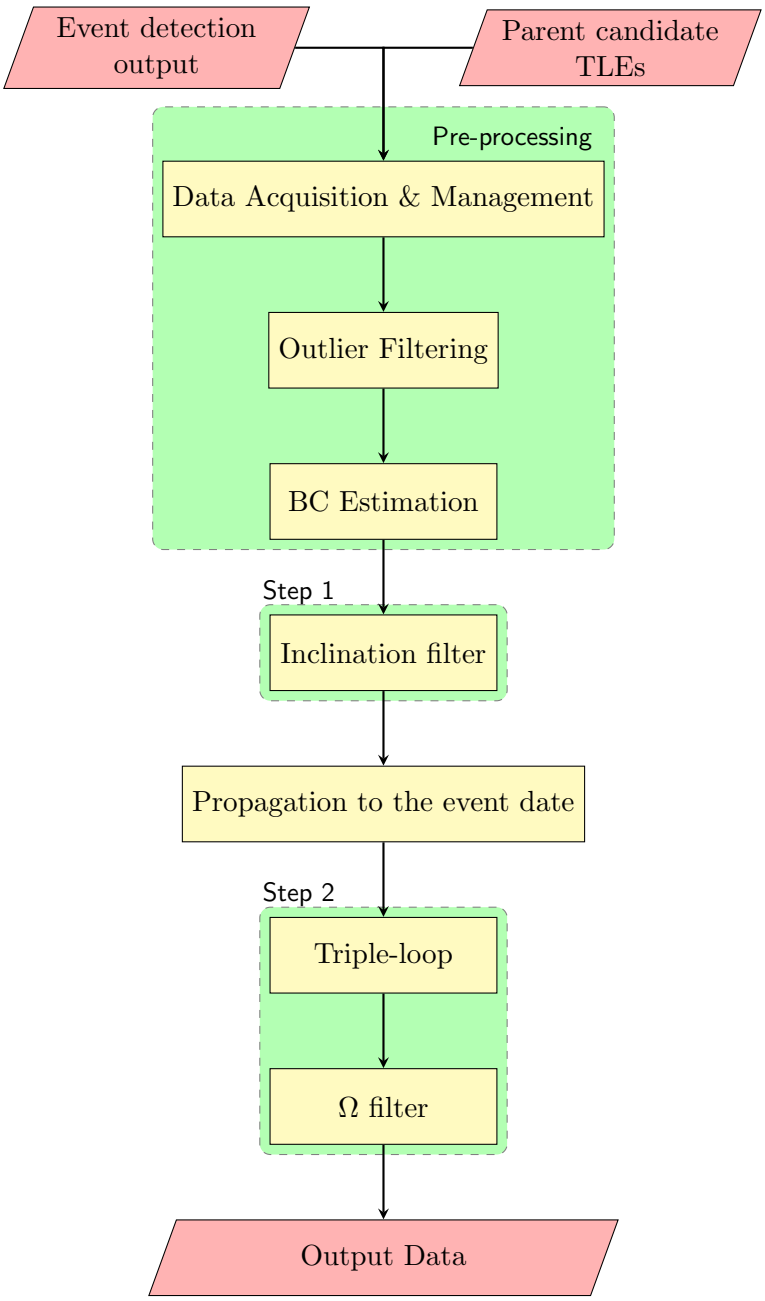

Figure 4.1: Event characterisation flowchart.

4.1 Inclination

The first step for the parent body identification goes through the analysis of the inclination of the objects' orbit. Indeed, as for the pruning phase useful for the event detection, also here it is possible to avoid considering all the objects included in the initial set for the propagation. As largely stated, the inclination is an extremely important parameter that can be exploited also for the parent body identification since its variation in time could be assumed as negligible. Consequently, the first check is performed looking at the orbit inclination of the objects on the starting date of the study. Four examples are proposed here to observe the distribution of the fragments with respect to their original parent body. The set of satellite/upper stages that constitute the initial candidate objects are taken from a catalog dated 25^{th} November 2017, and it is composed by LEO objects only. The fragments displayed in each picture are taken at the same date of the candidate set to have all the objects at the same time. In each image, the blue dots stand for possible satellite/upper stage candidates, the green dot identifies the correct parent object while the orange dots stand for the fragments belonging to the analysed family. The first example is related to the NOAA 16 satellite (NORAD ID 26536) breakup, happened on 25^{th} November 2015. The cause of the breakup is assessed to be a battery explosion (as reported in [5]) and hence the event is considered as an explosion. As clearly visible in figure 4.2, both the fragments and the main body are located in a narrow inclination region and hence a great number of the objects included in the initial sates are completely uncorrelated to the correct one. Due to this, only the objects whose orbital plane has an inclination that is near to the fragment one pass to the second part of the filtering process. As for this case, also by considering older events, the hypothesis remains valid. This is the case of the Cosmos 2251 and Iridium 33 collision, dated 10^{th} February 2009 (16 years before the date of the analysed set). As observable in figure 4.3 and 4.4 (representing the Cosmos 2251 and Iridium cases respectively), the distribution is similar also for not recent events. Indeed, all the objects are clustered in an interval of about 1 deg. A peculiar case that is interesting to be treated is the Fengyun 1C hipervelocity collision, occurred on 11^{th} January 2007. Figure 4.5 shows that the debris generated by the events are more widespread in inclination than in the other cases. Even if the majority of the objects are located in a region of about 1 deg (as displayed in the histogram in figure 4.6), other fragments orbits have an inclination that is far more distant from the main body.

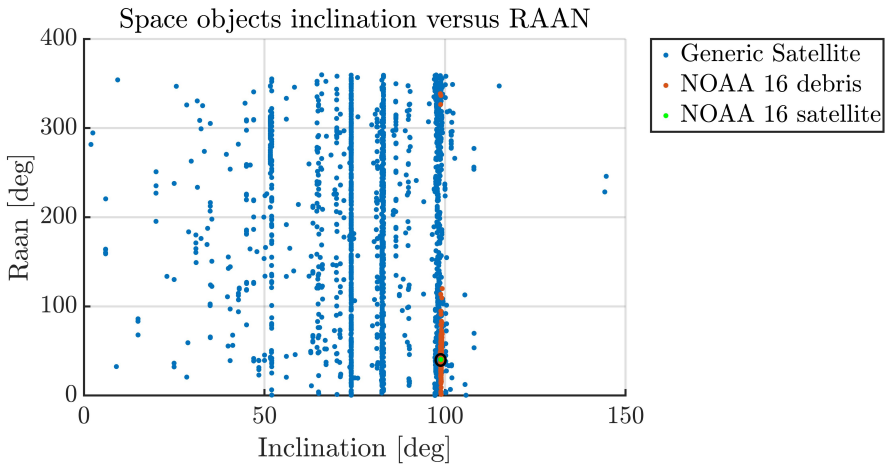

Figure 4.2: Objects distribution in inclination and in right ascension of ascending node of each orbit - NOAA 16 satellite.

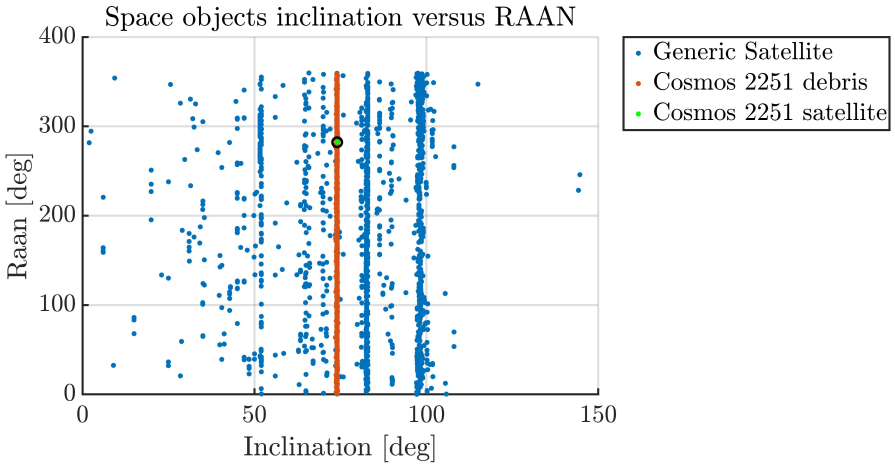

Figure 4.3: Objects distribution in inclination and in right ascension of ascending node of each orbit - Cosmos 2251 satellite.

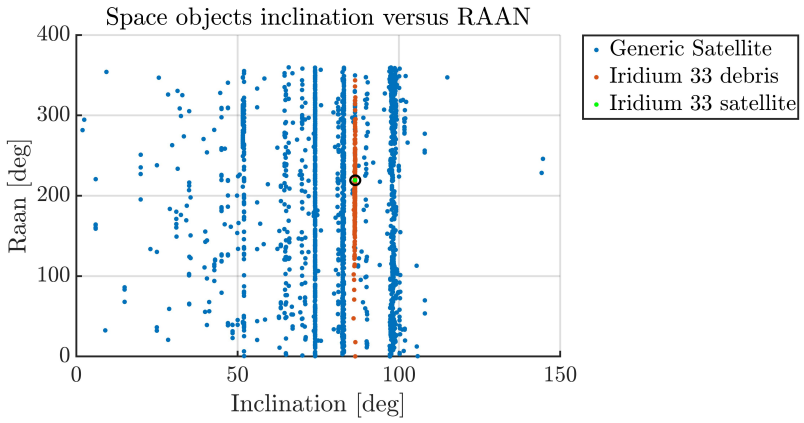

Figure 4.4: Objects distribution in inclination and in right ascension of ascending node of each orbit - Iridium 33 satellite.

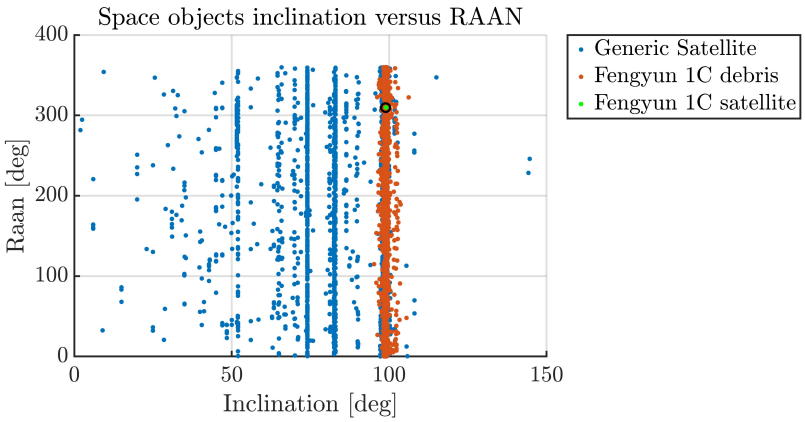

Figure 4.5: Objects distribution in inclination and in right ascension of ascending node of each orbit - Fengyun 1C satellite.

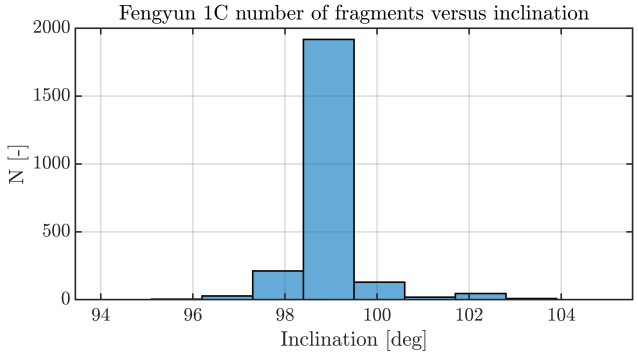

Figure 4.6: Number of fragments per orbit inclination - Fengyun 1C satellite.

The set of fragments is located in the interval of inclination that goes from 95.1 deg to 103.9 deg, making the study more complex. Indeed, in case the fragments analysed in the event detection are characterised by an orbit inclination located in those far region, a higher threshold value is required to not discard the correct parent body; consequently, a higher number of foreign objects would pass through this filtering stage.
The idea for this first filtering phase is simple. First of all, a mean inclination is computed from the objects survived during the event detection. Then, a threshold value is set for the formation of an inclination interval around the previously computed mean value. All the objects that are out of the interval are eliminated from the process, while the remaining ones are considered for further analysis. In this way, the propagation is performed only for a lower (and meaningful) number of objects. Before moving on to the second step, it is important to discuss another peculiar feature that affects this first filter, that is the presence of satellite constellations or of satellite families. An example of the latter case is the previously cited Cosmos 2251. Many other Cosmos satellites have been launched over the years in the same region or in similar regions. This inevitably increases the number of objects orbiting in a particular inclination area, making the use of other filtering steps essential to try to eliminate them; as it will be stated in the next section, the study related to the RAAN is particularly important for this scope.

4.2 Triple-loop and right ascension of ascending node

The second part of the process, as stated, is performed after that all the objects are propagated back to the event date. Indeed, mainly for the last step, it is essential to study the candidate objects near the fragmentation date. The two steps that characterise this second part of the model are:

- A geometrical selection based on the triple-loop filter (considering only the first two filters);
- A sort of clustering based on the RAAN of the fragments' orbits survived from the event detection.

Concerning the triple-loop filter, the time filter is discarded here since the objective is to discriminate parent candidates looking at the geometry of their orbit, and not to identify the close approaches between them. As the fragments are propagated back near the fragmentation event, it is expected that all the objects originated from the same parent will stay close

in distance. Consequently, the orbit geometry is useful to filter candidate objects that are not compatible with the remaining fragments. As per definition, the triple-loop compares two objects at the same time. During this phase, the first object is represented by a fragment while the second object is represented by one of the candidates. Each candidate is compared with all the fragments and two possibilities are considered:

1 the candidate is eliminated in case the filter fails for each fragments;

2 the candidate pass this filtering stage if the filter returns a positive result for at least one of the fragments.

This solution is adopted because, knowing the possible inaccuracy in the propagation and remembering that mean elements are being considered, it is possible that the correct body is eliminated erroneously in case too stringent thresholds are selected for the apogee/perigee and MOID checks. A simple example is proposed here to better visualize the model's idea. Figure 4.7 shows the Gabbard plot of 45 fragments (whose perigee altitudes are represented by the yellow dots, while the apogee altitudes are represented by the purple dots) belonging to the Cosmos 2251 (identified through the event detection routine) together with the Gabbard plot of 405 possible candidates (whose perigee altitudes are represented by the blue dots, while the apogee altitudes are represented by the orange dots) taken from a satellite catalog at the same date of the fragments one. The latter have been previously skimmed through the inclination filter and have been propagated back to the fragmentation event date.

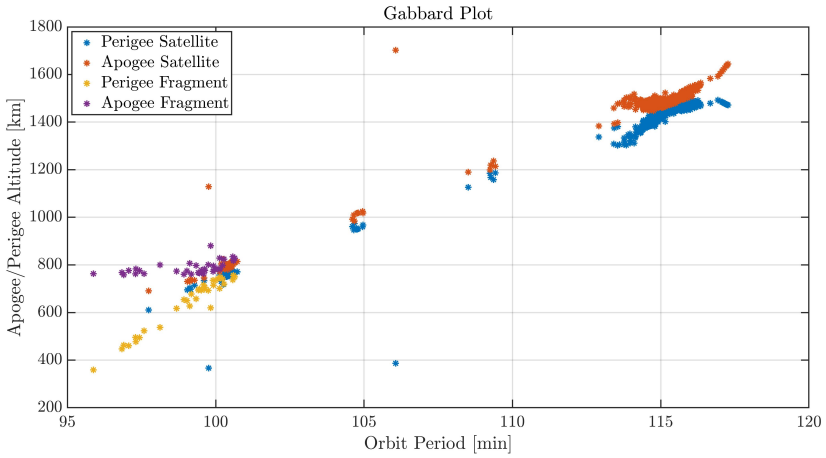

Figure 4.7: Gabbard plot of fragments and parent candidates.

As clearly visible from the picture, the fragments are all located in a specific altitude region, while the parent candidates are widespread at different altitudes. The objective of the triple-loop is to eliminate all the candidates that are far from the fragment altitude locations. To better quantify the contribution of this filter, the MOID between each fragment and the Cosmos 2251 orbits is computed. Figure 4.8 shows that the MOID's values, as expected, are of the order of some kilometers, in most cases below 4 km. A couple of fragments presents a MOID that is much higher than the others. This is the reason why, as previously observed, a candidate is discarded only if the comparison fails with all the fragments. In the proposed case, using a threshold of 5 km for the maxi admissible MOID would bring to the exclusion of the correct parent body. With the approach proposed here, the use of a more stringent limit does not lead to its elimination. However, this causes also an undesired effect, that is the inclusion of objects that would be eliminated in the final set and that instead manage to survive to the process. The use of a last filtering stage is essential to further reduce the final number of objects included in the set. Considering a threshold value of 10 km for the MOID check, 362 candidate are eliminated and only 45 objects remain for the last step. Obviously, the use of different threshold values entail a different number of candidates that survive through this step and have to be considered for the last one.

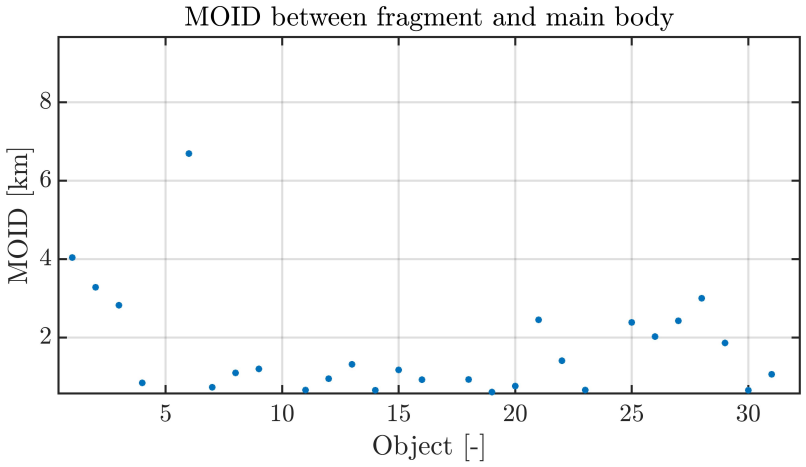

Figure 4.8: MOID between fragments and Cosmos 2251.

The last step of the method is based on the study of the RAAN of the remaining candidate objects. Indeed, near the event date, the fragments and the parent body are expected to be bounded in RAAN. Contrary to what is done for the inclination, a mean values among the fragments is

not computed here. Indeed, by studying the propagator accuracy and the selection of different sets of fragments for the same event detection case, it has been observed that in some cases the minimum $\Delta\Omega$ found by the process could be also near the event date. Consequently, the methodology adopted for this last filter is the following:

1 compute the $\Delta\Omega$ between each parent candidate and all the fragments;

2 take the minimum value out of all those obtained;

3 discard the candidate that overcome a selected threshold.

All the candidates that are not eliminated by the process are considered as probable parent object. This last step is extremely useful in cases (like the Cosmos 2251) in which satellite constellations or satellite families are involved. Figure 4.9 shows the RAAN distribution of each fragment (blue dots) and of the parent candidate (orange dots). It can be easily observed that all the fragments seem to be aligned at a specific RAAN value.

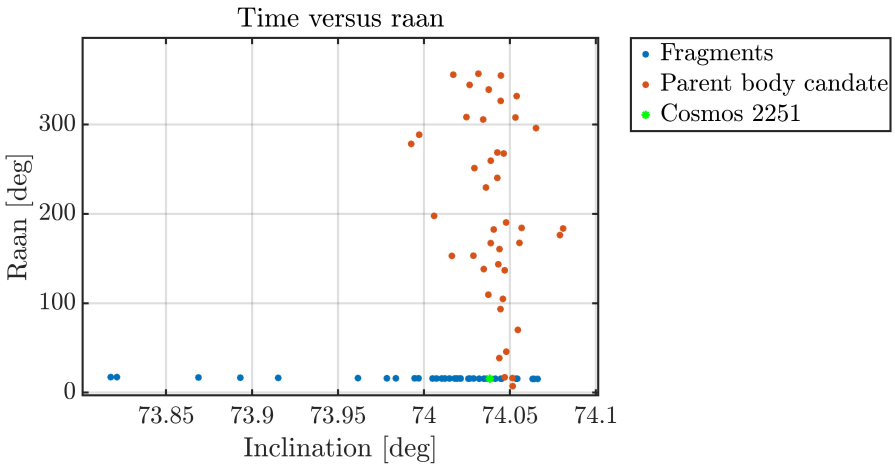

Figure 4.9: Fragments and parent candidates distribution in inclination and in right ascension of ascending node of each orbit.

Among all the candidates, the nearest to the fragments is the correct parent (marked in black) that is much closer than the others. All the other candidates (the almost totality of which belongs to the Cosmos family) are spread at different angles and this is why, as previously highlighted, this last filtering step is extremely powerful and useful for the entire process. For the proposed example, by selecting a value of 0.25 deg as threshold for the RAAN filter, it is possible to identify the correct parent body, that is the

Cosmos 2251. Clearly, this seems to be a quite stringent threshold value, also considering the accuracy obtainable through the propagator adopted for the work. However, as will be shown better in the next chapter, testing the use of stringent threshold values is useful to check the sensitivity of the proposed model.

4.3 Discussion

The outcome of the second part of the model is the possible identification of the fragmented satellite from which the analysed debris originated. At this point of the work (and it will be better clarified in the next chapter) it is not always possible to perfectly identify the correct parent body, but rather it is possible to reduce the number of possible candidates to a smaller subset. Some improvements to this part of the method are proposed in the future work Section 6.2 along with some correlated analysis that can be performed starting from the parent identification. The thresholds for the triple-loop filter and for the RAAN window rule the efficacy of the method. Too wide threshold values would include many objects in the final set, while too stringent values could eliminate the correct parent body. Tests to observe the response of the method with different threshold values are performed in the next chapter.

Chapter 5

Fragmentation scenarios

Previous chapters introduced the theoretical tools and the developed model useful for the characterisation of fragmentation events. This chapter is instead devoted to the tests of the method with the use of different fragmentations. The tests are subdivided between single family and multiple families cases and, inside each case, both the event detection and the parent identification are analysed. All the examinations are performed considering in the propagation process the following characteristics [1]:

- Sinusoidal representation for the solar cycle recovery;

- Drag perturbation;

- Gravitational perturbation: up to J_4 for the zonal harmonics and up to $J_{2,2}$ for the tesseral ones.

For the event detection phase, the accuracy of the method is evaluated through the use of the relative error

$$\epsilon_{rel}(\%) = \frac{t_{estim} - t_{real}}{t_{last} - t_{real}} \cdot 100 \tag{5.1}$$

where t_{estim} is the time estimated by the process, t_{real} is the real event date while t_{last} is the date corresponding to the beginning of the analysis. The relative error is a powerful tool since it links the error in the estimation to the time length of the analysis. Instead, for the parent identification it is evaluated the capabilities of identify the correct body or, in case it is not possible, to observe how many candidates remain at the end of the analysis.

5.1 Test considering a single family

Here are performed tests considering, for the analysis, set of objects constituted by objects belonging to the same family. The sets are composed by:

- Set 1 Cosmos 2251: 51 fragments;

- Set 1 NOAA 16: 61 fragments.

The TLEs of each set are reported in D.2. This first test has a dual objective: checking the validity of the model as the initial date of the analysis goes far from the event one, and monitoring its response considering breakups occurred in different moments of the solar cycle. Indeed, the Cosmos 2251 breakup is dated 10 February 2009 at 16:56 GMT, while the NOAA 16 is dated 25 November 2015 at 9:50 GMT. The latter is localised during a period of higher solar activity than the Cosmos 2251 one.

5.1.1 Event detection

The initial dates are set at 1, 6, 12, 18, 24, 30 months from each breakup event, respectively. As described in Section 3.3.1, whenever a single family is considered for the investigation, the event is detected by finding the minimum $\Delta\Omega$ throughout the propagation. The first examined parameter is just the final $\Delta\Omega$, evaluated at the time instant in which the event is identified. Figure 5.1 shows the $\Delta\Omega$ variation as function of the initial time. As observable, for the NOAA 16 set the variation in the final $\Delta\Omega$ is higher than the one of the Cosmos 2251 set. This increment in the final $\Delta\Omega$ can be a signal of loss of accuracy in the propagation, and hence in the research. Figure 5.2 shows instead the evolution of the relative error as function of the initial time. Also here, the Cosmos 2251 case produces more accurate results. The results seem to confirm what was expected. Indeed, due to the approximation introduced in the propagation model, it was foreseeable that an higher error would be associated to the breakup located during a period of high solar activity. However, the maximum error obtained corresponds to about 1 month.

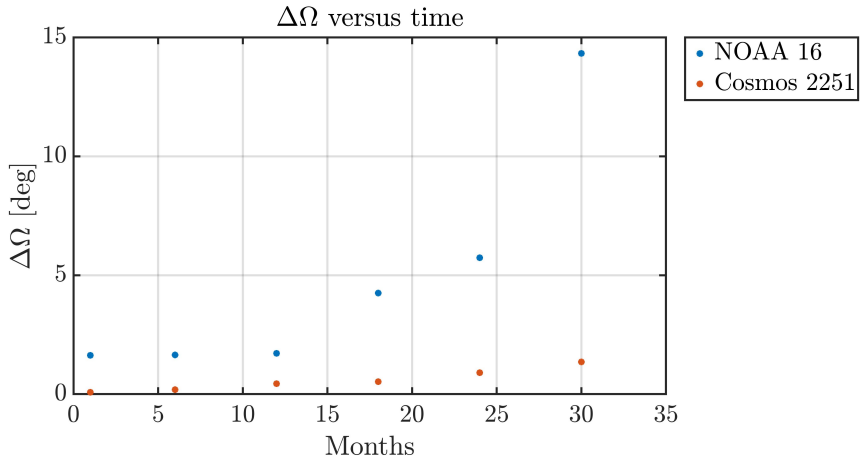

Figure 5.1: $\Delta\Omega$ as function of initial date of the analysis - Test case set 1.

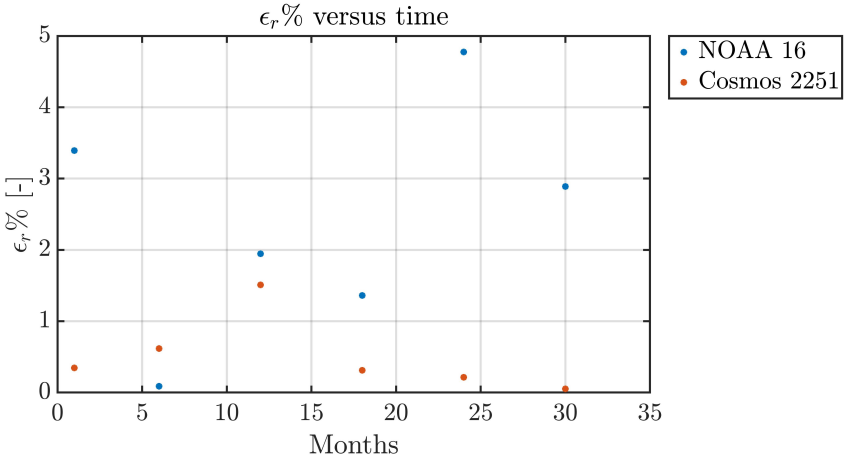

Figure 5.2: $\epsilon_r\%$ as function of initial date of the analysis - Test case set 1.

In addition to the previous consideration, two other sources of error can be identified:

1 The number of objects considered for the analysis;

2 The composition of the set.

Regarding the first source, the set for the NOAA 16 has been created considering all the objects available after one month from the event. The number of objects presented in the set can affect the results because, if an higher number of elements is considered, it is more likely to have fewer poorly estimated objects. Instead, as composition of the set it is intended

which fragments of all those generated by the breakup are considered in the detection process. Indeed, different fragments can be characterised by a different accuracy in the BC estimation and hence in the propagation process. Due to the previous considerations, two more tests are performed (one per each breakup event) with a different initial set of objects. The number of objects for each set is the same as the previous example, but the objects contained are different, and the same propagation dates are exploited. The results are showed in Figure 5.3 and Figure 5.4.

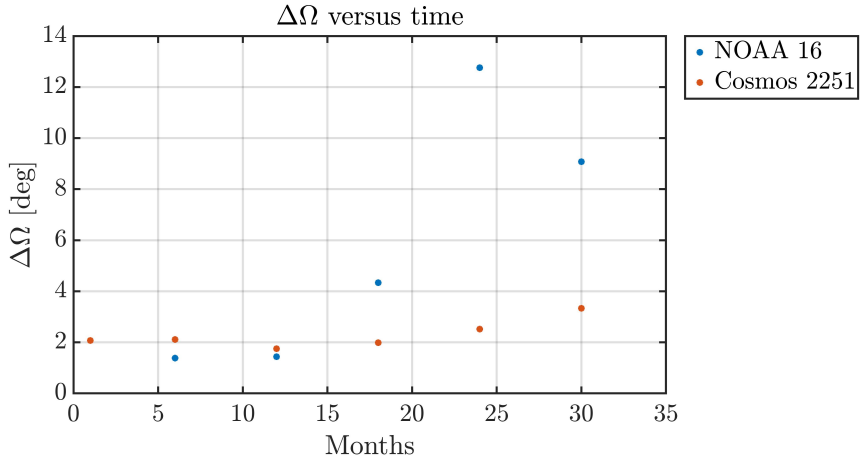

Figure 5.3: $\Delta\Omega$ as function of initial date of the analysis - Test case set 2.

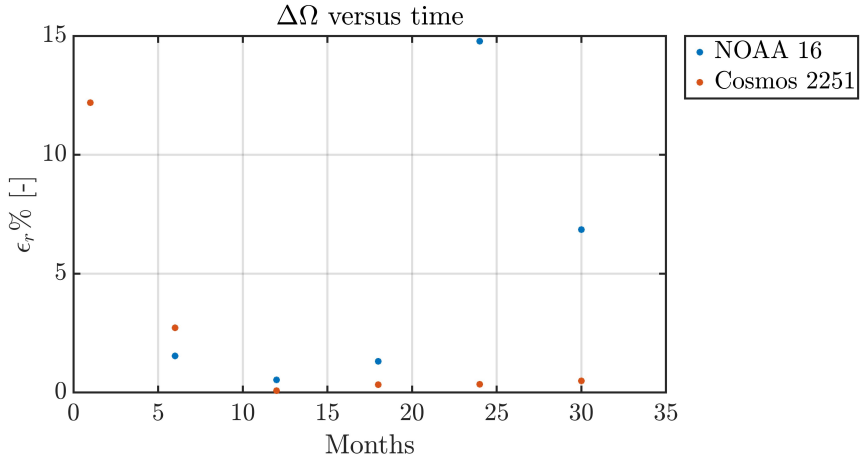

Figure 5.4: $\epsilon_r\%$ as function of initial date of the analysis - Test case set 2..

The second test case exhibits again a better behaviour for the Cosmos set as the propagation is performed for a higher time span. Moreover, the maximum error is associated to the NOAA 16, when the initial date is set 24 months after the breakup. This result is shared by both the test cases which involves the NOAA, and probably is related to a worse accuracy in the propagation due to a worse estimation of the BC. A strange result is observed in the test of Cosmos at one month form the event. The error is high if compared with the same results obtained with the first set. Anyway, the accuracy with longer propagation is clearly better. As for the first test, the $\Delta\Omega$ tends to increase with time. This confirm the fact that, probably, the increment in the relative errors is related to the increment in the final $\Delta\Omega$. In addition, the latter is surely related to a worsening in the propagation.

5.1.2 Refinement

The event detection routine includes a further analysis for the date estimation. The scope is to increase the accuracy of the first estimation trying to identify the time at which the fragments present the close approach. Here are showed the results related to the first two sets considered. The scan is performed considering a time window of ± 30 days around the first estimated date. Figure 5.5 compares the relative errors of the first and of the second estimation for the Cosmos case, while Figure 5.6 displays the results for the NOAA case.

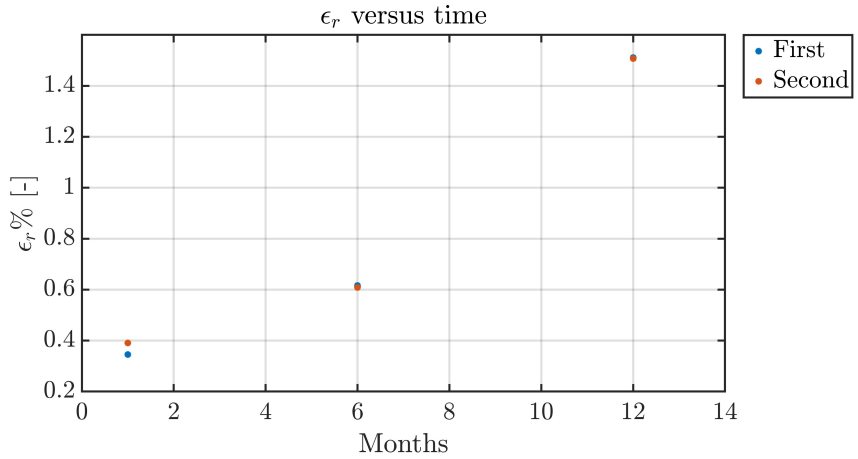

Figure 5.5: Refined $\epsilon_r(\%)$ as function of initial date of the analysis - Cosmos 2251 test case.

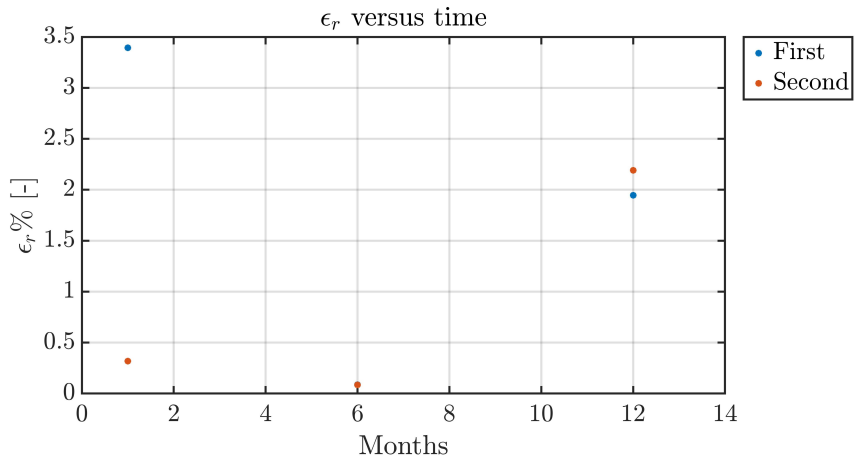

Figure 5.6: Refined $\epsilon_r(\%)$ as function of initial date of the analysis - NOAA 16 test case.

Looking at the Cosmos case, the refined solution remains around the initial one and hence does not improve the initial estimation. While, for the NOAA case, the estimation preformed at one month is better after the refinement with respect to the initial solution. It is however important to observe that, as the initial time of propagation goes far from the event date, the method seems to introduce also possible statistical errors. Indeed, as observable from Figure 5.7 and Figure 5.8 (related to the Cosmos case), the bins around the maximum one tend to increase the number of elements and hence it is possible that the correction date may not be perfectly identified. This result is probably related, on the one hand to the loss of correspondence between the averaged mean anomaly and the osculating one as the propagation is performed for long time spans, while on the other hand to the increment of inaccuracy in some Keplerian elements after the propagation process. Indeed, looking at Figure 5.1, as the initial date is set far from the event, even the RAAN tends to suffer of the approximation introduced for the propagation. This inevitably complicates the evaluation of the MOID and of the windows around it used for the close approach method.

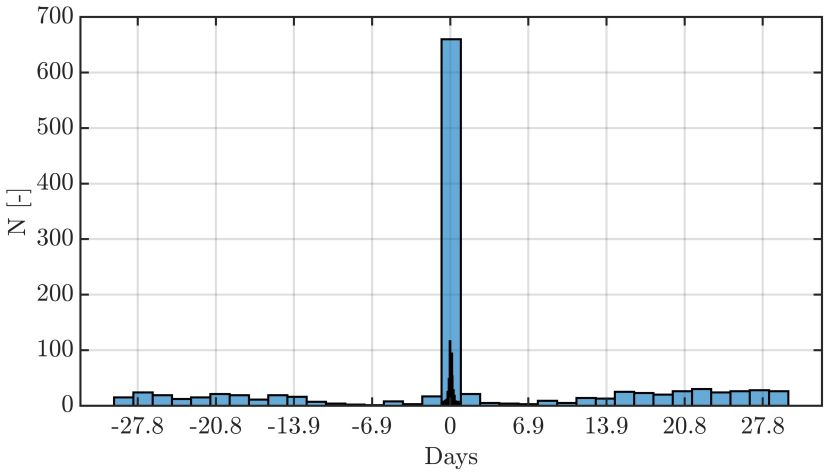

Figure 5.7: Number of identified close approaches per correction time - Test case 1 month.

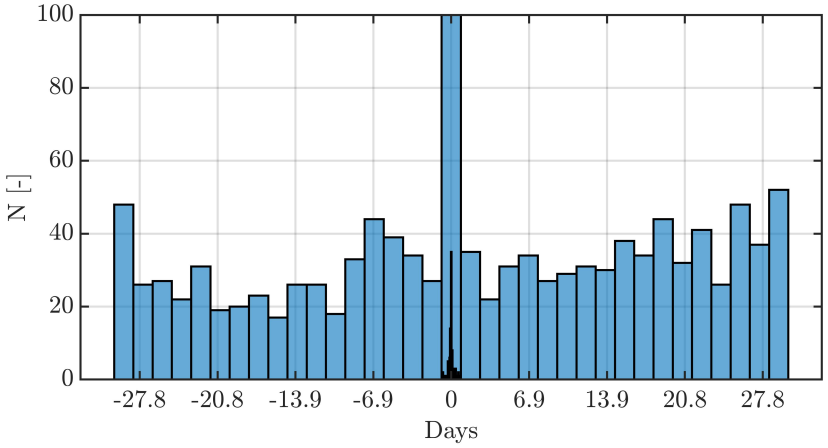

Figure 5.8: Number of identified close approaches per correction time - Test case 12 months.

5.1.3 Parent identification

The second part of the test is dedicated to the identification of the parent object. The examinations are performed considering the first set for each previously introduced fragmentation, while the initial set of possible candidates is composed by all the satellites or upper stages available at the starting date of the process. The check is performed considering a set of variable thresholds to observe the response of the method. The objective is to try to find the thresholds that allow to clearly identify the correct parent objects. However, as stated in Chapter 4, up to now it is acceptable to identify more than one possible parent, trying to eliminate the majority of the initial objects considered. The set of thresholds exploited for the tests are:

- Inclination Δi: from 0.05 deg up to 5 deg with step 0.05 deg;
- Apogee/perigee and MOID filters: [5/1. 10/5, 20/10, 40/20, 60/30, 80/40, 100/50] [1] km;
- RAAN $\Delta\Omega$: from 0.05 deg up to 5 deg with step 0.05 deg.

NOAA 16 parent identification

Figure 5.9 shows the trend in the number of objects remaining after the inclination clustering. Clearly, as the threshold is more stringent, a lower number of objects pass this first selection. The parent is always included in the final set for the 1, 6, 12 months cases for all the thresholds. The method seems to fail when the start of the analysis is farther away from the event and the limit is selected as 0.05 deg. The latter is clearly a too stringent value that does not account for possible inaccuracy of the propagation and in the definition of the parameters.

For the study of the second part of the method it is selected only one of the previously analysed cases, that is the one characterised by Δi equal to 0.5 deg. The remaining objects are propagated back to the date identified in the event detection phase before performing the second part of the filtering. The plot of the combined thresholds (as done for the inclination case) would be too confusing since, per each set, seven subcases are generated from the joint analysis of the two final step. Hence, the results are summarised in the Table 5.1. First of all, it is checked if the method is capable of identifying the correct parent as the single final candidate and the minimum thresholds required to reach this results are reported. In case it is not

[1] (the first term refers to the Apogee/perigee while the second to the MOID)

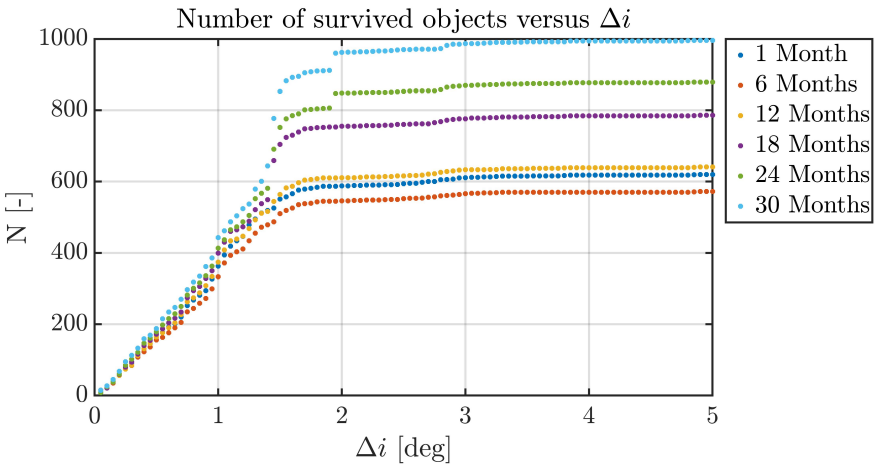

Figure 5.9: Number of survived candidates as a function of inclination threshold Δi - NOAA 16 test case.

possible to properly identify the correct parent, it is important to pinpoint the better solution, that is the one characterised by the lower number of possible candidates remaining in the final set.

	1	**6**	**12**	**18**	**24**	**30**
# Initial candidates	2104	1888	2090	2242	2360	2689
Single Candidate	Yes	Yes	No	No	No	No
A/P - MOID (km)	5-1	5-1	-	-	-	-
$\Delta\Omega$ (deg)	1	0.1	-	-	-	-
# Candidates	-	-	2	3	2	5
A/P - MOID (km)	-	-	5-1	5-1	5-1	5-1
$\Delta\Omega$ (deg)	-	-	0.65	1.45	2.5	3.85

Table 5.1: Parent identification, second step results - NOAA 16 test case.

The method works properly for the first two cases (1 and 6 months), while it is not possible to identify the correct candidate when the initial date is set too far from the event. Looking at the results, downstream of the triple-loop the right body is always included in the set. Hence, the problem has to be found in the last filtering step. Probably, the problem is the same

identified during the event detection study, that is a loss of accuracy in the Ω evolution. This limits the possibility to find the correct body since the error tends to include an higher number of undesired objects in the final set. However, from the large number of candidate objects included in the initial set, almost the totality of them are rejected correctly by the process.

Cosmos 2251 parent identification

The same investigation is performed considering the parent identification of the Cosmos 2251 fragments. The first evident difference with the previous case, as appreciable from Figure 5.10, is in the number of objects surviving after the first filtering step. This difference is mostly related to the already mentioned peculiarity of the Cosmos case, that is the presence of other Cosmos satellites in the analysed region; this inevitably increases the number of objects not rejected by the method. However, for all the cases, the correct parent is included in the intermediate set.
As before, for the second part of the test the set of survived objects when the threshold for the inclination is set at 0.5 deg is selected.

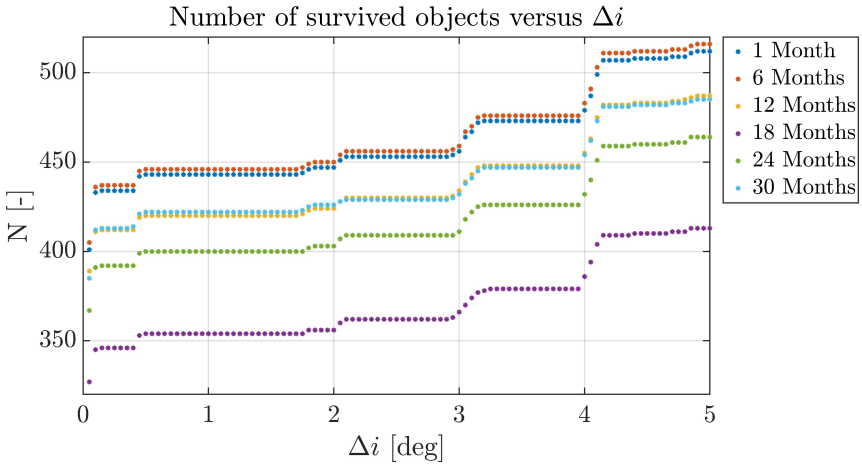

Figure 5.10: Number of survived candidates as a function of inclination threshold Δi - Cosmos 2251 test case.

To perform the second stage of the filtering, the objects are propagated to the event date. Table 5.2 contains the results of the triple-loop and of the RAAN filtering. The outcomes of this second example show that the correct parent is always identified. It is important to note that the results reported in the table are the the minimum ones to identify the better achievable results of the method. Indeed, it is possible to have the same outcomes

considering less stringent thresholds. However, the latter is dependent on the moment of the analysis.

	1	**6**	**12**	**18**	**24**	**30**
# Initial candidates	1719	1777	1673	1486	1678	1703
Single Candidate	Yes	Yes	Yes	Yes	Yes	Yes
A/P - MOID (km)	5-1	5-1	5-1	5-1	5-1	5-1
$\Delta\Omega$ (deg)	0.05	0.05	0.4	0.1	0.15	0.15
# Multiple Candidates	-	-	-	-	-	-
A/P - MOID (km)	-	-	-	-	-	-
$\Delta\Omega$ (deg)	-	-	-	-	-	-

Table 5.2: Parent identification, second step results - Cosmos 2251 test case.

A last comment is necessary for this second case. As previously mentioned, at the beginning of the second stage of filtering many objects where identified as possible parent. From the final results it is possible to observe the power of the RAAN parameter in the filtering selection. Indeed, even though many other satellites belonging to the Cosmos family were included after the inclination filtering, the last analysis is capable of distinguishing the ones more related to the fragments under examination.

5.2 Test considering more than one family

Here are discussed some tests performed considering sets composed by objects belonging to different families. The sets are assembled considering a base composed by fragments belonging to a chosen family and by adding other objects casually from a generic catalog. One of the fragments of the chosen family is considered as unknown and the capability of the model to detect the event and the correspondent parent body is checked. The steps executed are those presented in Section 3.3.2. As for the single family case, the first part of each test is dedicated to the identification of the event date, while the second part is dedicated to the parent object detection. Moreover, the hypothesis regarding the propagation are still valid. Different initial families along with different time spans are considered.

5.2.1 Iridium 33 Breakup

The first series of tests involves the Iridium 33 (NORAD ID 24946) breakup event, dated 11 February 2009 at 16:56 GMT. Three examinations are performed considering the same initial set of objects, composed by 360 objects (of which 79 are Iridium 33 fragments). The initial date for the tests is set on 11 May 2009, that is three months after the event. Each test case is performed both for the event detection and for the parent identification.
The unknown selected for the analysis is different per each case and for the following cases are: the fragment 34594, the fragment 34522 and the fragment 34494 (NORAD ID).

Event detection

The first part is dedicated to check the event detection method. The thresholds for the filtering phase are reported in Table 5.3.

Δi **(deg)**	**A/P (km)**	**MOID (km)**
0.5	25	20

Table 5.3: Filter thresholds - Iridium 33 test case.

The Table 5.4 summarise the number of objects included in the set after the pruning step. In all the cases, the method successfully eliminates all the foreign objects and includes only Iridium 33 fragments. However, depending on the selected unknown objects, a different number of objects remains in the set.

	34594	**34522**	**34494**
# Total Objects	31	22	11
# Iridium 33 Fragments	31	22	11

Table 5.4: Objects included in the set after the pruning phase - Iridium 33 test case.

The results for each case are plotted in Figure 5.11, where the relative errors of the first estimation and of the refined one are compared, and in

Figure 5.12, where the $\Delta\Omega$ computed at the first estimated date are displayed. Looking at the relative errors obtained with the first estimation, the highest value is associated to the third case, characterised by a relative error of about 18.8%. The reason could be related to the low number of objects available for the detection of the event, that could bring to a shift in the final minimum cluster in Ω. Instead, paying attention to the refined estimation, the maximum error is associated to the second test case in which the refined estimate is also worse than the initial one, showing a failure of the technique. For the other two test cases, the refined estimate is better than the first one. The reason of this can be related to the higher $\Delta\Omega$ (computed at the event date) that is associated to the second case. Indeed, since the objects are more spread along the Ω, it is possible that the MOID, and consequently the time windows generated around it, does not allow to properly perform the analysis.

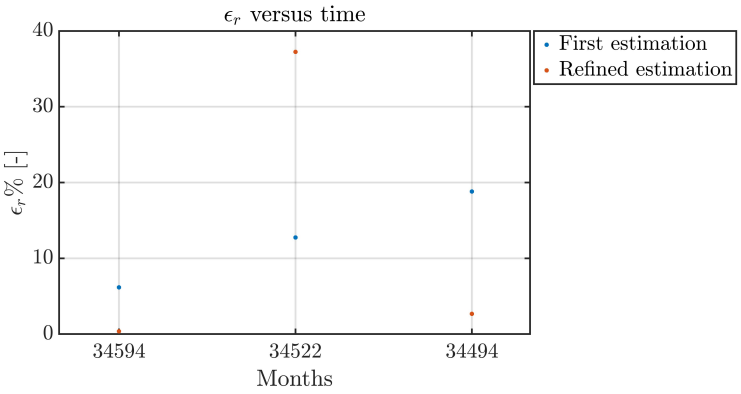

Figure 5.11: $\epsilon_r(\%)$ as function of the unknown object - Iridium 33 test case.

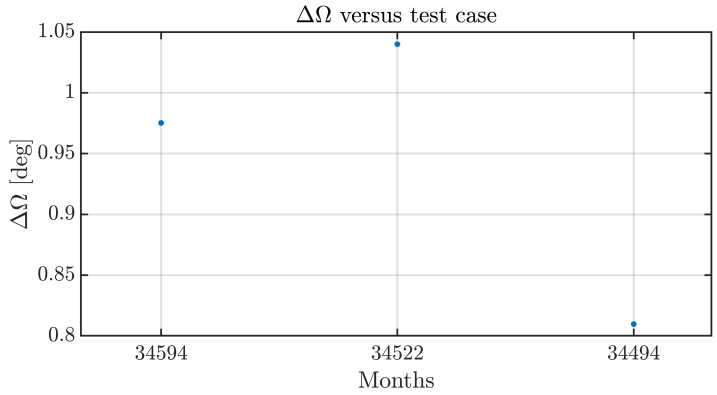

Figure 5.12: $\Delta\Omega$ evaluated at the event date - Iridium 33 test case.

Parent identification

Adopting the same thresholds introduced in the single family test section, each Iridium 33 case is tested for the parent identification. The initial set of the candidate bodies is constituted by 1577 objects. Figure 5.13 shows the trend of the number of objects that survive after the inclination clustering. For the first and the second test cases, all the thresholds adopted allow to have the correct candidate included in the set after the filtering. The third case, instead, fails when the threshold is set at 0.05 deg, that however is a very stringent threshold. An explanation could be given considering that the last case contains a lower number of objects, and hence it is possible that the mean value computed is much farther from the correct candidate than if computed considering a higher number of debris.

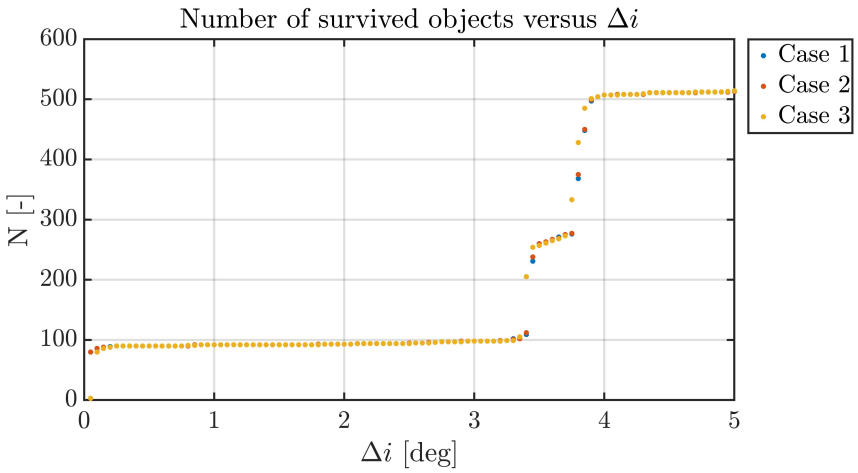

Figure 5.13: Number of survived candidates as a function of inclination threshold Δi - Iridium 33 test case.

The test of the triple-loop and of the RAAN filtering stages is performed considering the output of the inclination clustering with a Δi of 0.5 deg. It is important to remember that all the objects are propagated back to the previously obtained event dates before preforming these two filtering step. Table 5.5 shows the results obtained after all the filters have been applied to the candidates set. No test case is able to correctly identify the correct parent as the single final candidate. However, the method succeeds in narrowing the number of final candidates to a very small set of objects. The remaining foreign satellites are associated to other Iridium missions, which than present similar orbital elements to the analysed one.
Anyway, at the present level of the work, the results obtained are acceptable,

and further analysis will be performed to increase the accuracy.

	34594	**34522**	**34494**
Single Candidate	No	No	No
A/P - MOID (km)	-	-	-
$\Delta\Omega$ (deg)	-	-	-
# Multiple Candidates	5	8	9
A/P - MOID (km)	5-1	5-1	10-5
$\Delta\Omega$ (deg)	0.2	0.5	0.45

Table 5.5: Parent identification, second step results - Iridium 33 test case.

5.2.2 Fengyun 1C Breakup

This test considers the breakup event which involved the Fengyun 1C (NORAD ID 25730), dated 10 January 2007 at 22:26 GMT. As stated in the previous chapter, the Fengyun 1C represents a peculiar case by the inclination point of view, that is a wider distribution in orbit inclination of the generated fragments. The initial set it taken on 10 November 2007 (ten months after the event), and it is composed by 405 objects, of which 72 fragments belongs to the Fengyun 1C. The test is performed for three different initial unknown objects to observe how the initial condition influences the accuracy of the method. Each case is tested for both the event detection and the parent body identification.

Event detection

The unknown fragments selected per each case are the 29780, the 29729 and the 29765. The thresholds for the filtering phase are reported in Table 5.6.

Δi **(deg)**	**A/P (km)**	**MOID (km)**
1	25	20

Table 5.6: Filter thresholds - Fengyun 1C test case.

The results for each case are reported in Figure 5.14, where the relative error of the first estimation and of the refined one is compared, and in Figure 5.15, where the $\Delta\Omega$ at the first estimated date is displayed.

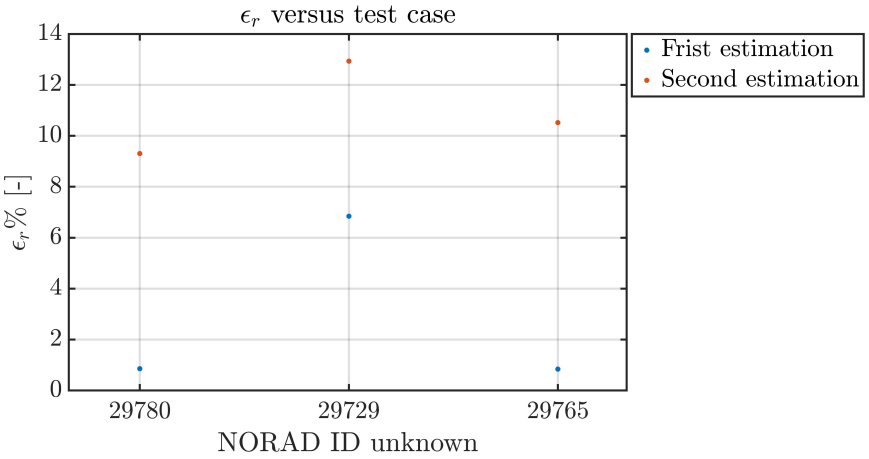

Figure 5.14: $\epsilon_r(\%)$ as function of the unknown object - Fengyun 1C test case.

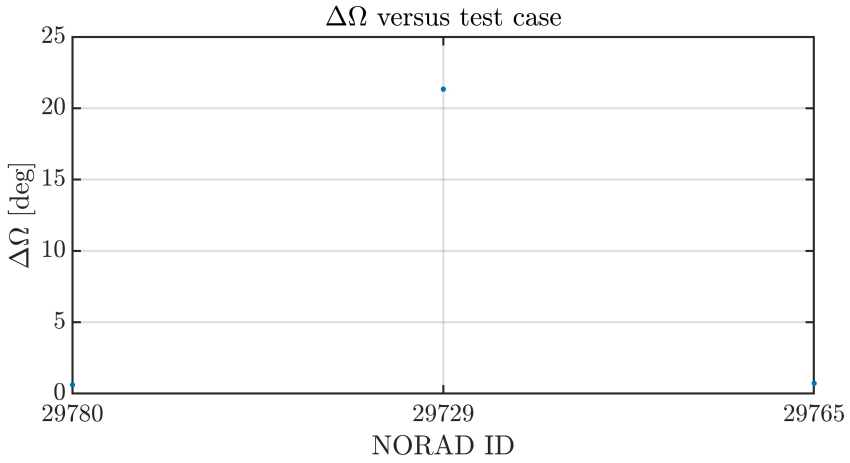

Figure 5.15: $\Delta\Omega$ evaluated at the event date - Fengyun 1C test case.

As visible, the second test case is associated to an higher relative error than the other two (that stay below the 1%). The reason of this outcome is evident looking at the final $\Delta\Omega$, where it is possible to observe a higher value for the second test case than the other two. Moreover, studying the final set of objects identified at the end of the propagation process (reported in Table 5.7), it appears that for the second case, the final set is not composed by all

Fengyun 1C fragments but includes also other objects. The presence of the four foreign bodies is probably the cause of the lower accuracy of the second case. The reason of the presence of those objects has to be attributed to a limitation of the pruning technique. However, the problem will be better analysed in the last proposed test.

	29780	**29729**	**29765**
# Total Objects	12	25	15
# Fengyun 1C Fragments	12	21	15

Table 5.7: Objects included in the set after the pruning phase - Fengyun 1C test case.

It is also important to note that the refinement technique fails for all the test cases. The blame for the failure can be given to the low number of fragments that have reached the final step of the method making the study more complex. Moreover, it is also possible that the hypothesis introduced to use the close approach technique are not valid if the elements are propagated back for too long time span.

Parent identification

Considering again the thresholds introduced at the beginning of this chapter, all the three cases are testes for the parent identification. The number of objects included in the initial candidates set is 1497.
Figure 5.16 shows the number of candidates surviving the inclination filter as function of Δi. Looking at the results, it is observable that for the first two cases the method fails when considering a Δi lower than 0.2 deg for the inclination filter, while the third case fails considering a Δi lower than 0.3 deg. The reason is probably in the higher widespread of the fragments in inclination than the other analysed case. This clearly entails that for a more general procedure, the low values obtained before are not suitable for all the possible cases. The test of the triple-loop and of the RAAN is performed considering the output of the inclination clustering with a Δi of 0.5 deg. Table 5.8 shows the results of the second step. The first and the third cases are able to properly recover the correct parent while the second case reach a solution in which 2 possible candidates remain in the final set. Probably the reason is, as for the event detection, the high $\Delta\Omega$ generated by the presence of wrong objects. The results are however good since, starting

from an initial set of 1497 candidates included in the initial set, the final conditions are narrowed enough.

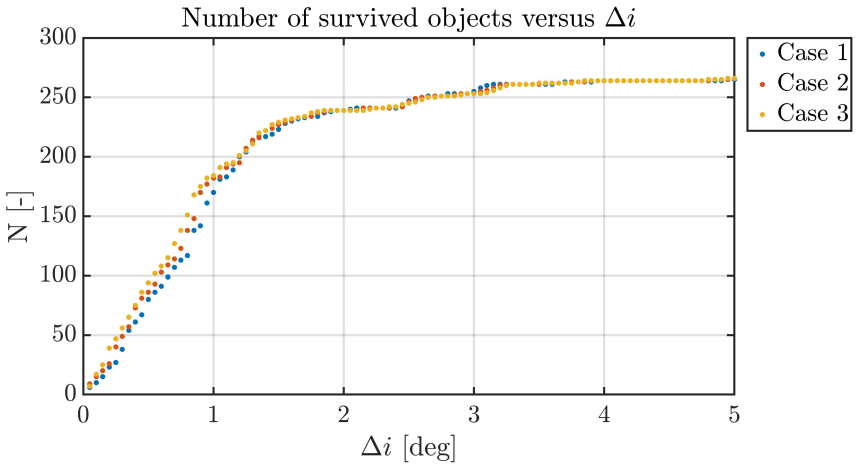

Figure 5.16: Number of survived candidates as a function of inclination threshold Δi - Fengyun 1C test case.

	29780	**29729**	**29765**
Single Candidate	Yes	No	Yes
A/P - MOID (km)	5-1	-	5-1
$\Delta\Omega$ (deg)	0.3	-	0.1
# Multiple Candidates	-	2	-
A/P - MOID (km)	-	5-1	-
$\Delta\Omega$ (deg)	-	1.4	-

Table 5.8: Parent identification, second step results - Fengyun 1C test case.

5.2.3 SL-14 R/B Breakup

The SL-14 R/B (NORAD ID 21656) breakup is dated 12 February 2020 at 10:46 UTC. This time, the test is performed considering a daily catalog taken at 23 February 2020 (about 1 year after the event). The number of objects included in the initial set are 16233, 104 of which are debris of SL-14 R/B. As always, an unknown fragment is randomly selected; for this test

case, the fragment 45270 (NORAD ID) is considered as unknown.
The thresholds for the filters are reported in Table 5.9.

Δi **(deg)**	**A/P (km)**	**MOID (km)**
0.5	15	10

Table 5.9: Filter thresholds - SL-14 R/B test case.

The pruning process rejects 16182 objects, creating a final set of 50 elements (38 belonging to SL-14 R/B). The majority of the objects are rejected during the inclination clustering phase (14755).
The remaining elements are then propagated to search the possible breakup event. Downstream the propagation, the set of objects is composed by 38 elements that are all fragments of the SL-14 R/B. Indeed, the binning method successfully eliminates the remaining 12 wrong objects, as visible in Figure 5.17.

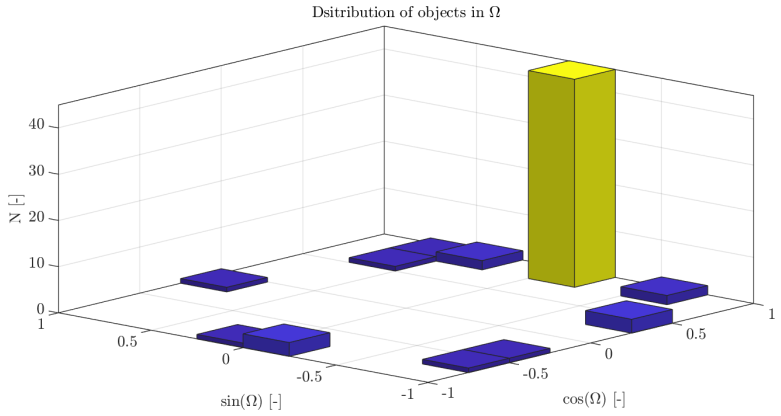

Figure 5.17: Ω distribution - SL-14 R/B test case.

The relative error in the first estimation is 5.3767%. By applying the refinement technique, the error decreases to 1.0184%. This time the method seems to work properly raising up the accuracy of the estimation.
The final set of fragments is then tested in the parent identification. The catalog of possible candidates counts 4567 objects. Figure 5.18 shows the number of candidates that survive after the inclination filtering stage. The correct parent is always included in the intermediate set.

For the second part, the intermediate set obtained considering Δi equal

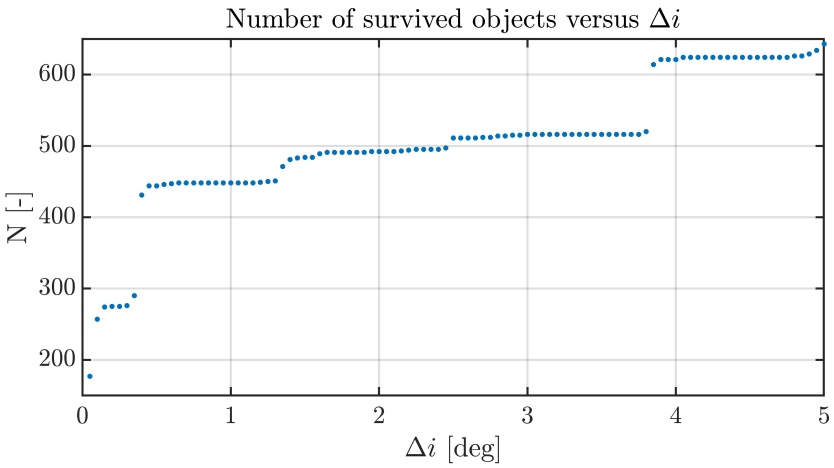

Figure 5.18: Number of survived candidates as a function of inclination threshold Δi - SL-14 R/B test case.

to 0.5 deg (that counts 444 possible candidates) is considered. Table 5.10 summarises the final conditions after the second filtering stage, performed after all the candidates are propagated back to the event date previously estimated.

Single Candidate	No
A/P - MOID (km)	-
$\Delta\Omega$ (deg)	-
# Multiple Candidates	2
A/P - MOID (km)	5-1
$\Delta\Omega$ (deg)	0.4

Table 5.10: Parent identification, second step results - SL-14 R/B test case.

Far all the combined thresholds cases, the method is not capable of finding the correct parent at the end of the process, but the final set is composed by 2 final candidates. As for the other cases, the limits reported in the table are the minimum ones that allow to have the narrowed solution.

5.2.4 USA 109 Breakup

This last test is dedicated to the breakup of the USA 109 (NORAD ID 23533), happened on 3 March 2015 at 17:40 GMT. This case is analysed because the breakup is occurred in a region denser of objects, that is the same of the Fengyun 1C and of the NOAA 16. The initial set includes 378 objects (40 belonging to USA 109), while the initial unknown object is the 40409 (NORAD ID).
Table 5.11 summarises the thresholds adopted for the pruning phase.

Δi **(deg)**	**A/P (km)**	**MOID (km)**
0.5	25	20

Table 5.11: Filter thresholds - USA 109 test case.

After the pruning phase, the set available for the propagation is composed by 58 objects (31 belonging to the USA 109). The propagation produces a relative error of 55.55%, while the final set of objects is composed by 38 objects (32 of which are UAS 109 fragments). The error obtained is very high if compared with all the ones of the previous tests. The problem is observable looking at Figure 5.19, that reports the distribution of the objects with respect to the Ω just before the propagation.

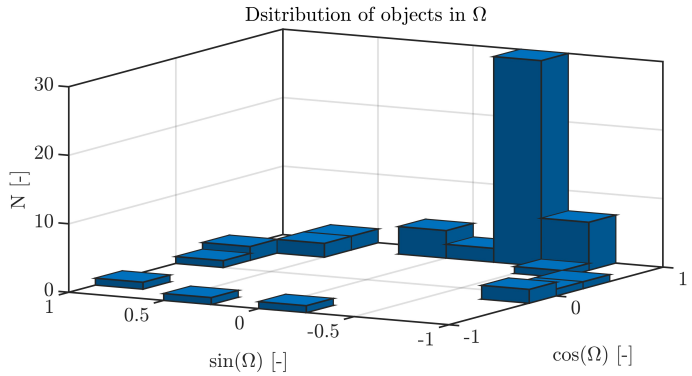

Figure 5.19: Ω distribution - USA 109 test case.

Indeed, it is possible to see that, around the maximum bin (that is composed by USA 109 fragments), other bins with a significant number of objects are located, the majority of which does not belong to the analysed

family. Consequently, during the propagation, as the RAAN evolves in time, it is possible that the foreign objects located near the correct ones will stay close to the unknown object and hence alter the solution estimation.
The reasons for this result are mainly two. First the method adopted for the binning formation; up to now, the number of bins generated is computed as the square root of the number of objects presented during the analysis. The second problem is related to the distribution in RAAN of the foreign objects remaining at the beginning propagation. Indeed, even considering more stringent values for the bin edges, it is possible that foreign fragments will stay close to the unknown one. Hence, when considering highly populated regions or, however, a higher number of objects in the initial set, it is probably needed a further step of filtering that eliminates this type of objects.

Chapter 6

Conclusions

6.1 Summary

The objectives of this thesis work were the detection of fragmentation events occurred in the past and the identification of the corresponding parent body. Moreover, the use of mean elements and the choice of a long time span for the orbits' evolution made the study more challenging than considering short time analysis (e.g. of the order of weeks). Even though the model developed here is subdivided into two parts, each of which focus on a specific goal, both the phases are intrinsically connected to each others. Indeed, the second part of the model needs the information obtained from the first one as initial conditions for the process. The method tries to exploit the natural properties of the objects orbit that characterise the region selected for the analysis (i.e. the LEO region) to make considerations in each step. This is clearly visible in the similarity between the steps of the first and of the second part of the model. A strong parameter has been identified in the orbit inclination. Indeed, thanks to its small evolution in time, it is suitable to cluster objects around the possible unknown fragments or to locate the region in which the parent objects can be identified. Nearer to the breakup event, it becomes powerful the use of the right ascension of ascending node as study parameter. Among all the others Keplerian orbital elements, the Ω tends to have a cluster in proximity of the event. Moreover, its evolution is well recovered by the propagator.
To appreciate the validity of the proposed model, tests concerning single family cases and more fillies cases have been performed. The first were carried out by exploiting breakup events located in different periods of the solar activity to appreciate possible differences caused by the simplification introduced in the propagation model. The seconds were carried out by examining

different breakup events with a different time span for the propagation, and by observing the sensitivity to the unknown fragment selected for the analysis. For all the tests cases, both the performances of the event detection and the parent identification routines have been checked. The results obtained proves the efficacy of both parts of the model. Regarding the single family tests, the maximum relative error obtained for the event detection is of about 14.8% on a time span of 24 months. The fault for this result can be associated on the one hand to the loss of accuracy in the propagation process during high solar activity periods, on the other hand to the objects included in the study set that may be more affected by the wrong BC estimation. The parent body identification routine is capable of including the correct objects in a narrowed set with respect to the initial one, and in some cases it is also capable of identifying it as the single last candidate. The latter is true unless too stringent thresholds values are chosen together with to long time span (more than one year) for the propagation. Regarding the model exploited to study the sets composed by objects of different families, the method seems to properly work both for the event detection and for the parent body.

However, some limitations are detected along the entire model. First of all, it is necessary to mention the possible inaccuracy in the BC estimation that reduces the accuracy of the propagation model. This inevitably affects the entire analysis since the latter is based on the study of the parameters evaluated through the propagator. Moreover, as observable from the single family test case, the period of study (e.g. near the minimum or near the peak of the solar cycle) partially affects the event detection. About the propagation phase, for the multiple families case, another limitation is related to the binning method, more precisely in the selection mode of the number of bins. The method seems to fail whenever, at the beginning of the propagation, the distribution of the objects along Ω is such that there are many objects, not correlated with the analysed unknown fragment, around the correct fragments. This can lead to a wrong selection of the event date. As stated many times, some LEO regions are highly exploited for different type of missions or are characterised by a large presence of fragments. The tests performed here consider only a small subset (mainly due to computational time problems) of the entire objects population. In case the latter is considered, the accuracy of the model, at the present state, could give worse results due to the inclusion of a grater number of undesired objects during the propagation phase. This implies that further levels of filtering have to be introduced in future modifications. A last remark is necessary for the refinement technique. Indeed, from the tests performed in the previous

chapter it is not possible to state if the method can work properly. Possible problems may arise when a low number of fragments is considered for the study. Moreover, the method can be affected by statistical inaccuracies, mainly related to the strong approximation introduced to perform it and to possible errors in the propagation. Hence, it is probable that the assumption made is not valid and the introduction of osculating orbital elements is needed for this type of analysis.
Despite all the cited limitations, the method gave great signals of success in achieving the prefixed objectives. Surely, many improvements can be made to increase its performance; some of the possible modifications are discussed in the following section.

6.2 Future works

This last section of the thesis is dedicated to the description of possible solutions for the previously identified limitations of the model and to the discussion of possible future works directly linked to this one.
The first issue is the number of fragments that can be handled by the model without having a too high computational time. This inevitably partially reduces the reliability of the process. The bottleneck of the problem seems to be the propagator, that slows down the process in case a high accuracy in the propagation itself is required. Speeding up the propagation surely would be a great improvement for the model, allowing the study of larger set of data. This may be fixed by using the propagator written in a different computer language, that is the C language.
A series of tests have been proposed to show the validity of the method. Surely, more tests are required to further validate the model and also to check the presence of other limitations. Additionally, performing more tests is important to have a better idea of the possible more suited values for all the threshold parameters presented inside the entire method, starting from the BC estimation, up to the thresholds for the pruning phase.
Speaking of the pruning phase, an important tool exploited is the triple-loop filter. The filter is implemented here without considering the influence of the perturbations. An improvement could be the integration of the dependence of the perturbations to each step of the triple-loop. Particularly to the method used to evaluate the MOID. Indeed, both the time windows check and the close encounter evaluation are performed considering a MOID constant in time. Surely this would lead to an increase in the complexity of the entire model, but would also increase the global accuracy of the study.
In addition to this, it would be important to try to elaborate a filter that

allows to better recognize fragments belonging to different families when the study is carried out far from the event date and in regions denser of objects. Another source of improvement is surely related to the BC estimation. Several analyses and tests were performed to understand the relation between the B^* parameter included in the TLE and the BC needed by the propagator. Even if the results seem to be good, further analysis in the estimation process would increase its accuracy. Indeed, this is the major source of inaccuracy in the propagation process and hence one of the major limitation of the entire process. A more in-depth study along with the comparison with real data would surely improve the accuracy of the entire model.
Regarding the second part of the model, a high improvement might be performed by the parent body identification; indeed, at the present state, the method only shows the bodies that could be at the origin of the fragmentation without accounting for priority among the identified bodies. It would be important to try to narrow down the choice of the possible candidates along with the assignment of a probability value to each candidate. The latter is of grate importance to have a more significant study regarding the characterisation of the event. Moreover, the idea is to further expand the routine by including a breakup model useful to recover features related to the generated fragment. The latter is directly linked to the parent body identification that is essential in each breakup model to perform analysis. The idea is to use the well known NASA breakup model [24] to produce simulations of the possible generated fragments and to estimate their physical properties. Then, from the results of the breakup model, it would be interesting to recover the orbital parameters of the generated debris. In addition to this, another enhancement to the model would be the implementation of a further routine, this time concerning a forward propagation. The idea is to improve the model introducing an analysis related to collision risks. Indeed, the present models identifies possible fragmentations occurred in the past along with the estimation of the parent body. A more general model that accounts also for the study of the collision risk concerning the generated fragments following the event would make the model more global and more reliable.
Then, the introduction of osculating orbital elements could be a further improvement for the method. The idea is to convert the mean orbital elements, used to detect the breakup events, into osculating orbital elements to perform a more precise investigation near the events. As observable from the tests performed to check the performances of the refinement technique, the latter does not always guarantee an improvement in the event date estimate. Hence, the use of osculating elements would be more suitable for the kind

of analysis performed and for a better localisation in space of the events.
A final consideration can be made with regards to the space regions. This work focuses on the LEO region only. This region is only a little portion of the entire space around the Earth. The study of fragmentations related to other regions, such as GEO, or to regions that share portion of space with other regions, such as the one where GTOs and HEOs are found, would increment the global knowledge of the debris world. Moreover, it would be possible to study possible interactions between the different regions together with the study of possible common features.
Finally, the idea is to develop a software tool (i.e. PUZZLE - long term), similar to the tool written by Romano et al. **ref?**, that integrates all the routines presented in this thesis work.

Bibliography

[1] C. Colombo. "Planetary orbital dynamics (PlanODyn) suite for long term propagation in perturbed environment". In: *Proceedings of the 6th International Conference on Astrodynamics Tools and Techniques (ICATT), ESOC/ESA, Darmstadt, Germany* (Mar. 2016).

[2] ESA Space Debris Office. *ESA's Annual Space Environment Report*. https://www.sdo.esoc.esa.int/environment_report/Space_Environment_Report_latest.pdf. 2020.

[3] National Research Council. *Orbital Debris: A Technical Assessment*. https://www.nap.edu/read/4765/chapter/4$#$24. 1995.

[4] NASA. *NASA - NSSDC - Spacecraft - Details - Mir*. https://web.archive.org/web/20090730232811/http://nssdc.gsfc.nasa.gov/nmc/masterCatalog.do?sc=1986-017A. 2010.

[5] P. D. Anz-Meador et al. "History of On-orbit satellite fragmentations 15^{th} Edition". In: *National Aeronautics and Space Administratio, Lyndon B. Johnson Space Center,Houston, Texas 77058* (2018). https://ntrs.nasa.gov/api/citations/20180008451/downloads/20180008451.pdf.

[6] NASA. *Space Debris and Human Spacecraft*. https://www.sdo.esoc.esa.int/environment_report/Space_Environment_Report_latest.pdf. 2013.

[7] ASI. *AMBIENTE SPAZIALE*. https://www.asi.it/lagenzia/facilities/registro-nazionale-degli-oggetti-lanciati-nello-spazio/ambiente-spaziale-2/. 2020.

[8] D. J. Kessler and B. G. Cour-Palais. "Collision frequency of artificial satellites: The creation of a debris belt". In: *J. Geophys* 83(A6) (1978), pp. 2637–2646. DOI: 10.1029/JA083iA06p02637.

[9] ISO/TC 20/SC 14 Space systems and operations. "Space systems — Space debris mitigation requirements". In: *Online Browsing Platform* (2019).

[10] D. A. Vallado. *Fundamentals of Astrodynamics and Applications, Fourth Edition*. USA: Space Technology Library, 2013.

[11] A. J. Rosengren et al. *Resident space object proper orbital elements*. 2019.

[12] P. Bendjoya and V. Zappala. "Asteroid Family Identification". In: *Asteroids III* (Jan. 2002).

[13] R. B. Southworth and G. S. Hawkins. "Statistics of meteor streams". In: *Smithsonian Contributions to Astrophysics* 7 (Jan. 1963), pp. 261–285.

[14] L. Di Mare et al. "In-Orbit Fragmentation Characterization and Parent Bodies Identification by Means of Orbital Distances". In: *First International Orbital Debris Conference*. Vol. 2109. Dec. 2019, p. 6007.

[15] J. D. Drummond. "A test of comet and meteor shower associations". In: *Icarus* 45 (Mar. 1981), pp. 545–553.

[16] T. Jopek. "Remarks on the Meteor Orbital Similarity D-Criterion". In: *Icarus* 106 (Dec. 1993), pp. 603–607. DOI: 10.1006/icar.1993.1195.

[17] V. Zappala et al. "Asteroid families. I. Identification by hierarchical clustering and reliability assessment". In: *The Astronomical Journal* 100 (Nov. 1990), pp. 2030–2046. DOI: 10.1086/115658.

[18] P. Bendjoya, E. Slezak, and C. Froeschle. "The wavelet transform - A new tool for asteroid family determination". In: *Astronomy and Astrophysics* 251.1 (Nov. 1991), pp. 312–330.

[19] V. Zappala et al. In: *Icarus* 59 (1984), p. 261.

[20] G. F. Gronchi. "An Algebraic Method to Compute the Critical Points of the Distance Function Between Two Keplerian Orbits". In: *Celest. Mech. Dyn. Astron.* 93 (Sept. 2005), pp. 295–329. DOI: 10.1007/s10569-005-1623-5.

[21] F. R. Hoots, L. L. Crawford, and R. L. Roehrich. "An Analytic Method to Determine Future Close Approaches Between Satellites". In: *Celestial Mechanics* 33.2 (June 1984), pp. 143–158. DOI: 10.1007/BF01234152.

[22] S. Frey, C. Colombo, and S. Lemmens. "Density based modeling and indication of break-up location and epoch from fragments using bacwards propagation". In: 5^{th} *European Workshop on Space Debris Modelling and Remediation, Paris* (June 2018).

[23] M. Romano et al. "PUZZLE software for the characterisation of in-orbit fragmentations". In: 8^{th} *European Conference on Space Debris, ESA/ESOC, Darmstadt, Germany, Virtual Conference* (Apr. 2021).

[24] N. L. Johnson et al. "NASA'S new breakup model of evolve 4.0". In: *Elsevier Science* 28, N.9 (2001), pp. 1377–1384. DOI: https://doi.org/10.1016/S0273-1177(01)00423-9.

[25] R. L. Andrisan et al. "Fragmentation event model and assessment tool (FREMAT) supporting on-orbit fragmentation analysis". In: *The 6th International Conference on Astrodynamics Tools and Techniques (ICATT), Germanium (Darmstadtium)* (Mar. 2016).

[26] J. Dolado et al. "OPERA: A tool for lifetime prediction based on orbit determination from TLE data". In: *Conference: International Symposium on Space Flight DynamicsAt: Laurel, Maryland – USA* (Jan. 2014).

[27] D. Gondelach, R. Armellin, and A. Lidtke. "Ballistic Coefficient Estimation for Reentry Prediction of Rocket Bodies in Eccentric Orbits Based on TLE Data". In: *Mathematical Problems in Engineering* 2017 (Nov. 2017). DOI: 10.1155/2017/7309637.

[28] S. Frey et al. "Extension of the King-Hele orbital contraction method and application to thegeostationary transfer orbit re-entry prediction". In: 4^{th} *Armellin4thInternational Workshop on Space Debris ReentryESOC, Darmstadt* (Feb. 2018).

[29] M. Matney. *Gabbard Plot Discussion*. https://ntrs.nasa.gov/api/citations/20150009502/downloads/20150009502.pdf. 2015.

[30] C. Colombo. *Orbital Mechanics - Orbit Perturbations Lectures*. 2018.

[31] H. A. Curtis. *Orbital Mechanics for Engineering Students, Third Edition*. USA: Butterworth-Heinemann, 2013.

[32] R. H. Battin. *An Introduction to the Mathematics and Methods of Astrodynamics, Revised Edition*. American Institute of Aeronautics and Astronautics, ISBN 978-1-56347-342-5,Inc., 1999.

[33] D. King-Jele. *Theory of Satellite Orbits in an Atmosphere*. London: Butterworths, ISBN 978-021692252, 1964.

[34] A. V. Kirov, L. L. Sokolov, and V. V. Dikarev. "Dynamics of Mars-Orbiting Dust: Effects of Light Pressure and Planetary Oblateness". In: *Celestial Mechanics and Dynamical Astronomy* 63 (1995), pp. 313–339. DOI: 10.1007/bf00692293.

[35] B. Kaufman and R. Dasenbrock. "Higher order theory for long-term behaviour of earth and lunar orbiters". In: *Naval Research Laboratory* (1972).

[36] J. Meeus. "Astronomical Algorithms". In: *Willmann-Bell, Inc., 2^{nd} edition, ISBN 978-0943396613* (1998).

[37] W. M. Kaula. *Theory of Satellite Geodesy: Applications of Satellites to Geodesy.* Blaisdell Publishing Company, ISBN 978-0486414652., 1966.

[38] D. Bouwer. "Solution of the problem of artificial satellite theory without drag." In: *Astronomical Journal* 64 (1959), pp. 378–396. DOI: 10.1086/107958..

[39] D. A. Vallado et al. "Revisiting Spacetrack Report #3". In: *AIAA* (2006).

[40] AGI (Ansys Company). *SGP4 Propagator.* https://help.agi.com/stk/11.0.1/Content/stk/vehSat_orbitProp_msgp4.htm.

[41] A. Lidtke, D. Gondelach, and R. Armellin. "Optimising filtering of two-line element sets to increase re-entry prediction accuracy for GTO objects". In: *Advances in Space Research* 63 (Feb. 2019), pp. 1289–1317. DOI: 10.1016/j.asr.2018.10.018.

[42] D. A. Vallado and W. D. McClain. "Fundamentals of Astrodynamics and Applications". In: *Space Technology Library, Microcosm Press* (2013).

[43] J. M. Picone, J. T. Emmert, and J. L. Lean. "Thermospheric densities derived from spacecraft orbits: Accurate processing of two-line element sets". In: *Journal of Geophysical Research: Space Physics* 110.A3 (2005). DOI: https://doi.org/10.1029/2004JA010585. eprint: https://agupubs.onlinelibrary.wiley.com/doi/pdf/10.1029/2004JA010585. URL: https://agupubs.onlinelibrary.wiley.com/doi/abs/10.1029/2004JA010585.

[44] S. Frey, C. Colombo, and S. Lemmens. "Extension of the King-Hele orbit contraction method for accurate, semi-analytical propagation of non-circular orbits". In: *Advances in Space Research* 64 (July 2009), pp. 1–17.

[45] G. Sitarski. "Approaches of the Parabolic Comets to the Outer Planets". In: *Acta Astronautica* 18 (Jan. 1968). https://ui.adsabs.harvard.edu/abs/1968AcA....18..171S, Provided by the SAO/NASA Astrophysics Data System, p. 171.

[46] G. F. Gronchi. "On the Stationary Points of the Squared Distance between Two Ellipses with a Common Focus". In: *Siam Journal on Scientific Computing* 24 (Aug. 2002). DOI: 10.1137/S1064827500374170.

[47] D. Cox, J. Little, and D. O'Shea. *Ideals, Varieties, and Algorithms*. Springer-Verlag, 1992.

[48] D. Brouwer. In: *Astron. J.* 56 (1951), p. 9.

[49] T.S.Kelso. *Frequently Asked Questions: Two-Line Element Set Format*. https://www.celestrak.com. 2019.

Appendix A

Hierarchical clustering method examples

The coefficients k_1, k_2 and k_3 (introduced in Section 1.3.1) are not selected casually, but rather are directly connected to each other.
In the paper of Zappala et al. [17], a method useful to have a relation among the parameters under study that would allow to have a proper weight of each of them is proposed. Both for the metric definition and the constant computation, the study begins from the system of equations

$$\frac{\delta a}{a} = 2\frac{\delta v_1}{na} \tag{A.1a}$$

$$\delta e = \frac{\delta v_2 sin(f)}{na} + 2\frac{\delta v_1 cos(f)}{na} \tag{A.1b}$$

$$\delta i = \frac{\delta v_3 cos(\omega + f)}{na} \tag{A.1c}$$

found following the statement present in Brouwer et al. [48] and Zappala et al. [19].
Then, the system of equations is squared, averaging it over f and $\omega + f$, and the results are substituted inside the metric 1.9, obtaining the equation

$$\delta v = \sqrt{x\delta v_1^2 + y\delta v_2^2 + z\delta v_3^2} \tag{A.2}$$

where

$$x = 4k_1 + 2k_2 \tag{A.3a}$$

$$y = \frac{k_2}{2} \tag{A.3b}$$

$$z = \frac{k_3}{2} \tag{A.3c}$$

As clearly visible, parameter k_1 and k_2 are not independent from each other and, consequently, it is not possible to have the solution x = y = z = 1 since the coefficients have to be positive to have significance in the procedure.
However, in this way it is possible to give more importance to a specific orbital parameter over the other ones.

Appendix B

Two-Line-Elements

The following tables summarie the NORAD Two-Line-Element set format described in [49]. Each TLE, as the name suggest, is composed by two lines. The first line contains mainly information about the identification of the objects (e.g. the satellite identification number) while the second line includes information about the orbital parameters of the objects considered. The latter, as already stated, are mean elements. Table B.1 refers to the first line, while Table B.2 refers the second line.
As an example, the following is a TLE of an Iridium 33 debris:

1 35625U 97051QX 20353.57473472 .00000715 00000-0 33538-3 0 9993

2 35625 86.1999 87.8745 0129042 228.5689 189.9746 14.14584985402124

Column	Content
01	Line Number of Element Data
03-07	Satellite Number
08	Classification (U=Unclassified, C=Classified, S=Secret)
10-11	International Designator (Last two digits of launch year)
12-14	International Designator (Launch number of the year)
15-17	International Designator (Piece of the launch)
19-20	Epoch Year (Last two digits of year)
21-32	Epoch (Day of the year and fractional portion of the day)
34-43	First Time Derivative of the Mean Motion
45-52	Second Time Derivative of Mean Motion
	(Leading decimal point assumed)
54-61	BSTAR drag term (Leading decimal point assumed)
63	Ephemeris type
65-68	Element number
69	Checksum (Modulo 10)
	(Letters, blanks, periods, plus signs = 0; minus signs = 1)

Table B.1: TLE-Line 1

Column	Content
01	Line Number of Element Data
03-07	Satellite Number
09-16	Inclination [Degrees]
18-25	Right Ascension of the Ascending Node [Degrees]
27-33	Eccentricity (Leading decimal point assumed)
35-42	Argument of Perigee [Degrees]
44-51	Mean Anomaly [Degrees]
53-63	Mean Motion [Revs per day]
64-68	Revolution number at epoch [Revs]
69	Checksum (Modulo 10)

Table B.2: TLE-Line 2

Appendix C

MOID parameters

Here are presented the definitions of elements introduced in section 2.6.2.

C.1 Position vector

The position vectors defined in Eq. 2.23 and Eq. 2.24 (for the first and the second body respectively) include four vectors which are function of the classical Keplerian orbital elements. The latter are evaluated through the use of the matrices H_1 and H_2 reported in Eq. C.1 and Eq. C.3, and are used to define the orbits in a 3-dimentional space [20]. The matrix H_1 is defined as

$$H_1 = \begin{bmatrix} 1 & 0 & 0 \\ 0 & cos(i_1) & -sin(i_1) \\ 0 & sin(i_1) & cos(i_1) \end{bmatrix} \begin{bmatrix} cos(\omega_1) & -sin(\omega_1) & 0 \\ sin(\omega_1) & cos(\omega_1) & 0 \\ 0 & 0 & 1 \end{bmatrix} \tag{C.1}$$

and, from the first two columns of the matrix, the components of $\underline{\mathfrak{P}}$ and of $\underline{\mathfrak{Q}}$ are evaluated

$$\underline{\mathfrak{P}} = \begin{cases} \mathfrak{P}_x = cos(\omega_1) \\ \mathfrak{P}_y = sin(\omega_1)cos(i_1) \\ \mathfrak{P}_z = sin(\omega_1)sin(i_1) \end{cases} \tag{C.2a}$$

$$\underline{\mathfrak{Q}} = \begin{cases} \mathfrak{Q}_x = -sin(\omega_1) \\ \mathfrak{Q}_y = cos(\omega_1)cos(i_1) \\ \mathfrak{Q}_z = cos(\omega_1)sin(i_1) \end{cases} \tag{C.2b}$$

The matrix H_2 is instead defined as

$$H_2 = \begin{bmatrix} cos(\Omega_2 - \Omega_1) & -sin(\Omega_2 - \Omega_1) & 0 \\ sin(\Omega_2 - \Omega_1) & cos(\Omega_2 - \Omega_1) & 0 \\ 0 & 0 & 1 \end{bmatrix} \begin{bmatrix} 1 & 0 & 0 \\ 0 & cos(i_2) & -sin(i_2) \\ 0 & sin(i_2) & cos(i_2) \end{bmatrix} \begin{bmatrix} cos(\omega_2) & -sin(\omega_2) & 0 \\ sin(\omega_2) & cos(\omega_2) & 0 \\ 0 & 0 & 1 \end{bmatrix} \tag{C.3}$$

and, as for the previously defined vectors, the components of $\underline{\mathfrak{p}}$ and of $\underline{\mathfrak{q}}$ are evaluated through the elements in the first two columns of the matrix

$$\underline{\mathfrak{p}} = \begin{cases} \mathfrak{p}_x = cos(\omega_2)cos(\Omega_2 - \Omega_1) - sin(\omega_2)cos(i_2)sin(\Omega_2 - \Omega_1) \\ \mathfrak{p}_y = cos(\omega_2)sin(\Omega_2 + \Omega_1) + sin(\omega_2)cos(i_2)cos(\Omega_2 - \Omega_1) \\ \mathfrak{p}_z = sin(\omega_2)sin(i_2) \end{cases} \tag{C.4a}$$

$$\underline{\mathfrak{q}} = \begin{cases} \mathfrak{q}_x = -sin(\omega_2)cos(\Omega_2 - \Omega_1) - cos(\omega_2)cos(i_2)sin(\Omega_2 - \Omega_1) \\ \mathfrak{q}_y = -sin(\omega_2)sin(\Omega_2 - \Omega_1) + cos(\omega_2)cos(i_2)cos(\Omega_2 - \Omega_1) \\ \mathfrak{q}_z = cos(\omega_2)sin(i_2) \end{cases} \tag{C.4b}$$

C.2 Coefficients of the polynomial system

The polynomial system defined in Eq. 2.29 is function of the polynomial coefficients, each of which is function of the true anomaly. The coefficients f_i (with $i = 0, ..., 4$) are parameters included in the first equation of the previously mentioned polynomial system and are evaluated as

$$\begin{cases} f_0(t) = p(E+1)^2(Lt^2 - 2Nt - L) \\ f_1(t) = -2[Kp(E+1) + EP(e-1)]t^2 + 4pM(E+1)t + \\ \qquad +2[Kp(E+1) + EP(e+1)] \\ f_2(t) = 0 \\ f_3(t) = 2[Kp(E-1) - EP(e-1)]t^2 - 4pM(E-1)t + \\ \qquad -2[Kp(E-1) - EP(e+1)] \\ f_4(t) = -p(E-1)^2(Lt^2 - 2Nt - L) = -\frac{(E-1)^2}{(E+1)^2} f_0(t) \end{cases} \tag{C.5}$$

while the coefficients g_i (with $i = 0, 1, 2$) are parameters included in the second equation, and are computed as

$$\begin{cases} g_0(t) = PM(e-1)^2t^4 + [-2KP(e-1) + 2ep(E+1)]t^3 + \\ \qquad +[2KP(e+1) + 2ep(E+1)]t - PM(e+1)^2 \\ g_1(t) = 2PN(e-1)^2t^4 - 4PL(e-1)t^3 + 4PL(e+1)t + \\ \qquad -2PN(e+1)^2 \\ g_2(t) = -PM(e-1)^2t^4 + [2KP(e-1) - 2ep(E-1)]t^3 + \\ \qquad +[-2KP(e+1) - 2ep(E-1)]t + PM(e+1)^2 \end{cases} \tag{C.6}$$

C.3 Sylvester matrix and resultant

The Sylvester matrix, associated to the two univariate polynomials included in the system of equation 2.29, is

$$S(t) = \begin{bmatrix} f_4 & 0 & g_2 & 0 & 0 & 0 \\ f_3 & f_4 & g_1 & g_2 & 0 & 0 \\ 0 & f_3 & g_0 & g_1 & g_2 & 0 \\ f_1 & 0 & 0 & g_0 & g_1 & g_2 \\ f_0 & f_1 & 0 & 0 & g_0 & g_1 \\ 0 & f_0 & 0 & 0 & 0 & g_0 \end{bmatrix} \tag{C.7}$$

where the coefficient of the matrix have been defined in C.5 and C.6. The resultant of the matrix C.7 is

$$\begin{aligned} Res(t) = &-g_0g_1^3f_1f_4 + 3g_0^2g_1g_2f_1f_4 + g_0g_1^2g_2f_1f_3 - g_1^3g_2f_0f_3 - g_1g_2^3f_0f_1 + \\ &+ 3g_0g_1g_2^2f_0f_3 - g_0^3g_1f_3f_4 - 4g_0g_1^2g_2f_0f_4 + 2g_0^2g_2^2f_0f_4 + g_2^4f_0^2 + \\ &+ g_0^4f_4^2 + g_1^4f_0f_4 + g_0^3g_2f_3^2 - 2g_0^2g_2^2f_1f_3 + g_0g_2^3f_1^2 \end{aligned} \tag{C.8}$$

During the process for the evaluation of the resultant of the matrix, the Sylvester matrix is modified with the introduction of new coefficients. The modified Sylvester matrix becomes

$$\hat{S}(t) = \begin{bmatrix} f_4 & 0 & g_2 & 0 & 0 & 0 \\ f_3 & f_4 & g_1 & g_2 & 0 & 0 \\ 0 & \tilde{f}_3 1 & \tilde{g}_2 0/\alpha_E & \tilde{g}_1 & \tilde{g}_2 0 & \alpha_E \tilde{g}_1 \\ \tilde{f}_3 1/\alpha_E & 0 & \tilde{g}_1/\alpha_E & \tilde{g}_2 0/\alpha_E & \tilde{g}_1 & \tilde{g}_2 0 \\ f_0 & f_1 & 0 & 0 & g_0 & g_1 \\ 0 & f_0 & 0 & 0 & 0 & g_0 \end{bmatrix} \tag{C.9}$$

where the new coefficients are defined as

$$\begin{cases} \alpha_E = \frac{E-1}{E+1} \\ \tilde{f}_{31}(t) = -2EP(1+\alpha_E) \\ \tilde{g}_1(t) = 2P[N(e-1)t^2 - 2Lt + N(e+1)] \\ \tilde{g}_20(t) = P(\alpha_e - 1)[M(e-1)t^2 - 2Kt + M(e+1)] \end{cases} \tag{C.10a}$$

Appendix D

Objects ID

D.1 Triple-loop filter example Elements ID

41558, 47690, 47689, 47688, 47687, 47686, 47685, 47684, 47618, 41558, 41557, 41510 41508, 41507, 38030, 38024, 32157, 32156, 32155, 32154, 32153, 32152, 32150, 32148, 32146, 32143, 32137, 22699, 22698, 22693, 22692, 22691, 22690, 22689, 22688, 22675, 22, 20, 16, 12, 11, 5.

D.2 Single Family

D.2.1 Cosmos 2251, single family case 1

22675, 33758, 33761, 33762, 33782, 33799, 33838, 33841, 33842, 33848, 33912, 33913, 33929, 33930, 33932, 33942, 33944, 33986, 33994, 34001, 34004, 34009, 34015, 34021, 34032, 34045, 34057, 34061, 34064, 34065, 34117, 34124, 34275, 34319, 34331, 34386, 34387, 34427, 34458, 34473, 34546, 34552, 34553, 34554, 34555, 34556, 34561, 34563, 34564, 34576 34590.

D.2.2 Cosmos 2251, single family case 2

33761, 34308, 33762, 33763, 33764, 33766, 33770, 34323, 34325, 34327, 34330, 33843, 33844, 33845, 33848, 33889, 34445, 34446, 34447, 34448, 34449, 33940, 33942, 33944, 33945, 33948, 34563, 34564, 34567, 34570, 34571, 34010, 34012, 34013, 34014, 34015, 34017, 34019, 34273, 34274, 34275,34468,34469,34473,34474,34477,33911,33912,33913,33918,33919.

D.2.3 NOAA 16, single family case 1

41053, 41054, 41055, 41056, 41057, 41058, 41059, 41060, 41061, 41062, 41063, 41064, 41065, 41066, 41067, 41068, 41069, 41070, 41071, 41074, 41075, 41076, 41077, 41078, 41079, 41080, 41081, 41083, 41084, 41085, 41086, 41088, 41089, 41090, 41092, 41093, 41094, 41095, 41096, 41126, 41131, 41132, 41133, 41134, 41135, 41137, 41138, 41139, 41141, 41142, 41143,41148,41149,41150,41153,41156,41158,41160,41161,41163, 41165.

D.2.4 NOAA 16, single family case 2

41050, 41054, 41057, 41060, 41069, 41071, 41075, 41077, 41081, 41084, 41085, 41086, 41096, 41129, 41137, 41139, 41144, 41152, 41156, 41202, 41203, 41213, 41217, 41220, 41228, 41229, 41231, 41251, 41252, 41264, 41265, 41269, 41273, 41275, 41277, 41283, 41286, 41288, 41290, 41296, 41301, 41305, 41306, 41348, 41350, 41355, 41363, 41369, 41372, 41409, 41413, 41414, 41415, 41419, 41422, 41423, 41425, 41426, 41427, 41428.